Synthesis and characterization of ion implanted Pd/Ti/V/Pd/Ti based multilayer thin films using Rutherford backscattering spectrometry (RBS) and elastic recoil detection analysis (ERDA) for hydrogen storage application.

Nyabane Blessing Maebela

A thesis submitted in partial fulfilment of the requirements for the degree of magister scientiae in the Department of Physics and Astronomy, University of the Western Cape.

Supervisors: **Dr Christopher Mtshali**
Material Research Department, iThemba LABS

Prof Reginaldt Madjoe
Department of Physics and Astronomy, University of the Western Cape

Declaration

Student number: 3878741

I declare **Synthesis and characterization of ion implanted Pd/Ti/V/Pd/Ti based multilayer thin films using Rutherford backscattering spectrometry (RBS) and elastic recoil detection analysis (ERDA) for hydrogen storage application** is my work and all the resources i have used or quoted have been indicated using complete references.

Signature: **Date**:

Nyabane Blessing Maebela

Abstract

Hydrogen is regarded as an attractive, pollution-free energy carrier for future energy systems, supported by its efficient energy conversion. Still, the challenge is its storage and transportation. Hydrogen can either be stored as a liquid in cryogenic tanks, gas in high-pressure cylinders or as a solid in metal hydrides. Metal hydrides are of research interest for hydrogen storage due to their higher energy density as compared to the gas- or liquid form and metal hydrides are also relatively safe. In this investigation, a **Pd (25nm)/Ti (50nm)/V (50nm)/Pd (25nm)** multilayer system was prepared on commercially available pure titanium (CP-Ti) substrates using an electron beam evaporator in order to investigate its viability for hydrogen storage. The sequential deposition of layers **Pd (25nm)/Ti (50nm)/V (50nm)/Pd (25nm)** was done at a constant deposition rate of 0.6 Å/s. Prior to implantation, samples were characterized for thickness confirmation using Rutherford backscattering spectrometry (RBS) technique discussed in the chapter 4. Two samples were implanted with Fe ions at 150 keV to higher fluences of 1×10^{15} and 1×10^{16} *ions/cm*^{2} respectively while the other three samples were implanted with Fe ions at 150 keV to fluences of 1×10^{12}, 1×10^{13}, *and* $1 \times 10^{14,}$ respectively. All the samples were hydrogenated using pure hydrogen gas at a substrate temperature 550 °C for 30 minutes. SEM revealed rough and non-uniform surfaces for the as-deposited samples with interconnected crystals that resulted from the deposition process. The implanted samples displayed no changes, particularly at low fluences (1×10^{12}, 1×10^{13} ,1×10^{14} $ions/cm^2$), except samples implanted at high fluence with (1×10^{15} and 1×10^{16} $ions/cm^2$) which displayed small changes.

XRD revealed that no intermixing took place as no new structural formation was observed. The RBS results supported the XRD results as the implanted samples showed stability with no indication of intermixing of the layers, particularly the Pd layers. XRD showed no intermixing of layers for the hydrogenated samples, and the TH_2 (titanium hydride) phase was difficult to

distinguish since its amount was low and overlapped with Ti peaks. RBS indicated that there was no spontaneous reaction during hydrogenation; thus, this process did not affect the integrity of the film stack. ERDA results revealed a maximum H atomic concentration of ~4.8 at% at a depth of ~1.8 µm for non-implanted samples and an average H concentration of ~2.6 at% over the probed depth. The average H concentration values over a probed depth were ~2.7, ~2.28, ~1.3, ~1.25 and ~1.18 at% in samples implanted at fluence values of 1×10^{12}, 1×10^{13}, 1×10^{14}, 1×10^{15} and 1×10^{16} ions/cm^2 respectively. These findings suggest that Fe ion implantation did not enhance but restricted H absorption at least to these fluence values.

Dedication

This work is dedicated to the following people:

- My parents Mogobe and Mamphake Maebela.
- My grandmother Mankokwane Moleke.
- My children
- My Partner
- My siblings

The following people who are late: My grandfathers, Magatikele Moleke and Nyabane Maebela, lastly my grandmother Matseleng Maebela.

Acknowledgements

Samathomo ke rata go leboga yo godimo le badimo ka moka baga Maebela lebaga Moleke geba mphile maatla, bohlale, kgotlelelo, le tŝhireletŝo gore ke kgone go phethagatŝa moŝomo o.

For this project to be successful, many people have participated in it so it gives me great pleasure to express my sincere appreciation to the following people for their contributions because without their efforts this work would not have been possible.

- My supervisor Dr Christopher Mtshali (iThemba LABS) for affording me this opportunity to carry out this project. His support, guidance and encouragement throughout this study were immeasurable. From his paramount supervision, I have accumulated much knowledge of ion beam analysis techniques from experimental work to simulations. His guidance in thesis writing, constructive comments, and corrections.
- My supervisor Prof Reginaldt Madjoe (UWC) for his continuous support, encouragement, comments and making sure that i get extension of the research funding.
- Dr Remy Bucher (iThemba LABS) for assisting me with the XRD technique.
- Dr Jack Matido (iThemba LABS) for assisting me with SRIM software.
- The staff and students from Material Research Department (iThemba LABS) for their support and help throughout this study.
- Dr Zakhele Khumalo and Nametso Mongwaketsi (iThemba LABS) for assisting me with ion beam analysis measurements.
- Mr Adrian Josephs (UWC) for assisting me with the scanning electron microscopy (SEM) technique.

- Prof Christopher Arendse (UWC) with his team for assisting us with hydrogenation experiments.
- Dr Mlungisi Nkosi (HoD at MRD iThemba LABS) for his support throughout this journey.
- All the technicians working at Tandetron accelerator at MRD iThemba LABS for assisting with technical work.
- My family, starting with my parents (Mogobe and Mamphake Maebela) for their immense support, patience, love and their prayers throughout this journey. My siblings (Matseleng, Lebogang and Katlego Maebela), my friends for their continuous support. My partner (Mashego Kgetho Uma) for her support throughout this journey.
- Lastly National Research Foundation (NRF) for the financial support to carry out this project.

Key words

Titanium

Palladium

Vanadium

Hydrogen

Hydrogen storage

Hydrogenation

Electron beam evaporation

Thin film coatings

Multilayers

Rutherford backscattering spectrometry

Elastic recoil detection analysis

Scanning electron microscopy

Phase transformation

Ion implantation

Metal hydrides

Abbreviations

Titanium: Ti

Palladium: Pd

Vanadium: V

Hydrogen: H

Rutherford backscattering spectrometry: RBS

Elastic recoil detection analysis: ERDA

X-ray diffraction: XRD

Scanning electron microscopy: SEM

Stopping and range of ions in matter: SRIM

Transport of ions in matter: TRIM

Proton exchange membrane: PEM

List of Tables

List of Figures

Contents

Chapter 1

Introduction

This chapter entails the background of the study, fuel cell technology, an overview on hydrogen storage techniques, the aim and objectives of this investigation.

1.1 Background

Energy is the driving force for daily human activities, economic and technological developments [1.13]. Due to growth in the human population and technological developments, the energy demand has been increasing rapidly. Fossil fuels remain the cornerstone energy sources that global society relies on to settle their energy needs. They contribute about 80 % of global energy consumption with 32.8 % petroleum, 27.2 % coal, and 20.9 % natural gas [1.1-1.3]. However, there are two significant problems associated with complete dependence on fossil fuel-based energy.

Firstly, fossil fuels deposits such as coal, petroleum, and natural gas will be depleted because, the consumption rate of these fossil fuel deposits is higher than the rate it takes them to accumulate [1.2]. As the global population rises and advances of technologies emerge, which are wholly dependent on fossil fuels, there are some concerns that fossil fuel reserves will not manage to satisfy energy needs for the future [1.4]. Fossil fuel reserves that are currently available are expected to last for a limited number of years, i.e., 40 years for petroleum, 60 years for natural gas, and 250 years for coal [1.4]. The depletion of fossil fuel put global energy systems and economic stability under threat.

Secondly, Fossil fuels are not friendly to the environment. During the combustion of fossil fuels to produce energy, harmful gases such as CO_2, SO_2, and NO_2 are discharged into the atmosphere, affecting air quality. These gases, also called greenhouse gases, endanger human health, hence are principal contributors to global warming [1.3, 1.6, 1.13].

Three significant sectors that participate in greenhouse gases (GHGs) emission during fossil fuel combustion is transportation, industry, and electricity generation [1.3]. **Figure 1.1** shows their contributions. To overcome these drawbacks associated with fossil fuel-based energy, non-polluting, economically competitive, and more sustainable energy source need to be used.

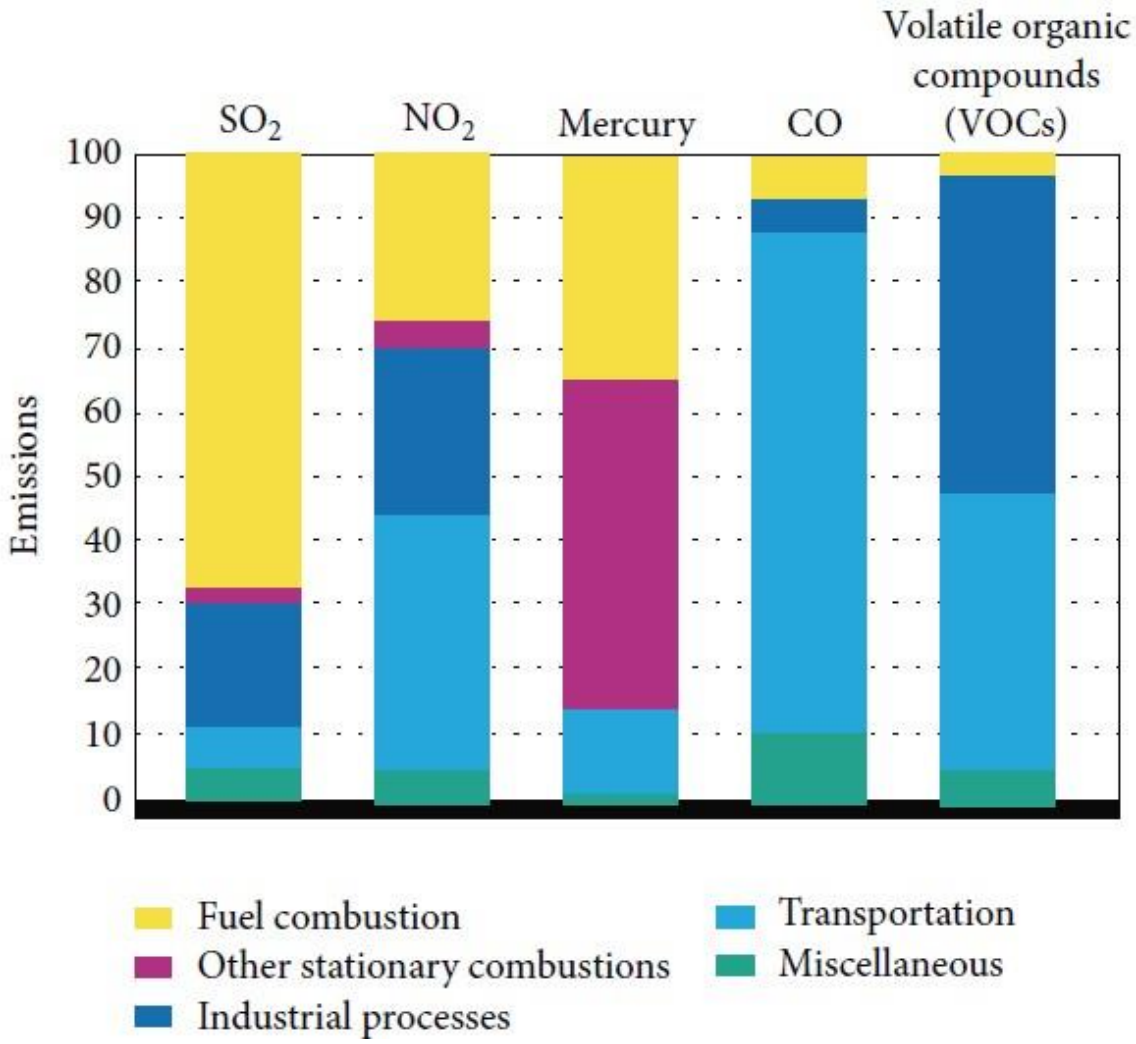

Figure 1.1: *The different factors that contribute to the emission of greenhouse gases [1.3].*

One technology that has been considered one of the solutions to curb the problem of greenhouse emission is hydrogen-based referred as hydrogen technology. This technology involves the production, transportation, storage and the use of hydrogen gas to produce electricity. Hydrogen is considered an energy carrier for future energy systems. The hydrogen cycle is shown in **Figure 1.2**.

Hydrogen as an energy carrier can minimize the complete dependence of global society on fossil fuels, which are insufficient and harmful to the environment [1.5]. It is regarded as a future energy carrier due to it being.

i. The most abundant chemical substance in the universe, accounting for about 75 percent of ordinary matter.

ii. It can be produced from water via water splitting process

iii. The only by product during the production of electricity using hydrogen is water.

iv. It is the richest in energy per unit mass

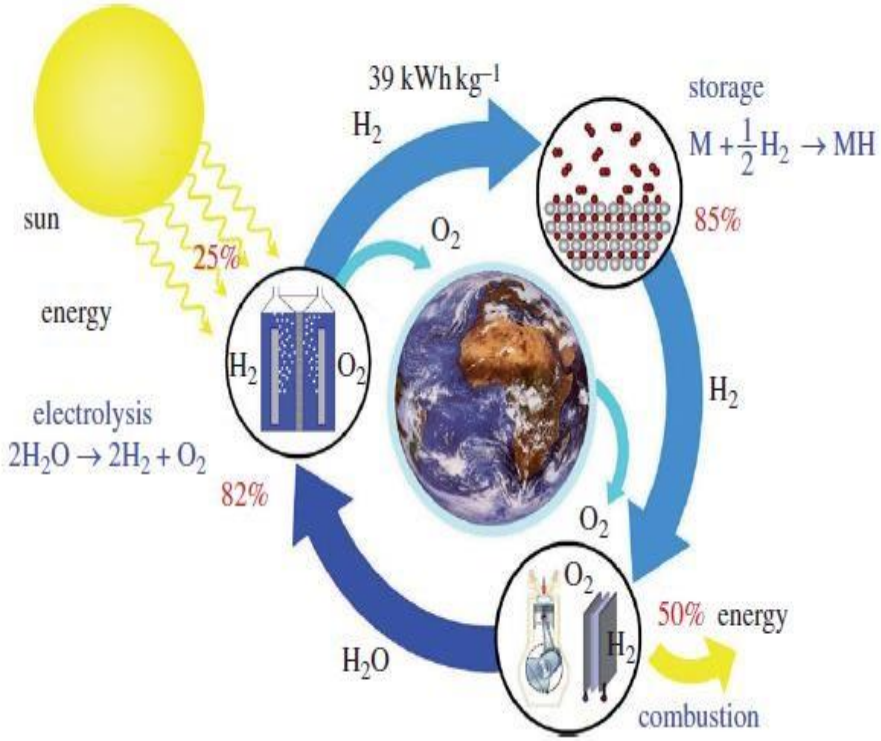

Figure 1.2: *Schematic of hydrogen cycle [1.8].*

Even though hydrogen technology is a promising technology for the future, there are still some challenges associated with it, i.e., clean production, transportation, and storage [1.3, 1.11]. Several

investigations have been done to solve some of the difficulties related to this hydrogen technology. Some of these investigations yielded promising results, but they were costly and can only be easily accessible: looking at standard methods of storing hydrogen such as storing hydrogen as a gas or a liquid using gas cylinders, these gas cylinders are costly and risky, thus preventing widespread use of hydrogen technology [1.13, 1.15, 1.17-1.18]. Furthermore, storing hydrogen as liquid had advantage of increasing the volumetric density of stored H_2, but the liquifying process is costly [1.13, 1.15, 1.17-1.18]. This work aims to contribute to solving the challenge of storage by investigating materials that can be suitable for storing hydrogen for an extended period in a safe manner and less costly.

1.2 Hydrogen fuel cell technology

Hydrogen cannot generate or produce electricity by itself without stripping an electron out of it. The electron stripping process can be achieved by employing fuel cell technology. Hydrogen fuel cell device converts chemical energy directly into electrical energy, water and heat being the only by-product [1.9, 1.24]. It can be employed in a diverse range of technologies. These include powering of buildings, cars, portable electronic devices and backup power systems [1.24]. Since fuel cells are electricity grid-independent, they are also considered an alternative for critical load functions such as data centres, telecommunications towers, hospitals, emergency response systems, and military applications for national defence [1.24]. Fuel cells for vehicles in comparison to conventional gasoline vehicles have desirable advantages such as reduction of carbon emissions, thus they are friendly to the environment [1.24].

1.3 Working principle of a hydrogen fuel cell

A fuel cell comprises of an anode catalyst (negative terminal), cathode catalyst (positive terminal), electrolyte and proton exchange membrane (PEM) between the two electrodes and an external circuit with a load, as shown in **Figure 1.3** [1.24]. The electricity generation process starts with

introducing H_2 gas into the anode electrode and O_2 gas into the cathode electrode. The catalyst in the anode electrode dissociates molecular hydrogen into atomic hydrogen, which is then stripped off its electron by the same catalyst in the anode. PEM selectively allows protons to flow to the cathode side of the cell

[1.24]. Electrons are attracted to the anode side and the external circuit enabling the load to glow. Protons reacts with oxygen to produce water and heat as the by-product of the whole process as shown in **Figure 1.3**.

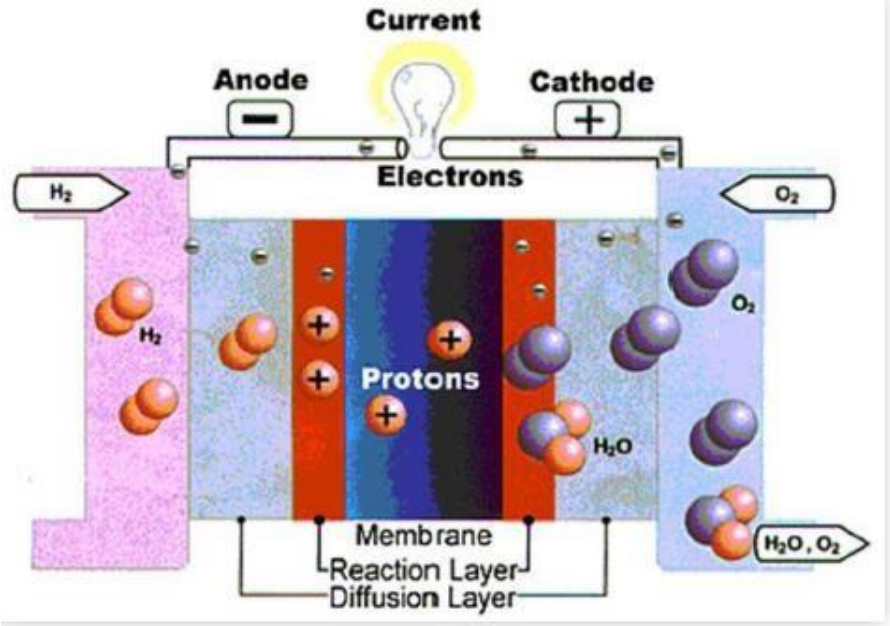

Figure 1.3: *Schematic representation of a fuel cell operation [1.24].*

1.4 Hydrogen storage overview

Hydrogen storage is a crucial challenge limiting the widespread commercialization of hydrogen-based energy [1.3, 1.20]. Hydrogen molecules can exist in different phases such as liquid, solid and gas. These phases are dependent on factors such as temperature, density and pressure. **Figure 1.4** depicts hydrogen phase dependency on pressure versus temperature reported in the literature [1.3, 1.12]

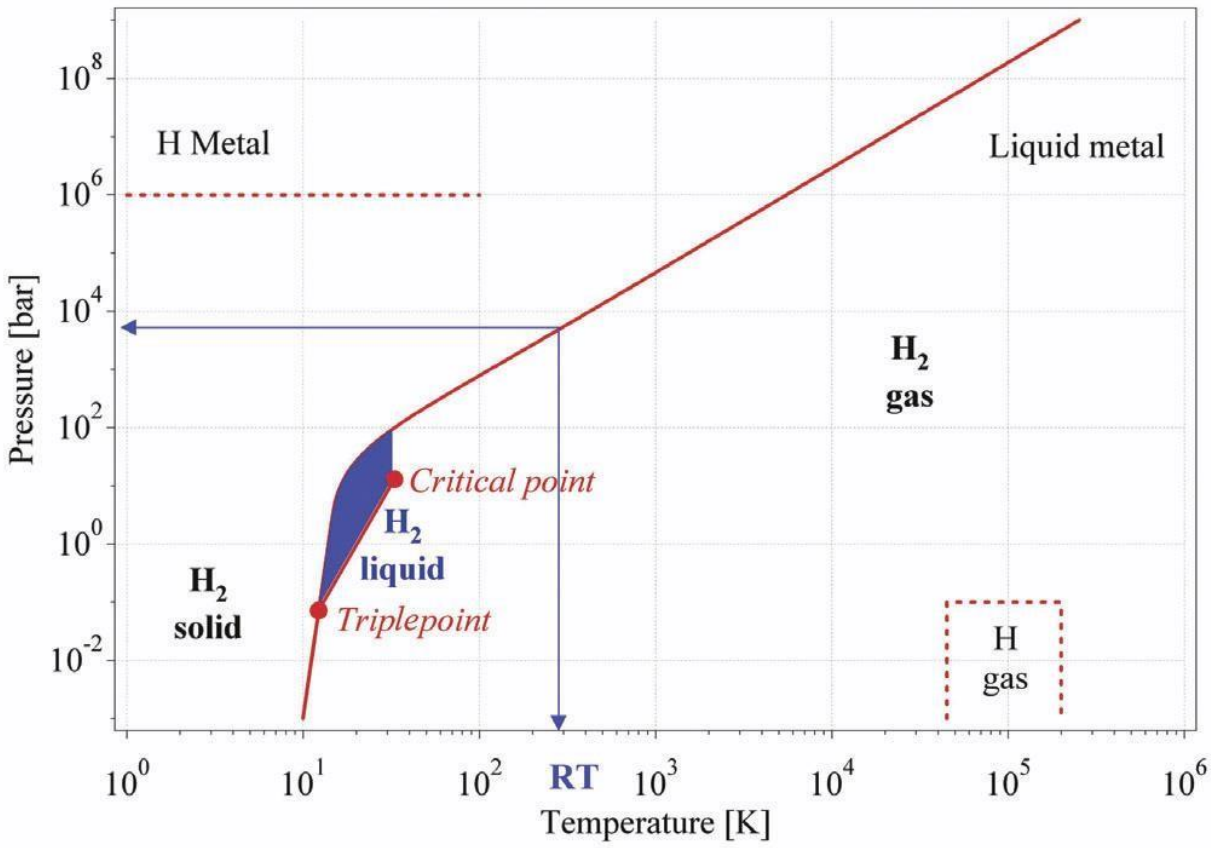

Figure 1.4: *Phase diagram for hydrogen [1.12].*

According to the phase diagram, H_2 can exist in different phases depending on the temperature and pressure. The solid form of H_2 exists at -262 °C and at 1 atm with a density of 70.6 kg/m^3, while the gaseous phase exists at 0°C and at 1bar with a density of 0.08988 kg/m^3. Its liquid phase can be found between the triple and critical points with a density of 70.8 kg/ m^3 at -253 °C [1.3, 1.12, 1.16].

1.5 Hydrogen storage

To achieve widespread use of hydrogen fuel technology, a cost-effective, reliable and safe storage mechanism need to be developed [1.3, 1.14, 1.15]. Its low volumetric density (VD) of 0.08988

kg/m^3 in its gaseous state makes it difficult to contain it at room temperature and standard pressure [1.3, 1.14, 1.20]. Therefore, various techniques of storing H_2 are currently being used while others are under investigation. These techniques will be discussed in the sub-sections below.

1.5.1 High-pressure gas cylinders

The current commonly used industrial method of storing H_2 is utilizing high-pressure gas cylinders. These gas cylinders can be able to contain high-density pure H_2 at high pressure [1.20]. This standard method holds a large amount of H_2 gas at a maximum pressure of 20 MPa t (200 bar). To achieve a much higher volumetric density of stored H_2 gas, ~36 kg/m^3, a pressure of 80 MPa t (800 bar) must be applied [1.13, 1.18]. However, the volumetric density (VD) of hydrogen molecules remains very low even after compression [1.19]. Due to low volumetric density, higher cost of high-pressure cylinders, and safety associated with these tanks, widespread use remains a challenge [1.13, 1.15, 1.17-1.18].

1.5.2 The liquid hydrogen

Another method of storing H_2 is by liquefying it. This method was found to be effective in increasing the volumetric density of stored H_2 [1.22]. The liquefying process can be achieved by lowering its temperature to -253 °C at ambient pressure [1.16, 1.22]. The volumetric density of liquefied hydrogen was found to be 70.8 kg/m^3 at -253 °C, which is slightly greater than that of compressed hydrogen (70.6 kg/m^3) [1.12,1.16,1.23]. However, this method has two critical challenges: high-energy requirements for the liquefaction process and the boil-off losses. During the liquefaction, about 40 % of the energy is used during this process [1.23]. Other factors that make this method to be expensive is the difficulty in maintaining liquid H_2 at low temperatures due to external heat gain from the surroundings, and the liquid hydrogen boils off. These factors remain a challenge to apply

this method in the area such as automotive and therefore impossible to consider it for widespread application.

1.5.3 **The metal hydrides**

Another method that has a great potential to be used as a mechanism of storing H_2 is storing H_2 as metal hydrides. Metal hydrides are compounds formed after the reaction of H_2 with metals, intermetallic compounds, and alloys [1.8, 1.18]. Storing hydrogen in this manner depends on its properties of reacting reversibly with hydrogen and keeping it safer at room temperature and standard pressure [1.15, 1.19]. The reaction of hydrogen with metal was firstly reported in 1866 by Graham, where absorption of hydrogen by Palladium (Pd) was observed [1.26]. This observation generated a comprehensive investigation on metals with hydrogen storage ability. **Table 1.1** provide metals with their hydrogen storage properties.

Table 1.1**:** *Metal hydrides and their storage properties [1.1].*

Metals	**Hydrides**	**Wt. % H**	**Pressure (bar)**	**Temperature (K)**
Pd	**$PdH_{0.6}$**	0.56	0.02	298
Mg	**MgH_2**	7.60	1	573
$LaNi_5$	**$LaNi_5H_6$**	1.37	2	298
ZrV_2	**$ZrV_2H_{5.5}$**	3.01	10_8	323
TiFe	**$TiFeH_2$**	1.89	5	303
Mg_2Ni	**Mg_2NiH_4**	3.59	1	555
TiV_2	**TiV_2H_4**	2.60	10	313

There are two classes of metal hydrides, namely binary and intermetallic metal hydrides. Binary hydrides have one metal element bonded to hydrogen and take the common form of MH_x, where M is the metal, H is hydrogen, and x is an integer number [1.18, 1.19]. AlH_3 is a binary metal hydride that is highly used with a gravimetric capacity of 10.1 wt. % and volumetric density of 1.48 g/ml [1. 15]. Intermetallic hydrides consist of more elements bonded to hydrogen, taking the form of $A_mB_nH_x$ compound. **A** is the rare-earth metal with high hydrogen affinity and forms stable hydrides, while **B** is the transition metal with low hydrogen affinity that and forms unstable hydrides [1.18, 1.19]. Intermetallic hydrides depend highly on the crystal structure of the compound, and their properties are based on the nature of the interaction between hydrogen atoms and the atoms of the host metal [1.21]. Some important intermetallic compounds include AB_5 in $CaCu_5$ structure, AB_2 (laves phase), AB in CsCl relative structure. A list of intermetallic hydrides that are commonly used is given in **Table 1.2**.

Table 1.2: *Intermetallic hydrides used for hydrogen storage [1.29].*

Intermetallic compounds	**Prototype**	**Hydride**
AB_5	LaN_5	$LaNi_5H_6$
AB_2	ZrV_2, $ZrMn_2$, $TiMn_2$	$ZrV_2H_{5.5}$
AB_3	$CeNi_3$, YFe_3	$CeNi_3H_4$
A_2B_7	Y_2Ni_7, Th_2Fe_7	$Y_2Ni_7H_3$
A_6B_{23}	Y_6Fe_{23}	$Y_6Fe_{23}H_{12}$
AB	TiFe, ZrN i	$TiFe_2$
A_2B	Mg_2Ni, Ti_2Ni	Mg_2NiH_4

However, AB_5, AB_2, and A_2B are the ones with the ability to absorb hydrogen. Even though intermetallic hydrides have high density by volume, they have density by mass, which is very low, which does not exceed 2 wt. % hence narrow their widespread use, especially in automobile applications. **Figure 1.5** shows the gravimetric and volumetric density of different metals and intermetallic hydrides. One of the intermetallic hydrides used commercially is $LaNi_5H_6$ with a volumetric density of 120 kg/m^3, higher than liquid hydrogen (70.8 kg/m^3) as illustrated by figure 1.5 [1.15]. Metal hydrides demonstrate high storage capacity as compared to standard storage methods such as liquid and gas. $LaNi_5H_6$ has 5.5×10^{22} H atoms/cm^3, while gas and liquid have 0.9 H atoms/cm^3 and 4.2 H atoms/cm^3 respectively [1.15].

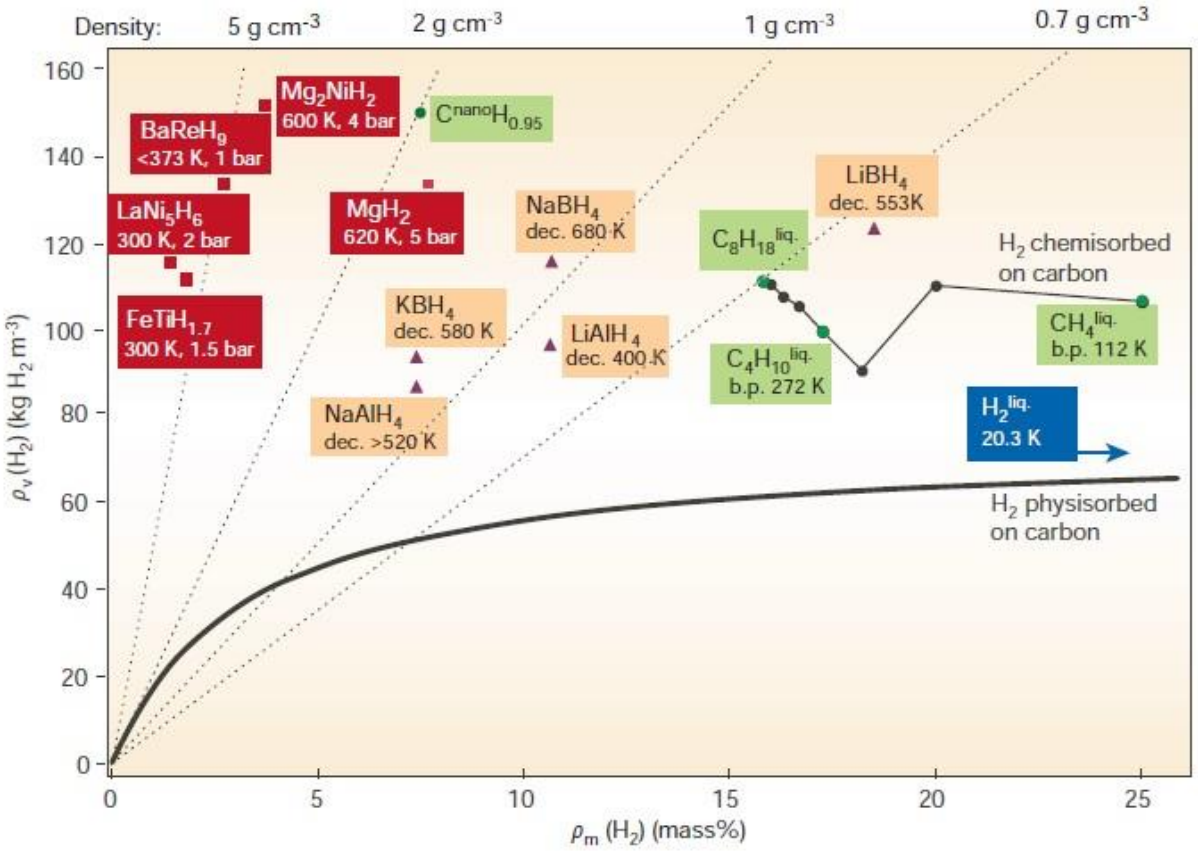

Figure 1.5: *Graph* of *the gravimetric and volumetric density of different metals and intermetallic hydrides [1.25].*

Due to some issues associated with standard storage methods (gas and liquid hydrogen), as discussed in the previous sections, Metal hydrides storage system has been considered a solution for storing hydrogen. Since they can absorb hydrogen at low temperatures and standard pressure, they are safer and energy efficient. They have high volumetric and gravimetric densities compared to hydrogen in their liquid and gas phases [1.15, 1.28]. However, hydrogen absorption kinetics is a significant concern for this storage system. Most potential metals and metals alloys such as Ti with the ability to store hydrogen cannot absorb hydrogen at room temperature [2.9]. The difficulty of these materials to absorb hydrogen is due to the passivation layer on the surface. This layer is formed from the reaction of metal surface atoms with hydrogen and oxygen to form thin oxides and hydroxides layer that cover the surface, preventing hydrogen uptake into the material at room temperature [2.21, 2.9]. The activation process in this regard is of significance before the hydrogenation process to remove the passivation layer on the surface.

Catalytic materials such as palladium are employed in this study to combat this problem since Pd can act as a catalyst for hydrogen molecule dissociation and a protective layer, thus helps hydrogen to diffuse into the material. Ion implantation is also used to address this significant drawback by modifying the surface properties of the material. Implantation of ions of desired elements with the ability to absorb hydrogen can remove the passivation layer on the surface and creates some lattice distortion, i.e., defects in the surface region that may accelerate the diffusion of hydrogen into the bulk of the metal matrix [2.21]. Implantation of ions it is also introduces extra solute atoms to bond with hydrogen molecules in some cases [2.1]. This method can improve the surface activation kinetics of Ti [2.21].

1.6 Aims and objectives of the study

Storing hydrogen as a solid (i.e., trapping it within metals) have been identified as a potential storage method, with the ability to enable the use of hydrogen as an energy carrier to be commercialized. Titanium (Ti) has been considered as a prospective storage material for hydrogen due to its high affinity to hydrogen. In this study, the investigation of hydrogen storage viability in **Pd /Ti /V /Pd /CP- Ti** is of the focus. The objectives of this study are to:

i. Investigate the effect of ion implantation of (Fe ions) on hydrogen absorption in **Pd/Ti /V/Pd /CP-Ti**

ii. Investigate the effect of ion implantation of (Fe ions) on phase transformation and microstructural evolution on **Pd/Ti /V/Pd /CP-Ti**

iii. Investigate the effect of temperature on hydrogen absorption in **Pd/Ti /V/Pd /CP-Ti**

iv. Investigate the effect of hydrogen on phase transformation and microstructural evolution on **Pd/Ti /V/Pd /CP-Ti**

1.7 Thesis outline

The thesis comprises five chapters. The background of the study, fuel cell technology, and the view on hydrogen storage techniques are detailed in chapter one. The absorption of hydrogen in metals, particularly the thermodynamics in the metal-hydrogen system, the effect of surface modification on hydrogen absorption, the improvement of hydrogen absorption on Ti-systems using ion implantation, and effect of palladium (Pd) coating on Ti for hydrogen absorption are given in chapter two. Chapter 3 discusses, description of the materials, the sample preparation procedure, and the experimental procedure used to carry out the investigation. The characterization techniques, including Rutherford backscattering spectrometry (RBS), Elastic recoil detection analysis (ERDA), scanning electron microscope (SEM), and X-ray diffraction (XRD), are discussed in chapter four.

Chapter five gives a detailed discussion of the results obtained from this investigation. The conclusion and the future work are presented at the end of this thesis.

1.8 References

[1.1] Adams, B. D., & Chen, A. (2011). The role of palladium in a hydrogen economy. *Materials Today*, 14(6), 282–289.

[1.2] Höök, M., & Tang, X. (2013). Depletion of fossil fuels and anthropogenic climate change-A review. *Energy Policy*, *52*, 797–809.

[1.3] Zacharia, R., & Rather, S. U. (2015). Review of solid-state hydrogen storage methods adopting different kinds of novel materials. *Journal of Nanomaterials*, *2015*.

[1.4] Midilli, A., Ay, M., Dincer, I., & Rosen, M. A. (2005). On hydrogen and hydrogen energy strategies I: Current status and needs. *Renewable and Sustainable Energy Reviews*, *9*(3), 255–271.

[1.5] Pan, H. Z., Wang, Y. L., He, K. H., Wei, M. Z., Ouyang, Y., & Chen, L. (2013). First-principles study of hydrogen adsorption on titanium-decorated single-layer and bilayer graphene's. *Chinese Physics B*, *22*(6).

[1.6] Nicoletti, G., Arcuri, N., Nicoletti, G., & Bruno, R. (2015). A technical and environmental comparison between hydrogen and some fossil fuels. *Energy Conversion and Management*, *89*, 205–213.

[1.7] Rosen, M. A., & Koohi-Fayegh, S. (2016). The prospects for hydrogen as an energy carrier: an overview of hydrogen energy and hydrogen energy systems. *Energy, Ecology and Environment*, *1*(1), 10–29.

[1.8] Züttel, A., Remhof, A., Borgschulte, A., & Friedrichs, O. (2010). Hydrogen: The future energy carrier. *Philosophical Transactions of the Royal Society A: Mathematical, Physical and Engineering Sciences*, *368*(1923), 3329–3342.

[1.9] Rayment, C. (2003). <Introduction to fuel cell tech.pdf>. Department of Aerospace and Mechanical Engineering, University of Notre Dame, IN, 46556, 11–12.

[1.10] Niaz, S., Manzoor, T., & Pandith, A. H. (2015). Hydrogen storage: Materials, methods and perspectives. *Renewable and Sustainable Energy Reviews*, *50*, 457–469.

[1.11] Stiegel, G. J., & Ramezan, M. (2006). Hydrogen from coal gasification: An economical pathway to a sustainable energy future. *International Journal of Coal Geology*, *65*(3–4), 173–190.

[1.12] Züttel, A. (2003). Materials for hydrogen storage. *Materials Today*, *6*(9), 24–33.

[1.13] Andersson, J., & Grönkvist, S. (2019). Large-scale storage of hydrogen. *International Journal of Hydrogen Energy*, *44*(23), 11901–11919.

[1.14] Dagdougui, H., Sacile, R., Bersani, C., & Ouammi, A. (2018). Hydrogen Storage and Distribution: Implementation Scenarios. *Hydrogen Infrastructure for Energy Applications*, 37–52.

[1.15] Durbin, D. J., & Malardier-Jugroot, C. (2013). Review of hydrogen storage techniques for on board vehicle applications. *International Journal of Hydrogen Energy*, *38*(34), 14595–14617.

[1.16] Makridis. (2016). Hydrogen storage and compression. *Methane and Hydrogen for Energy Storage*, *June* 1–28.

[1.17] Viswanathan, B. (2017). Hydrogen Storage. *Energy Sources*, 185–212.

[1.18] Züttel, A. (2004). Hydrogen storage methods. *Naturwissenschaften*, *91*(4), 157–172. [1.19] Yartys, V. A., & Lototsky, M. V. (2004). *An Overview of Hydrogen Storage Methods*. 75– 104.

[1.20] Document, W., Future, N. P. C., Fuels, T., Made, S., August, A., August, O., National, T., Council, P., Groups, T., & Papers, T. T. (2012). *Advanced Storage Technologies for Hydrogen and Natural Gas*.

[1.21] Rusman, N. A. A., & Dahari, M. (2016). A review on the current progress of metal hydrides material for solid-state hydrogen storage applications. *International Journal of Hydrogen Energy*, *41*(28), 12108–12126.

[1.22] Varin, R. A., Czujko, T., Wronski, Z. S., Prachi, P., Wagh, M. M., & Aneesh, G. (2009). Chapter 2 “Heart” of Solid-State Hydrogen Storage. *Advances in Energy and Power*, *4*(2), 11–22.

[1.23] Storage, H. (n.d.). C Hapter: S Ustainability and H Ydrogen. *Development*, 1–35.

[1.24] Kumar, A., & Sehgal, M. (2018). Hydrogen Fuel Cell Technology for a Sustainable Future: A Review. *SAE Technical Papers*, *2018-April* 1–11.

[1.25] Mazwi, S. (2016). Hydrogen storage in Ti-based coatings and Ti6Al4V alloy. Unpublished master's thesis, University of the Western Cape, Cape Town, South Africa.

[1.26] Jain, I. P., Lal, C., & Jain, A. (2010). Hydrogen storage in Mg: A most promising material. *International Journal of Hydrogen Energy*, *35*(10), 5133–5144.

[1.27] Yadav, V. (2014). *Emerging Materials and Thermal Issues for Hydrogen Fuel Storage*. *August 2012*.

[1.28] Pudukudy, M., Yaakob, Z., Mohammad, M., Narayanan, B., & Sopian, K. (2014). Renewable hydrogen economy in Asia - Opportunities and challenges: An overview. *Renewable and Sustainable Energy Reviews*, *30*, 743–757.

[1.29] Reuß, M., Grube, T., Robinius, M., Preuster, P., Wasserscheid, P., & Stolten, D. (2017). Seasonal storage and alternative carriers: A flexible hydrogen supply chain model. *Applied Energy*,*200*, 290–302.

Chapter 2

Literature review

2.1 Introduction

This chapter discusses relevant literature on the absorption of hydrogen in metals, particularly the thermodynamics in the metal-hydrogen system, the effect of surface modification on hydrogen absorption, the improvement of hydrogen absorption on Ti-system using ion implantation, and the effect of palladium (Pd) coating on Ti for hydrogen absorption.

2.2 Absorption of hydrogen in metals

2.2.1 Basic hydrogen absorption process

Understanding the basic principle and theory behind hydrogen absorption in metals is crucial because it is a cornerstone of the ability for metals to be utilized in the hydrogen economy. Factors governing the absorption process, storage and dehydrogenation require proper investigation. These include the activation energy, thermodynamics of the system under study, crystal structure, etc.

It is a well-known fact that hydrogen can react with several metals and metal alloys due to its high reactivity property, forming metal hydride and solid solution as illustrated in the reversible reaction 2.1 below [2.1, 2.3, 2.19].

$$Me + \frac{x}{2} H_2 \leftrightarrow MeH_x + Q \qquad (2.1)$$

Where Me represents a metal, MeH_x represents metal hydride formed after the reaction and x is the ratio of hydrogen to metal, Q is the heat of reaction [2.3].
The resulting metal hydride stoichiometry is dependent on the metal that is involved in the reaction.

For instance, the reaction between Ti and atomic H results in the formation of TiH_2, while that of Mg_2Ni and atomic H result in the formation of Mg_2NiH_4 [2.28]. Hydrogen can be incorporated into metal using several processes. These include physical adsorption (physisorption) and chemical adsorption (chemisorption). Before anything can happen far away from the surface, the hydrogen molecule and the metal are in their respective ground states [2.5]. As the hydrogen molecule approaches the metal surface, it gets attracted by the Van der Waals forces and results in a physiosorbed state.

Furthermore, as hydrogen further approaches the metal surface, dissociation of hydrogen molecules into two hydrogen atoms occurs, achieving the chemisorbed state. Once the chemisorbed hydrogen atoms overcome the surface barrier, they diffuse into the metal and form the lattice gas phase (α $phase$) [5]. The stable hydride phase (β-phase) is formed by increasing concentration of the hydrogen atoms, which occupies the interstitials sites of the host lattice [2.3, 2.5]. The processes involved in the absorption of hydrogen into the metal is shown in **Figure 2.1**.

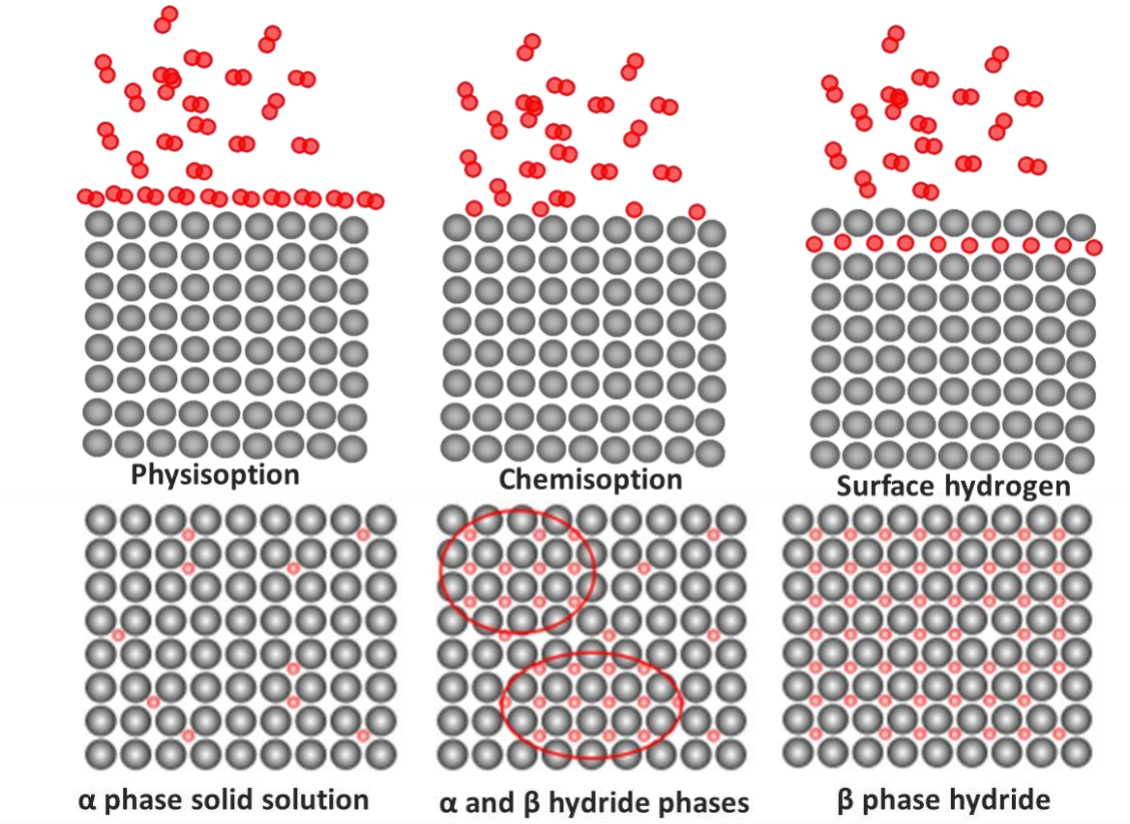

Figure 2.1: *Schematic representation of processes involved in the absorption of hydrogen into the metal [2.3].*

Hydrogenation, which is carried out using molecular hydrogen gas, involves numerous reactions during hydride formation (reaction of hydrogen and metal). These processes are governed by certain conditions such as temperature, pressure, treatment of the metal surface with catalyst, etc., that allow them to occur. **Figure 2.2** schematically display such processes in a one-dimensional energy curve [2.3, 2.5]. When the hydrogen molecule approaches the metal, it becomes attracted by the Van der Waals forces and forms a physiosorbed state. Before the hydrogen molecule diffuses into the bulk metal, it must dissociate, and forms chemisorbed state at the surface of the metal. After dissociation has taken place on the metal surface, the H atoms must diffuse into the bulk to form a M-H solid solution commonly referred to as a α-phase.

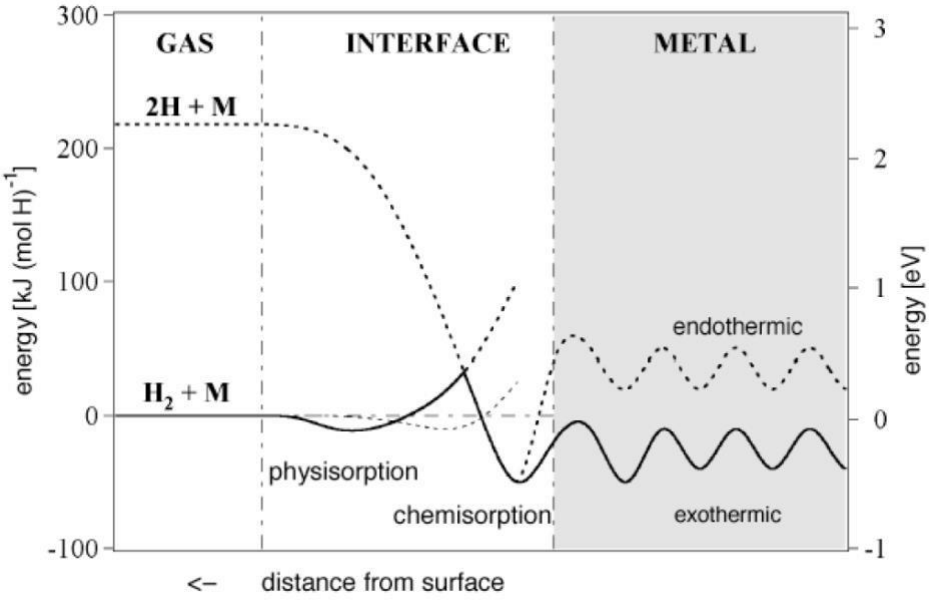

Figure 2.2: *One-dimensional energy curve for hydrogen absorption in metal [2.3].*

2.2.2 **Thermodynamics in metal-hydrogen system**

When the hydrogen molecule encounters metals surfaces, it gets dissociated into two hydrogen atoms and absorbed into the bulk metal [2.5]. These hydrogen atoms interact with atoms of the host lattice and interact among themselves. These interactions can form different phases depending on temperature, concentration, and pressure [2.4]. The absorption and desorption of hydrogen by metal can be understood by pressure-composition isotherms, as shown by Van't Hoff plot in **Figure 2.3** [2.7]. This Van't Hoff plot is very significant in hydride P-T stability to compare M-H systems and thermodynamic analysis of hydride formation [2.7]. At the lower hydrogen pressure below equilibrium pressure and low hydrogen content, hydrogen atoms penetrate the metallic lattice, then occupy interstitials sites to form a solid solution (usually called α-phase) [2.7, 2.8].

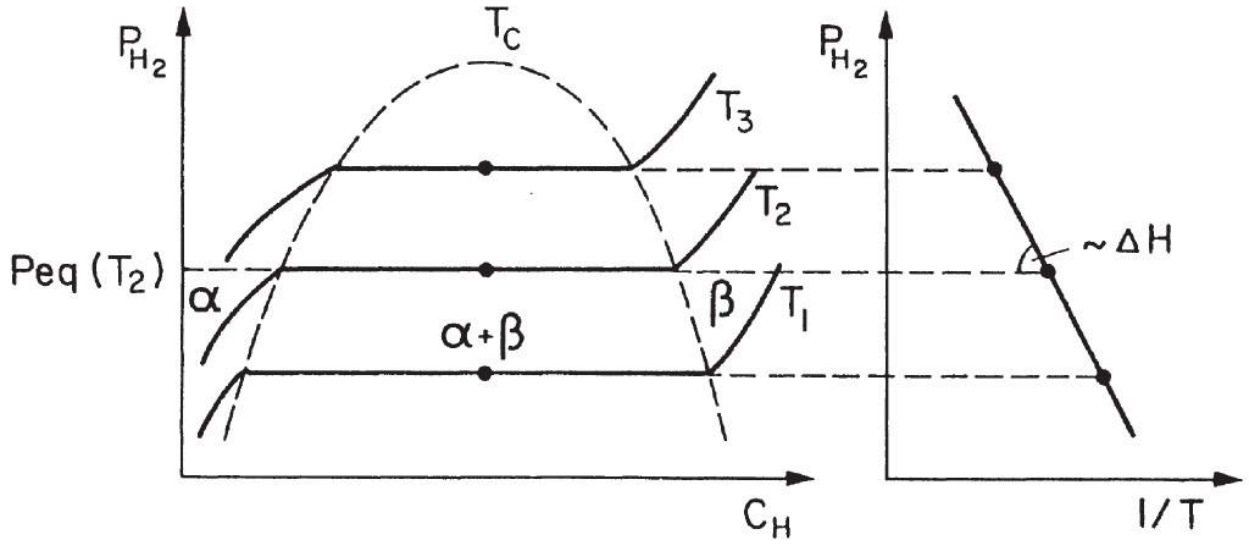

Figure 2.3: *Pressure-composition isotherms on the left and Van't Hoff plot on the right for the hydrogen absorption process in metals [2.7].*

The plot in **Figure 2.3** can be discussed: the increase in hydrogen pressure is directly proportional to the rise in hydrogen atoms concentration within the metal matrix. As the hydrogen pressure reaches an equilibrium point (plateau pressure), the H-H interactions become dominant, thus giving rise to the formation of the β-phase. At the plateau region, the α and β phases coincide, hence the $\alpha + \beta$ is the phase that exists. As hydrogen atoms concentration increases and the pressure rises above the plateau pressure, the β-phase becomes 100% dominant at the end right of the plateau region. The equilibrium pressure (the pressure value) decreases with the increase of the temperature but the width of the plateau as function of the hydrogen content increases with the increase of the temperature. Above the critical temperature, (T_c) the β-phase expands at the expense of the α-phase [2.7].

Furthermore, Van't Hoff expression (equation 2.2) describes the relationship between equilibrium pressures P_{eq}, temperature T, entropy, and enthalpy.

$$ln\left(\frac{p_{eq}}{p_o}\right) = \frac{\Delta H}{RT} - \frac{\Delta S}{R} \quad (2.2)$$

Where P_{eq} is the equilibrium pressure, P_0 is the standard pressure, ΔH is the enthalpy of the hydride formation, ΔS is the entropy of the hydride formation, R is the gas constant, and T is the absolute temperature.

2.3 Hydrogen absorption in Titanium and Titanium alloys

Titanium is one of the transition metals with atomic number 22, atomic weight of 47.867 g/mol, the density of 4.51 g/cm^{3,} and young modulus 120 GPa [2.6, 2.12, 2.14, 2.19]. Titanium and its alloys possess additional desirable properties such as strength to weight ratio, corrosion resistance, good stability at high temperatures, and they are cheap [2.6, 2.12, 2.14, 2.19]. These properties enable titanium to be used in various technology applications such as aerospace, marine, and medicine [2.6, 2.12, 2.14, 2.19].

Titanium exists in two phases depicted in **Figure 2.4**; referred to as the solid phase (α-Ti) and β-Ti [2.18]. At α-phase, titanium is solid up to β-transus temperature (882 ℃) and has a hexagonal closed packed structure (hcp) at this phase [2.10, 2.19]. Titanium transforms from α-Ti to β-Ti at a temperature from 882 ℃ up to the melting point (1670 ℃) and has a body-centred cubic structure (BCC). Crystal structures of both α-Ti and β-Ti are presented in **Figure 2.4** below with an indication of slip planes.

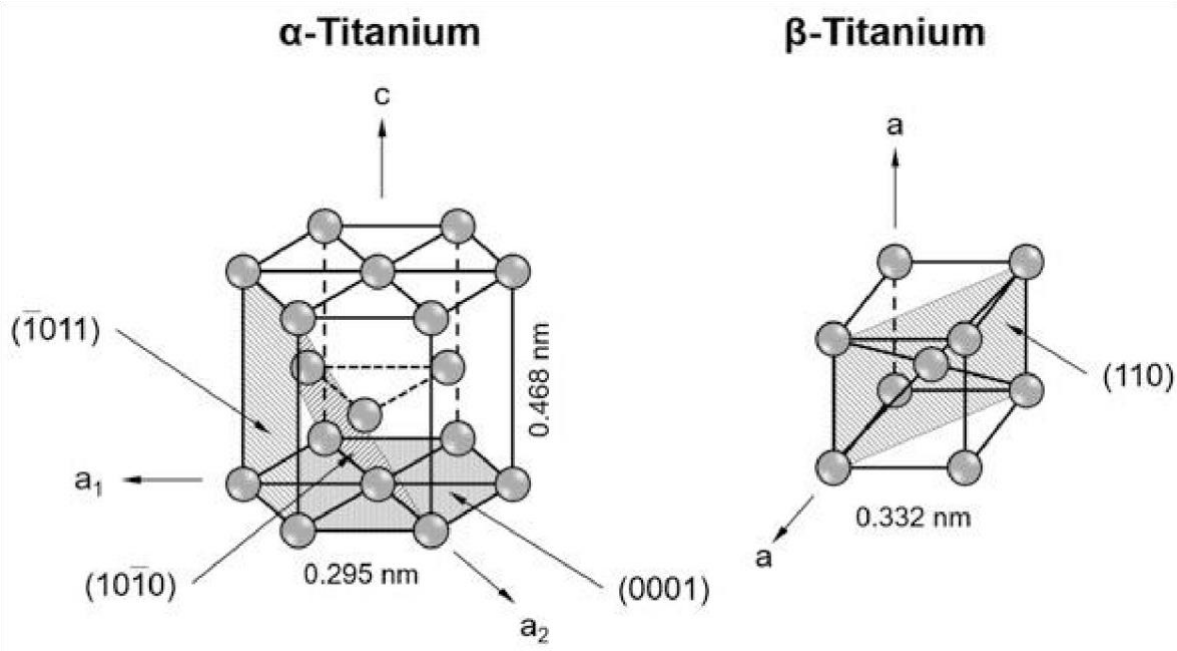

Figure 2.4: *Crystallographic structures of titanium [2.19].*

Titanium and titanium alloys are considered suitable candidate materials for hydrogen storage due to their high affinity for hydrogen, particularly at high temperatures, low density, and the ability to react reversibly with hydrogen [2.15-2.17, 2.19]. Hydrogen can also be absorbed at low temperatures by using the Ti-alloys such as Ti-6Al-4V, TiFe, etc. Titanium can pick up to more than 50 at % of hydrogen at a high temperature above 600 ℃ [2.11-2.13]. **Figure 2.5** demonstrates how hydrogen concentration increases as the temperature increases. It can also be observed that the threshold temperature for commercially pure titanium is close to 550℃; for the alloy, it is between 550℃ and 600℃. The solubility of hydrogen in Ti depends on hydrogenation experimental parameters such as temperature, time, pressure, and gas concentration [2.24].

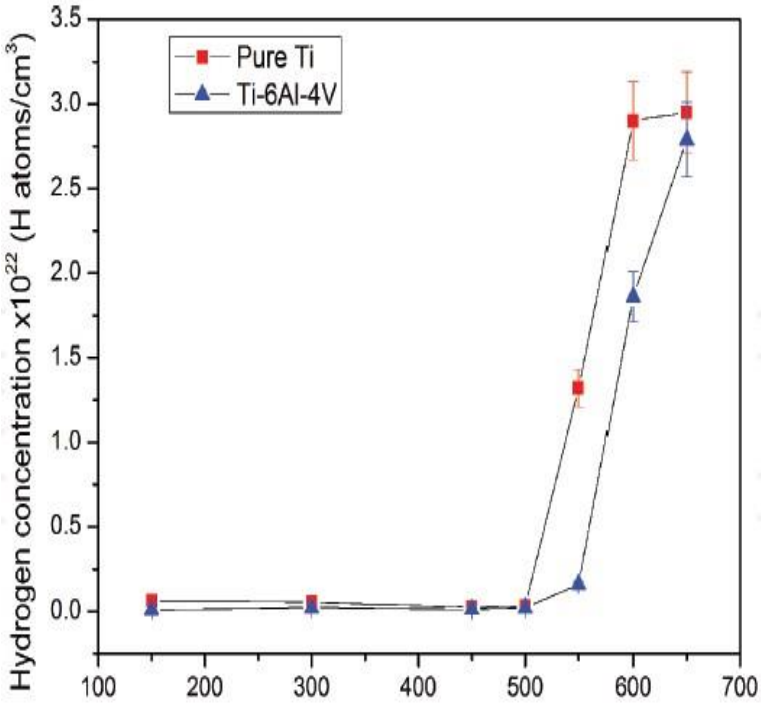

Figure 2.5: *Hydrogen concentration versus hydrogenation temperature for pure Ti and the Ti-6Al4V alloy [2.9].*

2.4 Phase transformation in Ti-H

When Ti reacts with atomic hydrogen, different phases are formed. These phases are depended on the content of hydrogen absorbed and temperature, as shown in **Figure 2.6**. At low hydrogen concentration, hydrogen forms an interstitial solid solution in the α-Ti and β-Ti phases and hydride phases at high hydrogen concentration [2.20]. The detailed Ti-H phase diagram is discussed below.

2.4.1 **Ti-H binary system**

The Ti-H phase diagram depicted in **Figure 2.6** can be summarized in the following manner: at the room temperature, hydrogen solubility in the α-Ti phase is 0.12 at. % and as the temperature increases, the hydrogen solubility also increases and the maximum value of 7.9 at. % is reached at the eutectoid temperature of 300 ℃ [2.20]. Hydrogen solubility remains constant up to 600 ℃. At a temperature above 600 ℃ hydrogen solubility in the α-Ti phase decreases up to β-transus temperature (882 ℃). Furthermore, absorbed hydrogen stabilizes the β-phase, thus reduces the βtransus temperature (882 ℃) to a eutectoid temperature of 300 ℃. At the eutectoid temperature of 300 ℃, the α-Ti, β-Ti, and δ-hydride phases exist with the hydrogen concentrations of 6.72 at. %, 39 at. %, and 51.9 at. % respectively.

At room temperature, three kinds of titanium hydrides (δ, ε, and ϒ) has been observed; δ –hydride (TiH_x) with x ranging between 1.5-1.99 has a face-centred cubic (FCC) and can exist as a mixture of α- δ or β- δ solid solutions [2.11, 2.12, 2.20]. At room temperature, δ-hydride forms a single-phase material at a hydrogen concentration of 60-66 at. %. At hydrogen concentration above 66 at. %, ε-hydride with distorted FCC exist [2.11, 2.12, 2.20]. Finally, at a hydrogen concentration of 1-3 at % metastable hydrides (ϒ) with tetragonal structure precipitate in the α-Ti (H) solid solution [2.11, 2.12, 2.20].

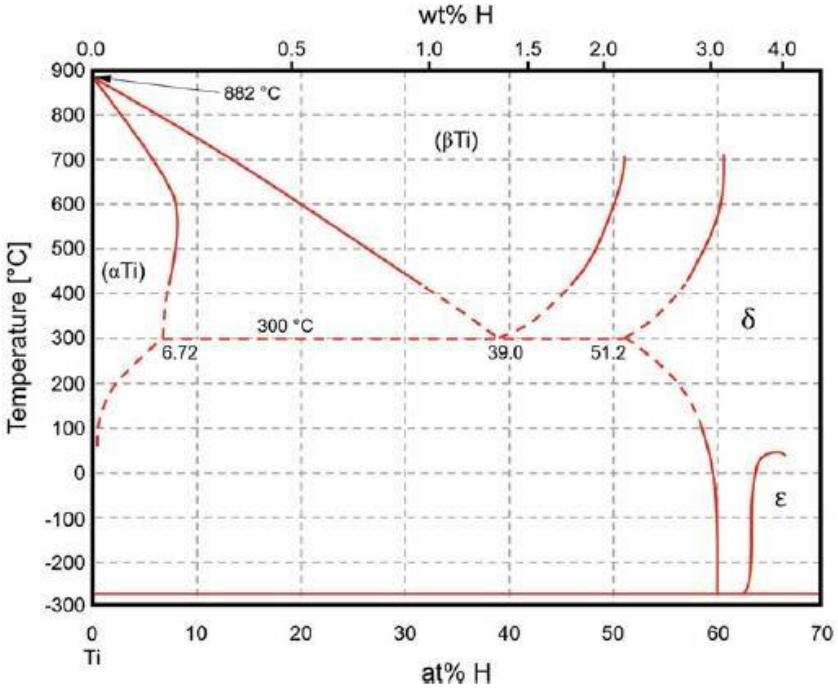

Figure 2.6: Ti-H equilibrium phase diagram [2.19].

2.5 Effect of surface modification on hydrogen absorption

Most potential metals and metals alloys such as Ti with the ability to store hydrogen cannot absorb hydrogen at room temperature [2.9]. The difficulty of these materials to absorb hydrogen is due to the passivation layer on the surface. This layer is formed from the reaction of metal surface atoms with hydrogen and oxygen to form thin oxides and hydroxides layer that cover the surface, preventing hydrogen uptake into the material at room temperature [2.21, 2.9].

The activation process in this regard is of significance before the hydrogenation process to remove the passivation layer on the surface. This activation process can be done by carrying out the hydrogenation process at high temperature and pressure, and by capping the material under investigation with catalytic layer, or by implanting energetic ions using ion implantation technique [2.9, 2.21, 2.23]; these processes are discussed in the section below

2.5.1 Metal treatment using ion implantation

Metals and their alloys Ti can store hydrogen due to its high affinity to hydrogen.

Still, they require structural treatment, among other processes, to absorb and store large amounts [2.9, 2.21]. Implantation of ions of desired elements with the ability to absorb hydrogen can remove the passivation layer on the surface and creates some lattice distortion, i.e., defects in the surface region that may accelerate the diffusion of hydrogen into the bulk of the metal matrix [2.21]. Implantation of ions does also introduce extra solute atoms to bond with hydrogen molecules in some cases [2.1]. This method can improve the surface activation kinetics of Ti [2.21]. During hydrogen implantation into Ti, the trapping mechanism depends on temperature and the fluence during implantation [2.22]. Lopez-Suarez et al. [2.22] reported that at a temperature above 273 K, hydrogen moves from the surface to the bulk and forms hydrides. Still, at a temperature around 273 K, the implanted hydrogen does not possess enough energy to activate and form hydride resulting in hydrogen atoms being trapped by the vacancies. The same behaviour takes place at low implantation fluence.

In the other report by Lopez-Suarez et al. [2.4], Ti samples were implanted with 5 keV H ions at room temperature at a fluence of $1 \times 10^{14}\ ions/cm^2$ prior hydrogenation; to improve the activation process. After implantation, they hydrogenated samples at temperatures 300, 450, and 650 ℃ in a 50% hydrogen and 50% argon atmosphere, at 1 atm pressure, and flux of 50 cc/min for 2 hrs. The ERDA results of hydrogenated implanted samples plotted against non-implanted samples are shown in **Figure 2.7**, displaying absorbed hydrogen. They observed improvement in the absorption of hydrogen due to implantation, even at temperatures below 550 ℃; which correspond to the reports by other researchers who reported high hydrogen content at threshold temperature of 550 ℃ as shown in figure 2.5-7 [2.9, 2.22, 2.32].

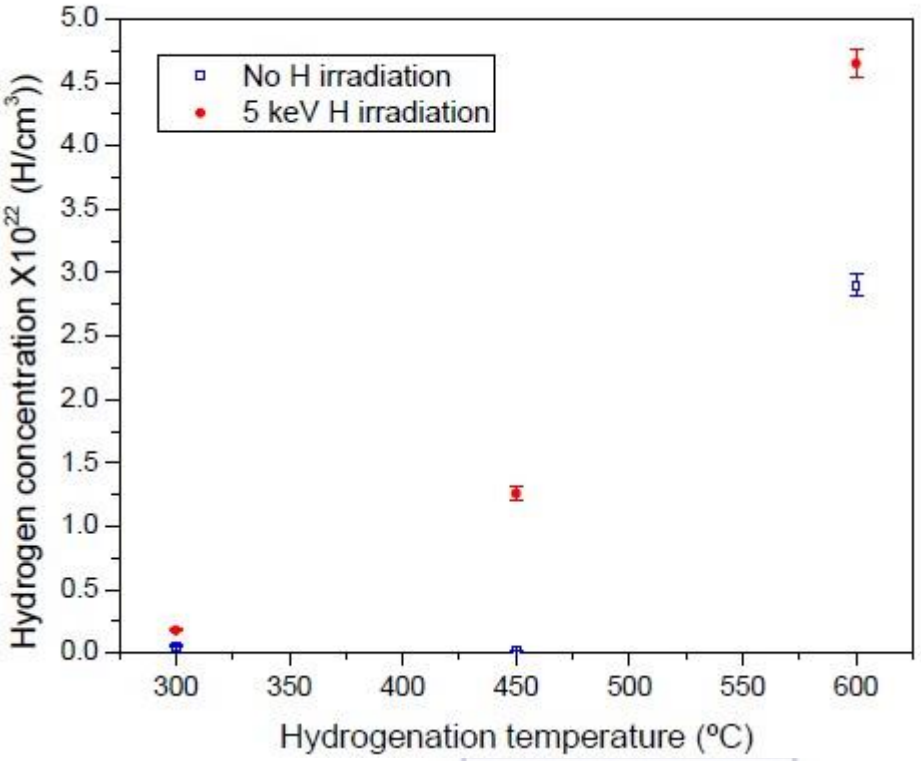

Figure 2.7: *Hydrogen concentration of hydrogenated samples of implanted and non-implanted [2.22].*

Lopez-Suarez et al. [2.22] also looked at the depth profile of implanted and non-implanted Ti hydrogenated at 450 ℃ as shown by **Figure 2.8**. At the surfaces, both implanted and non-implanted Ti possesses hydrogen peaks. The peak of non-implanted Ti is associated with the superficial hydrogen, and the peak of implanted Ti is related to the combination of superficial hydrogen and the implanted hydrogen. However, implanted Ti does show a hydrogen signal between 0.15-0.83 μm. Furthermore, implanted Ti contains hydrogen content beyond 0.83 μm in bulk. The above reports found that ion implantation done at a threshold temperature of 550 ℃ does improve hydrogen absorption. These reports showed enhancement of hydrogen absorption in Ti metal as a direct result of ion implantation as shown by the red curve. The blue curve which shows non implanted sample showed no enhancement of hydrogen absorption.

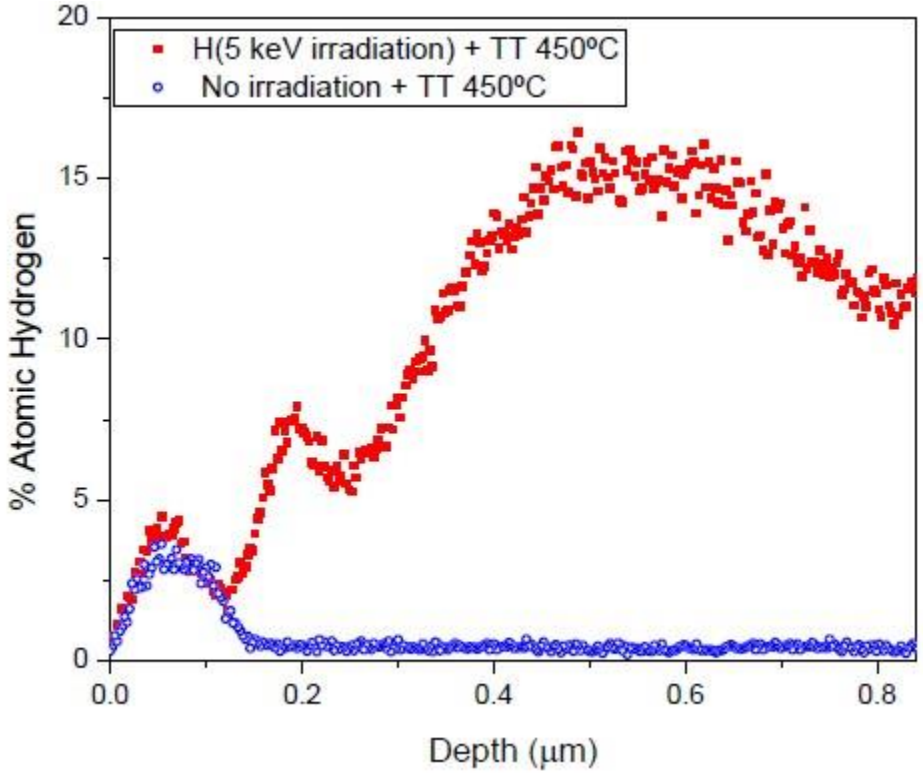

Figure 2.8: *Hydrogen depth profile of Ti hydrogenated at 450* ℃ *[2.9].*

2.5.2 Metal surface treatment using palladium (Pd) coating

Another alternative method to protect hydride forming materials from oxidizing is by capping Ti system with a thin metal catalyst film which is anti-corrosive and permeable for hydrogen [2.25, 2.32]. Palladium (Pd) was a suitable catalyst since it can absorb hydrogen at room temperature and atmospheric pressure. As a result, it has been a highly regarded material applicable in various hydrogen technologies [2.24, 2.32]. In hydrogen technologies, Pd is used as a catalyst to support the hydrogen absorption kinetics in titanium (Ti) by dissociating hydrogen molecules into atomic hydrogen, a protective layer to avoid further oxidation on Ti-system, selective membrane for hydrogen purification, and for hydrogen sensors [2.24,2.25-2.27, 2.32].

Several groups have studied Pd-based systems for hydrogen storage purposes, with most reporting enhancement of hydrogen absorption. For instance, Drogowska et al. [2.6] studied hydrogen

absorption in Pd/Ti/TiO_2/Si and Ti/TiO_2/Si thin films at room temperature. They observed that thin films without the Pd catalyst layer did not absorb any hydrogen; however, the thin films with the Pd layer on top showed some improvement in hydrogen absorption. Zaluski et al. [2.26] investigated the effect of catalytic Pd on TiFe alloy for hydrogen absorption. They reported that Pd coated TiFe could absorb hydrogen at normal conditions (room temperature and atmospheric pressure) without any activation before hydrogenation. Furthermore, an increase of hydrogen concentration from lower to higher was observed after the Pd layer modified the TiFe alloy. Topic et al. [2.32] investigated the hydrogen storage in Ti-Al6-4V alloy where all samples were hydrogenated at the optimal temperature of 550 ℃ in a gas mixture of 15 % hydrogen and 85 % argon gas were (31 ± 4) at. % was absorbed in this material. Furthermore, the Ti-Al6-4V alloy was coated with a catalytic Pd layer. As a result of this catalytic the Pd layer, the improvement of hydrogen absorption in this material increased from (31 ± 4) at. % to (36 ± 3) at. %.

Based on the above reports, the Pd coating does enhance hydrogen absorption kinetics on metallic hydrogen storage materials. The effect of the Pd catalyst was found to exhibit the spill over mechanism, as shown in **Figure 2.9** [2.24, 2.26].

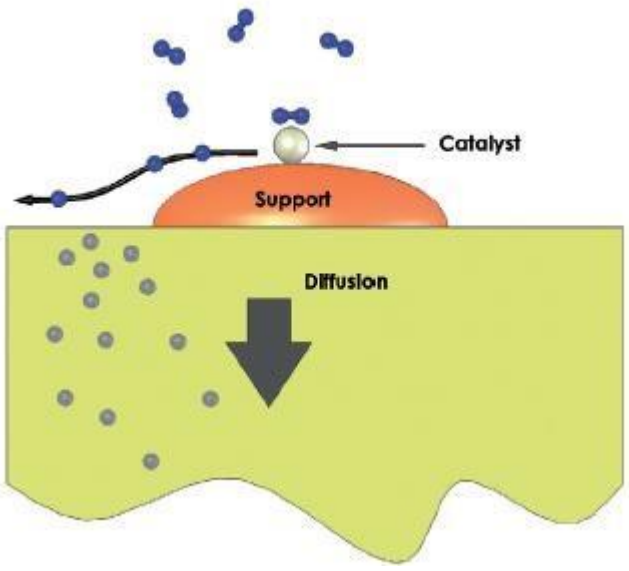

Figure 2.9: *Schematic of spill over mechanism [2.24].*

2.6 References.

[2.1] Sandrock, G. (1999). Panoramic overview of hydrogen storage alloys from a gas reaction point of view. *Journal of Alloys and Compounds*, *293*, 877–888.

[2.2] Wang, T., Eichhorn, F., Grambole, D., Grötzschel, R., Herrmann, F., Kreissig, U., & Möller, W. (2002). A new Ti/H phase transformation in the H2+ titanium alloy studied by x-ray diffraction, nuclear reaction analysis, elastic recoil detection analysis and scanning electron microscopy. *Journal of Physics Condensed Matter*, *14*(45), 11605–11614.

[2.3] Dornheim, M. (2011). Thermodynamics of Metal Hydrides: Tailoring Reaction Enthalpies of Hydrogen Storage Materials. *Thermodynamics - Interaction Studies - Solids, Liquids and Gases*.

[2.4] Kirchheim, R., & Pundt, A. (2014). Hydrogen in Metals. In *Physical Metallurgy: Fifth Edition* (Fifth Edition, Vol. 1).

[2.5] Remhof, A., & Borgschulte, A. (2008). Thin-film metal hydrides. *ChemPhysChem*, *9*(17), 2440–2455.

[2.6] Drogowska, K., Flege, S., Schmitt, C., Rogalla, D., Becker, H. W., Kim-Ngan, N. T. H., Brudnik, A., Tarnawski, Z., Zakrzewska, K., Marszałek, M., & Balogh, A. G. (2012). Hydrogen charging effects in Pd/Ti/TiO2/Ti thin films deposited on Si (111) studied by ion beam analysis methods. *Advances in Materials Science and Engineering*, *2012*.

[2.7] Systems, H. A. L., & Place, K. (1995). *Hydrogen-metal systems*. 135–166.

[2.8] Baldi, A., & Dam, B. (2011). Thin film metal hydrides for hydrogen storage applications.

Journal of Materials Chemistry, *21*(12), 4021–4026.

[2.9] López-Suárez, A. (2017). Effect of Absorption and Desorption of Hydrogen in Ti and Ti Alloys. *New Advances in Hydrogenation Processes - Fundamentals and Applications.*

[2.10] Peters, M., Hemptenmacher, J., Kumpfert, J., & Leyens, C. (2005). Structure and Properties of Titanium and Titanium Alloys. In *Titanium and Titanium Alloys*.

[2.11] Tal-Gutelmacher, E., & Eliezer, D. (2005). The hydrogen embrittlement of titanium-based alloys. *Jom*, *57*(9), 46–49.

[2.12] Tal-Gutelmacher, E., & Eliezer, D. (2004). Hydrogen-assisted degradation of titanium-based alloys. *Materials Transactions*, *45*(5), 1594–1600.

[2.13] López-Suárez, A., Rickards, J., & Trejo-Luna, R. (2003). Analysis of hydrogen absorption by Ti and Ti-6Al-4V using the ERDA technique. *International Journal of Hydrogen Energy*, *28*(10), 1107–1113.

[2.14] Furuya, Y., Takasaki, A., Mizuno, K., & Yoshiie, T. (2007). Hydrogen desorption from pure titanium with different concentration levels of hydrogen. *Journal of Alloys and Compounds*, *446–447*, 447–450.

[2.15] Tal-Gutelmacher, E., Gemma, R., Pundt, A., & Kirchheim, R. (2010). Hydrogen behavior in nanocrystalline titanium thin films. *Acta Materialia*, *58*(8), 3042–3049.

[2.16] Valencia, R., Chavez, E., & Flores, A. (1998). *In Titanium Plates at Low Pressure*. *23*(1), 15–18.

[2.17] Tarnawski, Z., & Kim-Ngan, N. T. H. (2016). Hydrogen storage characteristics of Ti– and V–based thin films. *Journal of Science: Advanced Materials and Devices*, *1*(2), 141–146.

[2.18] Analysis, T. (n.d.). Thermal Analysis Application Brief Detection of Beta Transus in Titanium Alloys. *Technology, 3–4.*

[2.19] Bergmann, C. P., & Alessioomalandruccolo, S. (n.d.). *Topics in Mining, Metallurgy and Materials Engineering Series Editor: Aerospace Alloys.*

[2.20] Checchetto, R., & Scardi, P. (1999). Structural characterization of deuterated titanium thin films. *Journal of Materials Research*, *14*(5), 1969–1976.

[2.21] Suda, T., Ohkawa, M., Sawada, S., Watanabe, S., Ohnuki, S., & Nagata, S. (2002). Effect of surface modification by ion implantation on hydrogenation property of TiFe alloy. *Materials Transactions*, *43*(11), 2703–2705.

[2.22] López-Suárez, A., Valencia, C. E., López-Patiño, J., Vargas, M. C., & Fuentes, B. E. (2015). Improvement of titanium hydrogenation by low energy ion irradiation. *International Journal of Hydrogen Energy*, *40*(11), 4194–4199.

[2.23] Mazwi, S. (2016). Hydrogen storage in Ti-based coatings and Ti6Al4V alloy. Unpublished master's thesis, University of the Western Cape, Cape Town, South Africa.

[2.24] Adams, B. D., & Chen, A. (2011). The role of palladium in a hydrogen economy. *Materials Today*, *14*(6), 282–289.

[2.25] Heller, E. M. B., Suyver, J. F., Vredenberg, A. M., & Boerma, D. O. (1999). Oxidation and annealing of thin FeTi layers covered with Pd. *Applied Surface Science*, *150*(1), 227–234.

[2.26] Zaluski, L., Zaluska, A., Tessier, P., Ström-Olsen, J. O., & Schulz, R. (1995). Catalytic effect of Pd on hydrogen absorption in mechanically alloyed Mg2Ni, LaNi5 and FeTi. *Journal of Alloys and Compounds*, *217*(2), 295–300.

[2.27] Takasaki, A., Furuya, Y., & Taneda, Y. (1998). Hydrogen uptake in titanium aluminides covered with oxide layers. *Metallurgical and Materials Transactions A: Physical Metallurgy and Materials Science*, *29*(1), 307–314.

[2.28] Liu, Y., & Pan, H. (2013). Hydrogen Storage Materials. In *New and Future Developments in Catalysis: Batteries, Hydrogen Storage and Fuel Cells*.

[2.29] Kojima, Y., Miyaoka, H., & Ichikawa, T. (2013). Hydrogen Storage Materials. In *New and Future Developments in Catalysis: Batteries, Hydrogen Storage and Fuel Cells*.

[2.30] Banerjee, S., & Mukhopadhyay, P. (2007). Interstitial Ordering. *Phase Transformations*, 719–781.

[2.31] Dedrick, D. E. (2008). Solid-state hydrogen storage system design. *Solid-State Hydrogen Storage: Materials and Chemistry*, 82–103.

[2.32] Topić, M., Halindintwali, S., Mtshali, C., Nsengiyumva, S., & Khumalo, Z. M. (2019). Hydrogen storage in Ti-based metal hydrides investigated by elastic recoil detection analysis (ERDA). *Nuclear Instruments and Methods in Physics Research, Section B: Beam Interactions with Materials and Atoms*, 450(April), 239–24.

Chapter 3

Material and methods

3.1 Introduction

This chapter describes the materials, the sample preparation procedure, and the experimental methods used to carry out the investigation.

3.2 Material description

In this study, 99.6 % purity of bulk material of commercially pure titanium (CP-Ti) supplied by the Good-Fellow company was used to prepare the samples to be investigated. Round discs with 10 mm diameter and 2 mm thickness were cut out of bulk CP-Ti. The schematic diagram of the prepared discs is illustrated in **Figure 3.1**.

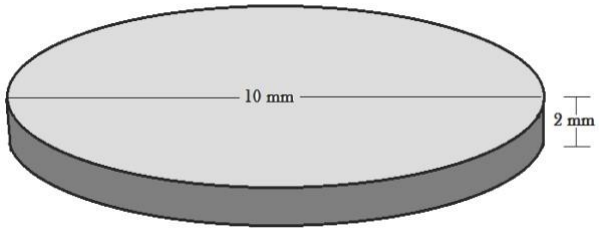

Figure 3.1: *The schematic diagram of the disc with 10 mm diameter and 2 mm thickness.*

3.3 Sample preparation

3.3.1 Polishing

The prepared disc samples from the bulk material of CP-Ti were polished using silicon carbide to remove scratches on the surface as a direct result of the cutting process to obtain a flat and smooth surface.

3.3.2 Thin film deposition

Before thin film deposition, all disc samples were ultrasonically cleaned using methanol for 20 minutes to remove contamination on the surface. Sample discs were dried using compressed argon gas and then transferred into the electron beam evaporator chamber. The target materials (Ti, Pd, and V) with 99.9% purity were placed on separate copper crucibles inside the chamber, with CP-Ti substrate discs carefully mounted on sample holders inside a vacuum chamber. The vacuum chamber was pumped down from atmospheric pressure to 10^{-7} mbar.

Sequential selective deposition of films was done by evaporating target materials using a high vacuum electron beam evaporator. These were done in the following manner: Ti (layer 5) on top of the CP-Ti substrate disc, Pd (layer 4), V (layer 3), Ti (layer 2), and Pd (layer 1 – surface layer) with an intention of forming the CP-Ti (substrate)/Pd (25 nm)/V (50 nm)/Ti (50 nm)/Pd (25 nm) multi-layered structure. The thickness of the multilayer films was monitored and recorded using a crystal monitor mounted inside the chamber.

The mechanism of electron beam evaporation used in film preparation is depicted in **Figure 3.2**. The beam of electrons was generated by applying a 5 kV voltage to the tungsten filament. This electron beam was directed onto the target materials. During the electron beam-target interaction, the kinetic energy of electrons was transferred onto the atoms on the surface of the target material resulting in the conversion of the kinetic energy of the electrons into thermal energy, causing the

atoms of the target on the surface to leave the surface through evaporation processes. The evaporated particles or atoms form the thin films on the substrate. The rate of deposition was kept as 0.6 Å/s.

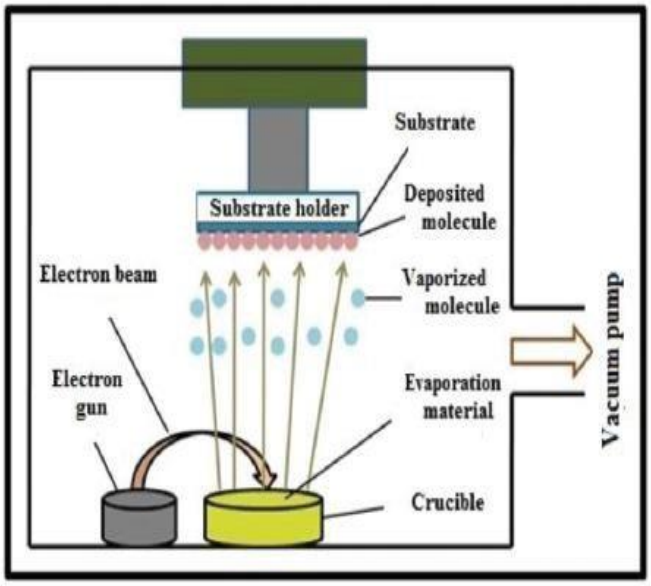

Figure 3.2: *Schematic diagram of e-beam evaporator [3.1].*

3.4 Ion implantation and SRIM simulation

3.4.1 . Ion implantation

Ion implantation is a critical non-equilibrium doping technique used to induce changes in properties of solid materials [3.2-3.5]. This technique involves the accelerating of energetic ions of desired elements through a potential difference directed towards the target material. The energy of the accelerated ions is usually in keV to MeV ranges depending on the desired depth to be reached [3.6, 3.7]. When the energetic ions penetrate the surface of the target material, they interact with the atoms of the target material, as shown by **Figure 3.3** (a – b), causing the lattice imperfections or disorders [3.6]. The defects caused by the implanted ions are responsible for modifying the physical,

chemical, electrical, and optical properties of the surface and subsurface layers of the target material [3.5-3.9].

(a)

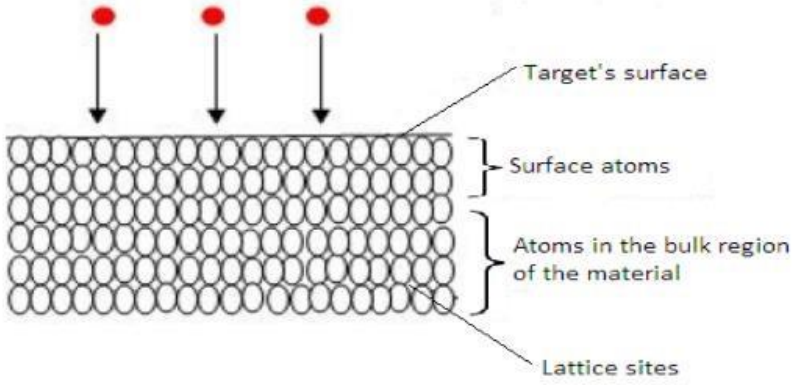

(b)

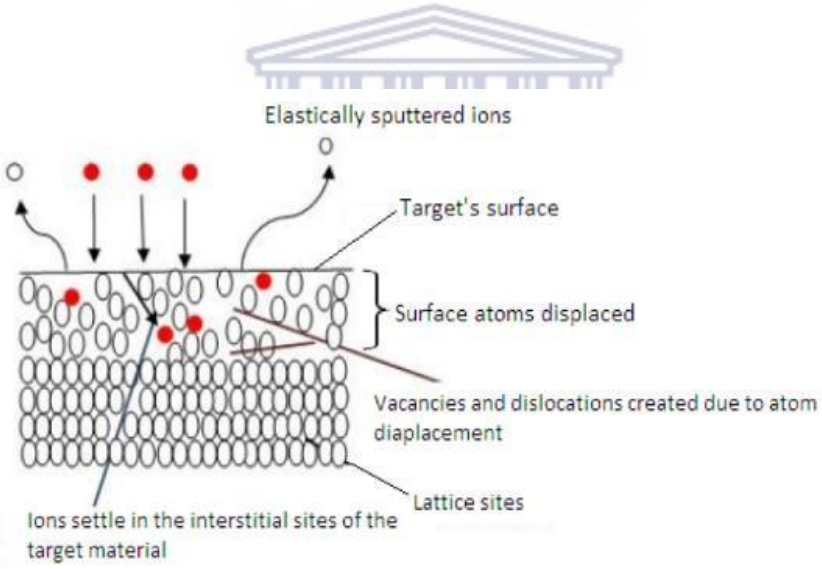

Figure 3.3: *Schematic representation, showing ion-solid interaction, (a) the crystalline material before implantation and (b) the crystalline material after implantation with possible interaction during implantation [3.10].*

.

Ion implantation has been applied in a various field such as microelectronics production, in academics as a research tool for ion-solid interaction investigation, and synthesis of new materials due to some

desirable advantages it possesses [3.2-3.4]. Ion implantation can modification the surface properties of the material without altering the bulk material. The energy and the ion fluence are used to control the depth and the implant. The conventional rules of solubility do not limit the choice of implant. Hence any ion of choice can be implanted [3.4, 3.7-3.9, 3.11].

Besides being the preferable doping technique, it has a significant drawback in creating lattice defects, causing undesirable structural damage. Thermal treatment can be used to treat these structural damages. However, the damage caused by ion implantation could significantly improve the properties of the material, particularly in this investigation.

3.4.2 Basic physics of ion implantation.

When the energetic ion bombards the surface of the solid material, it interacts with the stationary atoms of the host material; as a result of ion-target interaction, the ion loses its energy [3.4, 3.6, 3.7]. The energy loss is dependent on several parameters, such as ion energy *(E)*, the mass of the ion *(M_1)*, and the mass of the target material *(M_2)* [3.7]. The energetic ions lose their energy via two main energy loss processes. These include (i) the electronic energy loss process where ions interact with the electrons of the target material through inelastic collision, and (ii) the nuclear energy loss process, which is due to the interaction of ions with the nuclei of the target material. Other processes that also result from the interaction of energetic ions with target atoms are radiative processes such as bremsstrahlung and Cerenkov radiation [3.6, 3.9]. All these processes are energy dependent. Hence, they all contribute differently to the energy loss by the ion along its trajectory [3.6, 3.9]. By summing the nuclear, electronic, and radiative terms, the total energy loss by the incident ion with penetration depth x can be determined. Mathematically, the total energy loss by the incident ion is expressed as:

$$\left(\frac{dE}{dx}\right)_t = \left(\frac{dE}{dx}\right)_n + \left(\frac{dE}{dx}\right)_e + \left(\frac{dE}{dx}\right)_r \quad (3.1)$$

Where subscripts n, e, and r represent nuclear, electronic, and radiation loss, respectively. Since the energy loss due to radiation is minimal, it is normally neglected; hence the equation (3.1) becomes:

$$\left(\frac{dE}{dx}\right)_t = \left(\frac{dE}{dx}\right)_n + \left(\frac{dE}{dx}\right)_e \tag{3.2}$$

By normalizing the rate of the energy loss with atomic density N (atoms/cm^3), we obtain the stopping cross-section S with units (eV cm^2/atom) [7] which is defined as:

$$S = \frac{1}{N}\left(\frac{dE}{dx}\right)_t \tag{3.3}$$

Hence the total stopping cross-section can be expressed as the sum of nuclear stopping cross-section and electronic stopping cross-section:

$$S_t = S_n + S_e \tag{3.4}$$

Both stopping powers increase with energy and reach their maximum value, and then after that decrease [3.6, 3.14]. Nuclear stopping dominates at low energies, and electronic stopping dominates at higher energies [3.3, 3.4, 3.8], as shown in **Figure 3.4**.

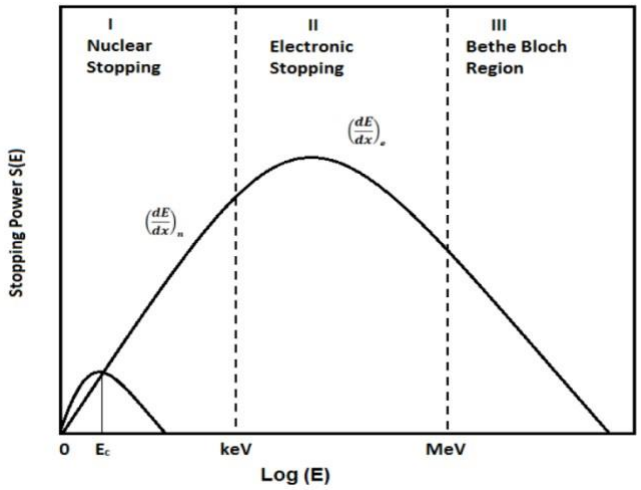

Figure 3.4: *Plot showing dominance regions of electronic and nuclear stopping of*

the ion as a function of energy (plotted logarithmically). E_c is critical energy in which electronic and atomic stopping are comparable [3.10].

3.4.3 **The electron energy loss**

The electron energy loss mechanism is due to the inelastic interaction between energetic ions and electrons of the target material. As a result, active ions causing the excitation and ionization of the target electrons [3.3, 3.7, 3.9, 3.12]. Electronic energy loss predominates at high velocities, intermediate energies, and lower ion mass [3.3, 3.8], as shown in **Figure 3.5** Since this mechanism is associated with high velocities, resulting in less ion-electron interaction time, leading to few lattice displacements [3.9, 3.12].

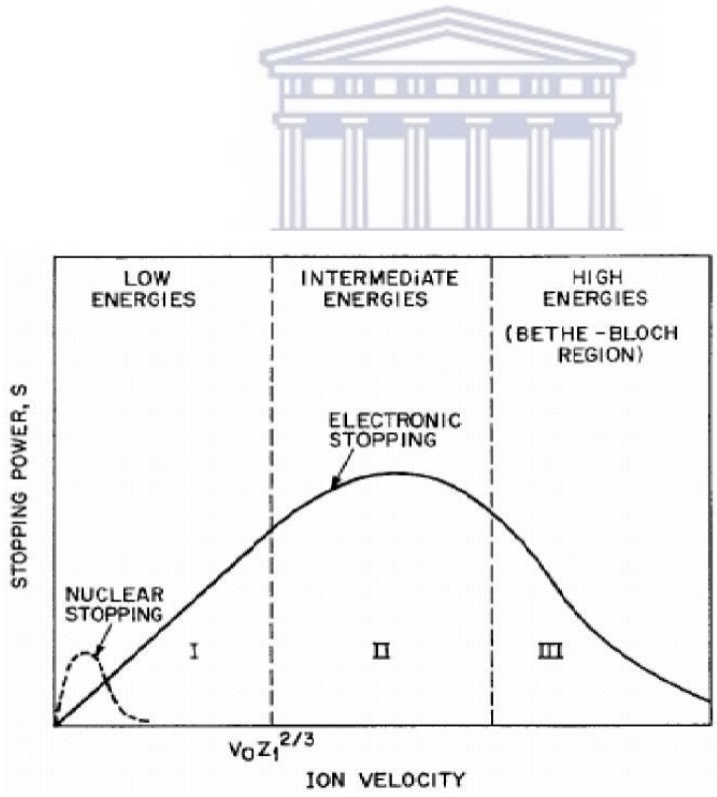

***Figure 3.5**: Plot showing electronic and nuclear stopping of the ion as a function of ion velocity [3.5].*

Several models that describe electronic stopping that has been developed over several decades. These models are based on comparing of incident ions in the three regions (low, intermediate, and high) with Bohr velocity, $V_o = e^2/\hbar$, where e and $\hbar$ are the electron charge and Plank's constant, respectively. In the first region, where the incident is $v < Z^{2/3}{}_1 v_0$, the electronic stopping force is described by the Firsov and Lindhard-Scharff-Schiott (LSS) [3.2, 3.12] theories. The general expression of electronic stopping cross-section was derived by Lindhardt, Scharff, and Schiott (LSS) [3.7, 3.12] and is given as:

$$S_e(E) = 3.83 \frac{Z_1^{\frac{7}{6}} Z_2}{\left(Z_1^{\frac{2}{3}} + Z_2^{\frac{2}{3}}\right)^{\frac{3}{2}}} \left(\frac{E}{M_1}\right)^{\frac{1}{2}} \tag{3.5}$$

Where Z_1 and Z_2 are ion and target atomic numbers, respectively, M_1 is ion mass, and E is the current energy of the ion. From the expression (3.5) above, it is evident that the electronic stopping cross-section is proportional to the ion velocity ($E^{1/2}$), which is:

$$S_e(E) \propto E^{\frac{1}{2}} \tag{3.6}$$

Lindhardt-Scharff further expressed the electronic stopping cross-section in a reduced form which is dimensionless and is given as:

$$S_e(\varepsilon) = -\left(\frac{d\varepsilon}{d\rho}\right)_e = -K_L \varepsilon^{\frac{1}{2}} \tag{3.7}$$

Where,

$$K_L = \frac{Z_1^{\frac{2}{3}} Z_2^{\frac{1}{2}} \left(1 + \frac{M_2}{M_1}\right)^{\frac{3}{2}}}{12.6 \left(Z_1^{\frac{2}{3}} + Z_2^{\frac{2}{3}}\right)^{\frac{3}{4}}}$$

ρ is density, $M_{1 \text{ and }} M_2$ are ion and target masses respectively, and Z_1 and Z_2 are the ion and target atomic numbers respectively.

In the intermediate and third regions, where the incident is $v \sim Z^{2/3}{}_1 v_0$ and $v >> Z^{2/3}{}_1 v_0$, respectively, Bohr and Bethe describe the electronic stopping force – Block theories are given below [3.6, 3.13].

$$S = \frac{4\pi {Z_1}^2 Z_2 e^4}{m_e {v_1}^2} \left[ln\left(\frac{2m_e {v_1}^2}{I}\right) + ln\left(\frac{1}{1-\beta^2}\right) - \beta^2 - \frac{c}{Z_2}\right] \quad (3.8)$$

Where m_e is electron mass, v_1 is the projectile's velocity, $\beta = v/c$ where c is the speed of light, $I = Z_2 10$ (eV) is the average ionization potential, and C/Z_2 is the shell correction.

3.4.4 The nuclear energy loss

The nuclear energy loss mechanism is due to the interaction between the incident ions and target atom's nuclei [3.3, 3.8]. This energy loss mechanism results from the scattering projectile by the screened nuclear potential of the target, and this phenomenon is referred to as Rutherford backscattering [3.8, 3.12]. Interactions during this mechanism are elastic [3.3, 3.8]. Nuclear energy loss predominates at lower energy E and high Z_1 [3.7]. In binary collision from **Figure 3.6**, the interaction between the incoming ion of mass M_1, atomic number Z_1, energy E_0, and momentum P_0 and target atom of mass M_2 and atomic number Z_2 at rest at a distance r apart can be described by the scattering between two positively charged nuclei screened by the cloud's electrons [3.3] as:

$$V(r) = k\frac{Z_1 Z_2 e^2}{r}\chi(r) \tag{3.9}$$

Where $\chi(r)$ is the screening function, and it is given as:

$$\chi(r) = 0 \; if \; r \to \infty$$

$$1 \; if \; r \to 0$$

The nuclear stopping cross-section is given as:

$$S_n = N\frac{\pi^2}{2}E^{-2}a\left[\frac{Z_1 Z_2 M_1}{M_1 + M_2}\right] \tag{3.10}$$

Where N is the atomic density, a is the lattice parameter, Z_1 and Z_2 are ion and target atomic target numbers, respectively. M_1 and M_2 are ion and target masses, respectively. Equation 3.8 can depict that nuclear stopping power is proportional to the inverse square of the energy. The total amount of energy deposited by atomic collision is called Nuclear Displacement. If the energy of the atoms is below this energy, there will be no more damage caused by nuclear stopping-energy [3.10].

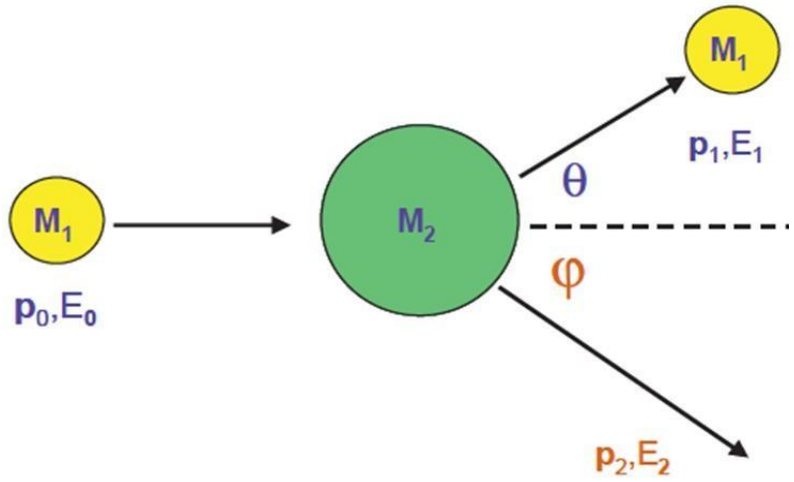

Figure 3.6: *Schematic representation of binary interaction between an incident ion of M_1 and the target of mass M_2 [3.3].*

3.4.5 Ion range and distribution

When ions travel through the target material, they undergo collisions with the electrons and nuclei of the target material and comes to rest inside target material after losing all their energies [3.14]. The ions cover a certain distance before they can finally come to rest. That distance is called a range; the vector component into the same direction of the incident ion and perpendicular to the surface is called the projected range [3.7, 3.14]. **Figure 3.7** illustrates the two quantities where R and R_p represent the range and project range, respectively.

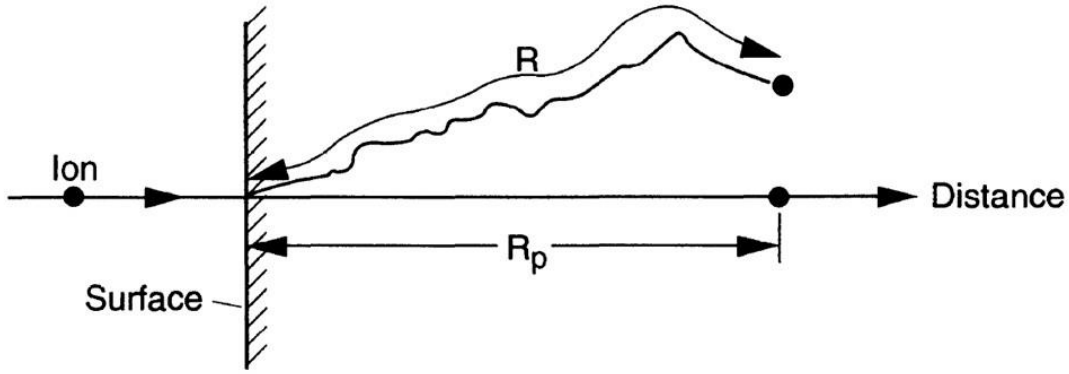

Figure 3.7: *An Illustration of range R and projected range R_p [3.7].*

If $S_n(E)$ and $S_e(E)$ are known, the total distance covered by an ion before it can come to rest (Range) with initial energy E_0 can be obtained by integrating the rate at which energy is lost with the path length, which is given by (equation 3.3), which results in:

$$R(E) = \int_0^R dx = \frac{1}{N}\int_0^{E_0} \frac{dE}{[S_n(E)+S_e(E)]} \tag{3.11}$$

Where N the atomic density of the target material, E_0 is the initial energy of the incoming ion, S_n and S_e are nuclear and electronic stopping, respectively.

The movement and stopping of an ion during the implantation process are random, resulting in the variation of collision sequence, subsequence ion deflection, and total path length at which ion will stop concerning each ion [3.5, 3.7, 3.10]. Hence the ion distribution will result in a Gaussian shape as shown in **Figure 3.8** (a-b). These can be approximated by looking at the Gaussian distribution, which is described by probability function and is characterized by a projected range (R_p) which describes the penetration depth measured from the surface of the target, straggling(ΔP_p), and ion fluence (the total number of ions per unit area). Mathematically, depth distribution is given as:

$$N(x) = \frac{\varphi}{\Delta R_p (2\pi)^{\frac{1}{2}}} exp\left[-\frac{1}{2}\left(\frac{x-R_p}{\Delta R_p}\right)^2\right] \tag{3.12}$$

Where φ is the fluence. The concentration of the implanted ions in terms of depth x is given by:

$$C(x) = c_p exp\left[\frac{(x-x_p)^2}{2\pi\Delta R_p}\right] \tag{3.13}$$

Where Cp is the height of the Gaussian distribution (see figure 3.9), the range straggling is given by:

$$\Delta R_p = \sqrt{\frac{1}{\varphi}\int_{-\infty}^{\infty}(x - R_p)^2 C(x)dx} \tag{3.14}$$

In some, the skewness (describing the degree of symmetry of distribution) and kurtosis (describing the presence of tail extension in the distribution) of the Gaussian distribution peak exist. Positive skewness signifies asymmetric tail towards the positive values, while negative skewness is towards the negative values of the distribution peak.

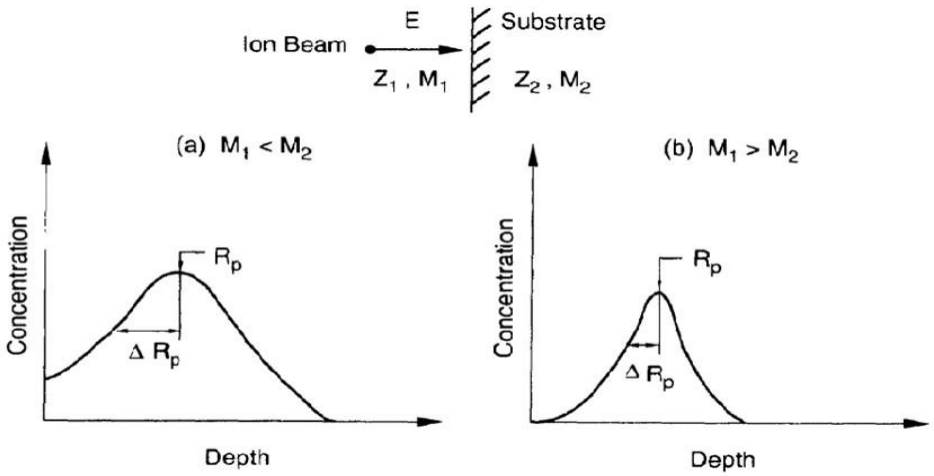

Figure 3.8: *The depth of the implanted ions in the target material; (a) mass of an incoming ion is less than the mass of the target material, (b) mass of the incoming ion is greater than the mass of the target material.* R_p It *depends on ion mass and incident energy, while* $\frac{\Delta R_p}{R_p}$ *depends on the ratio of incident mass and target mass [3.7].*

3.5 SRIM simulation code

SRIM with TRIM (transport of ions in the matter) option is a well-known computer software for calculating the interaction of atoms in a material [3.15]. TRIM is of crucial importance for this software package, and it is based on a numerical method called Monte Carlo simulation. TRIM is used to perform calculations of each ion interaction with matter. There is a compound dictionary; valuable materials are saved containing empirical data on their composition. This software also enables the user to simulate the desired compound by entering appropriate parameters such as atomic number, atomic

mass, and stoichiometry of participating atoms. In this investigation, SRIM was used to simulate the desired energies before actual implantation in order to enable the implanted ions to reach the desired depth near the material's surface, as shown in **Figure 3.9**.

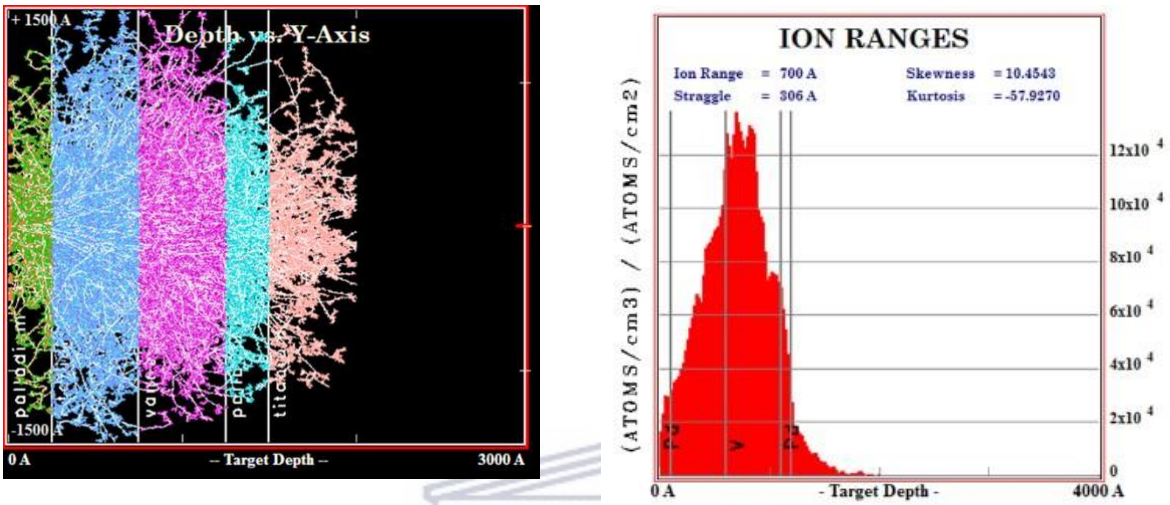

Figure 3.9: *Typical SRIM simulation showing (a) ion distribution and (b) ion ranges implanted at keV energy range.*

3.5.1 Implantation of samples

In this investigation, ion implantation of the samples was achieved using a 200-20A2F ion implanter, shown in **Figure 3.10** available, at iThemba LABS, Tandem and Accelerator Mass Spectrometry department, South Africa. Prior to implantation, samples were characterized for thickness confirmation using Rutherford backscattering spectrometry (RBS) technique discussed in the next chapter (chapter 4) and it was found that two out of five samples deposited had a different thickness of the second Pd layer (layer 4) with this layer having a thickness of ~17 nm. Therefore, these two samples were implanted with Fe ions at 150 keV to higher fluences of 1×10^{15} and 1×10^{16} *ions/cm²* respectively while the other three samples were implanted with Fe ions at 150 keV to fluences of 1×10^{12}, 1×10^{13}, *and* 1×10^{14} *ions/cm²* respectively, see **table 3.1**. The choice

of Fe as an implantation species is supported by its affinity to hydrogen and the possibility of forming $FeTiH_2$ hydride.

Table 3.1: *samples with implantation energy and fluences*.

samples	**Implantation energy (keV)**	**Fluence (*ions/cm*^{2})**
Pd (25 nm)/Ti (50 nm)/V (50 nm)/Pd (25 nm)	150	1×10^{12}
Pd (25 nm)/Ti (50nm)/V (50 nm)/Pd (25nm)	150	1×10^{13}
Pd (25 nm)/Ti (50nm)/V (50 nm)/Pd (25nm)	150	1×10^{14}
Pd (25 nm)/Ti (50nm)/V (17 nm)/Pd (25 nm)	150	1×10^{15}
Pd (25 nm)/Ti (50 nm)/V (50 nm)/Pd (17 nm)	150	1×10^{16}

Varian-200-20A2F

Figure 3.10: *Varian-200-20A2F ion implanter.*

3.6 Hydrogenation process

The samples under investigation were hydrogenated using a CVD (Chemical Vapour Deposition) system at the University of the Western Cape, Physics and Astronomy department using pure hydrogen gas (H_2). The hydrogenation of the samples was carried out at a threshold temperature of 550 ℃ with a flow rate of 100 SCCM. The following steps describe how the hydrogenation experiment was carried out.

i. Firstly, the samples were mounted on the sample holder and inserted into a chamber with a vacuum pressure of 10^{-7} mbar.

ii. The temperature was ramped up to 550 ℃ while flowing hydrogen gas at a flow rate of 100 SCCM while keeping the pressure constant at 100 µbar.

iii. The samples were hydrogenated at 550 ^{o}C for 30 minutes.

iv. The CVD system was switched off for the samples to cool down to room temperature at the rate of 5 ℃/min in the presence of hydrogen.

v. Finally, the samples were taken out of the furnace and to avoid diffusing hydrogen out of samples, they were immediately kept in liquid nitrogen.

3.7 References

[3.1] Jilani, A., Abdel-wahab, M. S., & Hammad, A. H. (2017). Advance Deposition Techniques for Thin Film and Coating. *Modern Technologies for Creating the Thin-Film Systems and Coatings*.

[3.2] Hu, Z. G., Tan, Z. Y., Lin, Z., Chen, J., Wang, B. S., Tian, L. F., Zheng, R. T., Chen, Y. C., Cheng, G. A.. Cu ion implantation improves the performance of Si film anode used in lithium-ion battery. *Nuclear Instruments and Methods in Physics Research, Section B: Beam Interactions with Materials and Atoms*, *440* (2018), 191–196.

[3.3] Mazzoldi, P., Mattei, G. (2005). Potentialities of ion implantation for the synthesis and modification of metal nanoclusters. *Rivista Del Nuovo Cimento*, *28* (7), 1–69.

[3.4] Williams, J. S. (1986). Materials modification with ion beams. *Reports on Progress in Physics*, *49*(5), 491–587.

[3.5] Machaka, R. (2006). *Ion Beam Modification of Boron Nitride by Ion Implantation*.PhD thesis, University of the Witwatersrand, Johannesburg, South Africa.

[3.6] Rautray, T. R., Narayanan, R., & Kim, K. H. (2011). Ion implantation of titanium-based biomaterials. *Progress in Materials Science*, *56*(8), 1137–1177.

[3.7] Nastasi, M., Mayer, J. M., and Hirvonen, J. K. (1996). *Ion Solid-Interaction:Fundamentals and Applications*. Cambridge Solid State Science Series, Cambridge University Press.

[3.8] Townsend, P. D., & Nunn, P. J. T. (2005). Optical effects of ion implantation. *Engineering Thin Films and Nanostructures with Ion Beams*, *501*, 229–278.

[3.9] Amolo, G. (2008). Optical and electrical properties of ion beam modified materials. PhD thesis, University of the Witwatersrand, Johannesburg, South Africa.

[3.10] Aradi, E. (2014). Investigations on the characterazation of ion implanted hexagonal boron nitrate. PhD thesis, University of the Witwatersrand, Johannesburg, South Africa.

[3.11] Cheung, N., & Berkeley, U. C. (n.d.). Advantages of Ion Implantation • Precise control of dose and depth profile. *1–26.*

[3.12] Fink, D., & Chadderton, L. T. (2005). Ion-Solid Interaction: Status and Perspectives. *35(3).*

[3.13] Orloff, J., Utlaut, M., Swanson, L., Orloff, J., Utlaut, M., & Swanson, L. (2003). Interactions of Ions with Solids. *High Resolution Focused Ion Beams: FIB and Its Applications*, 123–145. [3.14] Gibbons, J. F. (1968). Ion Implantation in Semiconductors—Part I Range Distribution Theory and Experiments. *Proceedings of the IEEE*, *56*(3), 295–319.

[3.15] Konobeyev, A. Y., Fischer, U., Korovin, Y. A., & Simakov, S. P. (2017). *Evaluation of effective threshold displacement energies and other data required for the calculation of advanced atomic displacement*. *3*, 169–175.

[3.16] Jilani, A., Abdel-wahab, M. S., & Hammad, A. H. (2017). Advance Deposition Techniques for Thin Film and Coating. *Modern Technologies for Creating the Thin-Film Systems and Coatings*.

[3.17] Mogogodi, S. (2019). Hydrogen storage capacity of the Ti-Pd multilayer.

[3.18] Pollock, T. J. (1987). A Study of Ion Implanted Silicon Using Rutherford Backscattering Spectroscopy with Ion Channeling.

[3.19] Gemmell, D. S. (1974). Channelling and related effects in the motion of charged particles through crystals. *Reviews of Modern Physics*, *46*(1), 129–22.

Chapter 4

Characterization techniques

This chapter entails the description of the characterization techniques that were used in this investigation. These techniques include Rutherford backscattering spectrometry (RBS), Elastic recoil detection analysis (ERDA), scanning electron microscope (SEM), and X-ray diffraction (XRD).

4.1 Rutherford backscattering spectrometry (RBS)

4.1.1 Introduction

RBS is one of the analytical methods used primarily in material science for film thickness determination, elemental composition, and depth profiling of individual elements [4.1]. It is a non-destructive technique; sensitive to heavy elements of the order of parts-per-million (ppm) in a low Z matrix and has a depth resolution of several nm [4.1]. Standard RBS uses He-ions with energy in the MeV regime [4.2]. The possible depth to be analysed is ~3 μm depending on incident ions energy [4.1]. It involves the ions accelerated towards the target and traversed through, losing energy along their path and are backscattered from a target atom nucleus. Several physics concepts that describe the interaction during the RBS measurement give information regarding the samples under analysis. As discussed in subsequent sections, these include kinematic factor, K, scattering cross-section, and stopping cross-section due to energy loss dE.

dx

4.1.2 **Kinematic factor (K)**

When a stationary target of mass M_2 is bombarded with a particle of mass M_1 with energy E_0 moving with constant velocity, they will elastically collide, and the energy will be transferred from the moving to the stationary particle. (Figure 3.6 in the previous section 3.4) shows the schematic diagram of the scattering process, where the scattering angle is and φ is the recoil angle. The energy relationship between the target material and incident particle can be determined by applying energy conservation principles and conservation of momentum [4.3]. The relationship between energy E of the projectile M_1 after the scattering by surface atoms and initial energy before the scattering is described by the kinematic factor K, given by:

$$E = KE_0 \tag{4.1}$$

Where.

$$K = \left[\frac{M_1\cos(\theta)+\left(M_2{}^2-M_1{}^2\theta\right)^{\frac{1}{2}}}{M_1+M_2}\right]^2 \tag{4.2}$$

The kinematic factor K depends on ion and target masses M_1 and M_2, respectively, and the scattering angle(θ), hence it can be calculated for different target and projectile masses and scattering angles. It indicates atoms that constitute film/material under investigation.

4.1.3 **Rutherford scattering cross-section**

Scattering cross-section indicates the number of atoms present with a probed depth in film/material under investigation. The probability of the ions being scattered is described by differential scattering cross-section:

$$\frac{d\sigma}{d\Omega} = \left(\frac{Z_1 Z_2 e^2}{4E}\right)^2 \frac{4}{sin^4(\theta)} \frac{\left\{\left[1-\left(\left(\frac{M_1}{M_2}\right)\sin(\theta)\right)^2+\cos(\theta)\right]\right\}^2}{\left[1-\left((M_1-M_2)\sin(\theta)\right)^2\right]^{\frac{1}{2}}} \tag{4.3}$$

Where E is the energy of the projectile before scattering, $Z_1$and Z_2 are atomic numbers of projectile and target respectively, θ is the scattering angle, e is the electric charge, and Ω is the solid angle as shown in **Figure 4.1**. [4.4]

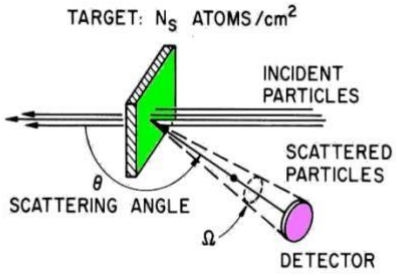

Figure 4.1: *Schematic diagram of the scattering process [4.5].*

The number of counts Y registered by the detector is given by:

$$Y = QNt\frac{d\sigma}{d\Omega}\Omega \tag{4.4}$$

Where Q is the number of projectiles striking the target, N is the volume density of the target atoms, t is the thickness of the target, and $\frac{d\sigma}{d\Omega}$ is the average scattering cross-section for scattering into a solid angle Ω at scattering angle. For small values of Ω, the average $< \frac{d\sigma}{d\Omega} >$ can be approximated by differential scattering cross-section $\frac{d\sigma}{d\Omega}$ and is usually referred to as scattering cross-section and is given by σ. Therefore, the yield can be expressed as:

$$Y = NQt\sigma\Omega \tag{4.5}$$

4.1.4 **Stopping cross-section**

Stopping cross-section indicates the depth at which atoms are located/detected in film/material under investigation, translating into thickness. As the incident projectile traverses through a target, they experience energy loss $\frac{dE}{dx}$ (the energy at distance x) due to collisions with target electrons.

The electronic energy loss at distance x travelled is given by Beth-Bloch formula:

$$\frac{dE}{dx} = NZ_2 \left[\frac{4(Z_1 e^2)^2}{m_e v_1}\right] ln\left(\frac{2m_e {v_1}^2}{KZ_2}\right) \quad (4.6)$$

Where NZ_2 the areal electronic density of the target, M_e is the electron mass, V_1 is the projectile's velocity, and $\boldsymbol{K}$ is Bloch's constant considered to be 10 eV. Energy loss is proportional to the square of the atomic projectile mass [4.4].

4.1.5 **Energy straggling**

As the energetic ions penetrate the target, they encounter energy loss due to the various individual interactions. The active ions with the initial velocity, will not have the same energy after travelling the same distance after penetrating through the thickness target Δx, leading to statistical energy fluctuations [4.3]. Since ions lose energy due to their interaction with target electrons, electronic interactions contribute dominantly to the energy straggling [4.3]. According to Bohr's theory, energy straggling is not dependent on the energy of the incident ions. The root mean square (rms) of the energy variation increases with the square root of the electron density per unit area NZ_2t in the target. For a layer thickness t, Bohr's energy straggling has a variance:

$${\Omega_B}^2 = 4\pi(Z_1 e^2)^2 NZ_2 t \quad (4.7)$$

Where Z_1 and Z_2 are projectile and target atomic numbers, N is the volume density of the target, e is the electronic charge, and t is the thickness of the target. Ω_B^2 Increases with Z_2. The standard deviation Ω_B of Bohr's theory is the most appropriate value to use, estimating energy straggling in solids with the 1 to 2 MeV range.

4.1.6 Experimental set-up

In this investigation, target samples were mounted on sample holders and place inside the vacuum chamber of 10^{-6} mbar pressure and were tilted by the magnitude of -5^{o} to manage the channelling ions. Si (Li) detector was placed at a scattering angle of 150^{o} from the direction of the incident beam that collected the scattered ions. Target samples were bombarded with a 1 mm diameter collimated beam of 2 MeV He^{++} particles. The total charge and current of 20 µC were collected at a beam current of 50 nA. The schematic set-up of RBS is illustrated in **Figure 4.2** below.

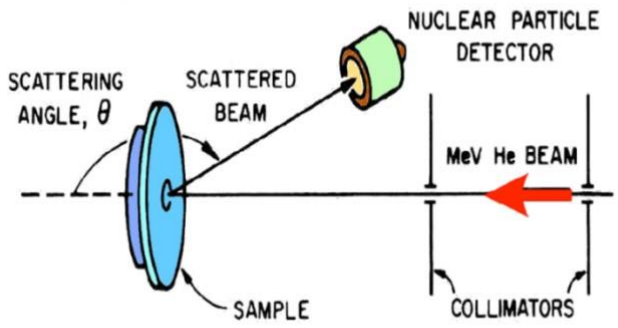

Figure 4.2: *Experimental set-up of RBS [4.5]*.

4.1.7 **Energy calibration**

Si-Co-Au calibration sample was used to determine channel number/energy calibration in terms of backscattered energy of particles. This was achieved using a gold-cobalt on top of silicon dioxide deposited on a silicon substrate ($AuCo/SiO_2/Si$) standard sample. An average current of 60 nA and a total charge of 20 µC were used for all samples. The vacuum pressure during the measurements was better than 10^{-6} mbar. The energy of the scattered He^{++} ions was recorded using a Si surface barrier detector with the energy resolution of ~23 keV positioned at a backscattering angle of 150^o and the sample surface tilted by 5^o towards the detector. Simulations of RBS spectra were achieved using SIMNRA software version 6.06 *[www.simnra.com]* with SigmaCalc option selected for the non-Rutherford cross-section in the simulation process as shown in **Figure 4.3** below.

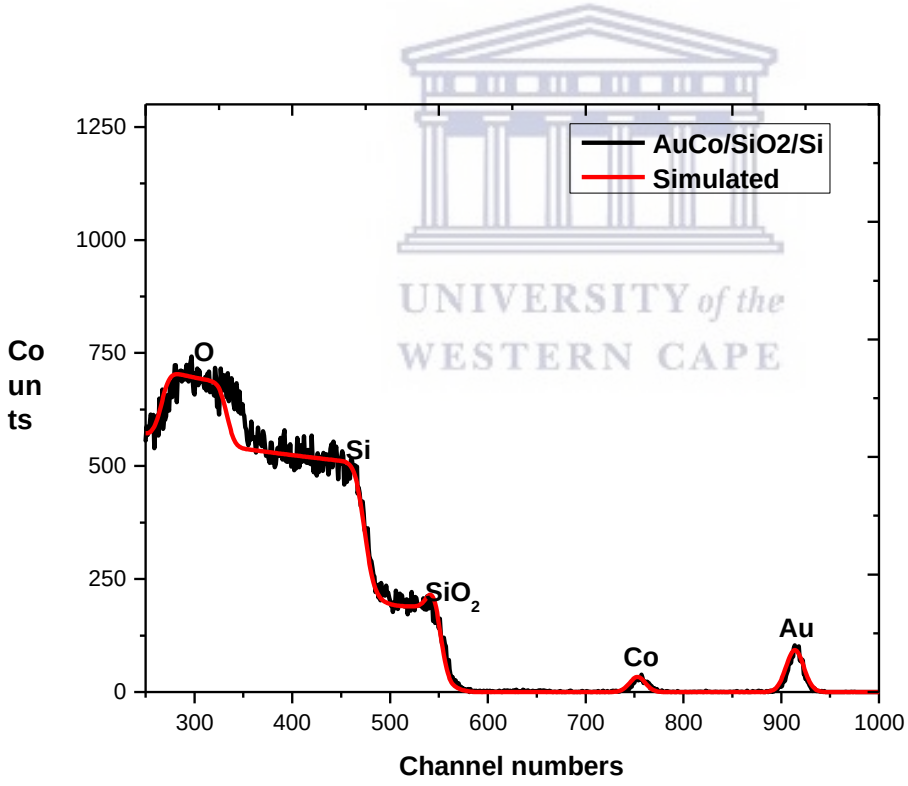

Figure 4.3: *AuCo/SiO2/Si simulated standard sample.*

4.2 Elastic recoil detection analysis (ERDA)

ERDA is one of the analytical techniques for quantitative analysis of light elements [25]. ERDA has a detection limit of ≥0.01 at. % and has a typical depth resolution of 30 – 60 nm due to hydrogen's relatively small energy loss of in solids [4.6]. ERDA was employed in this study for the determination of hydrogen concentration and depth profiling.

4.2.1 Fundamentals of (ERDA) technique

4.2.1.1 Kinematic factor

As explained in RBS, when the target to be examined is irradiated with energetic ions, ions get scattered at an angle θ. During this interaction between the incident ions and the target atoms, the energy is transferred to the atoms of the target and recoiled in a forward direction through an angle φ, as illustrated by **Figure 4.5**. This interaction is governed by the Coulomb repulsion force [4.7, 4.8]. Since He-ions are used in ERDA, and it is more massive than hydrogen, hydrogen is knocked out in the forward direction with significant energy after being struck by He-ions. The energy E_2 after recoil transferred by incident ions of mass M_1 and E_0 to the target atoms of mass M_2 recoiled at angle φ is given by:

$$E_2 = \frac{4M_1M_2}{(M_1+M_2)^2} E_0 \cos(\varphi)^2 \quad (4.8)$$

The energy fraction transferred between incident and recoil particles is given by the kinematic factor for recoiling as:

$$K_r = \frac{4M_1M_2}{(M_1+M_2)^2} \cos(\varphi)^2 \quad (4.9)$$

Where φ is the recoil angle, and M_1 and M_2 are masses of incident and recoil particles, respectively. the expressions of K_r depends on the mass ratio $\frac{M_2}{M_1}$ and angle φ.

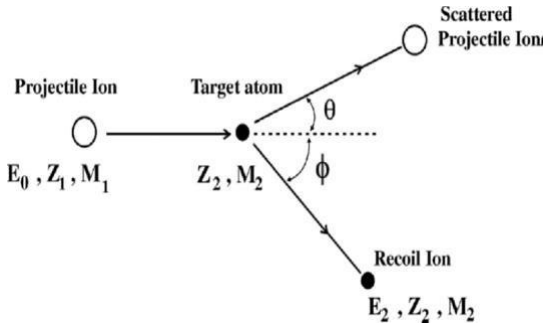

Figure 4.4: *Schematic representation of binary interaction between an incident ion of M_1 and the target of mass M_2 [4.7].*

4.2.1.2 **Scattering cross-section and depth resolution in ERDA**

The probability of one incident ion from the beam to knock an atom out of a target is referred to as scattering cross-section [4.7]; this is given as:

$$\frac{d\sigma}{d\Omega} = \left(\frac{Z_1 Z_2}{2E_0}\right)^2 \frac{\left(1+\frac{M_1}{M_2}\right)^2}{\cos(\varphi)^3} \tag{4.10}$$

Schematic representation of emission of recoil atoms in the scattering process [4.7]. Where E_0 is the starting energy of the incident projectile, $Z_1$and Z_2 are atomic numbers of the incident projectile and target, respectively. Scattering cross-section as a function of $\frac{1}{{E_0}^2}$ shows that the yield of the recoils and sensitivity of the ERDA decreases with the depth due to reducing the energy of the incident projectile E_0. Considering surface approximation and assuming uniform energy loss, then the depth resolution δ_x can be expressed as:

$$\delta_x = \frac{\delta E_2}{E_2}(S_{rel})^{-1} \tag{4.11}$$

Where S_{rel} is relative energy loss factor expressed as:

$$S_{rel} = \frac{\frac{dE_0}{dx}}{E_0}\frac{1}{\sin(\alpha)} + \frac{\frac{dE_2}{dx}}{E_2}\frac{1}{\sin(\beta)} \quad (4.12)$$

Where α and β are the incident angle of the beam and the exit angle of recoiling ion, respectively, as illustrated by figure 4.6, the depth resolution depends on the relative energy resolution and the relative stopping force of incoming and outgoing ions [4.7].

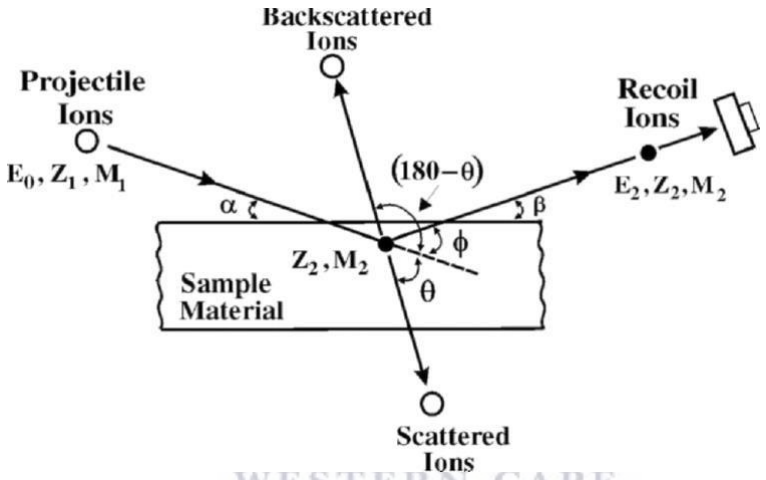

Figure 4.5: *Schematic diagram of ERDA geometry [4.7].*

4.2.1.3 **Experimental set up**

The depth profile and concentration of hydrogen of the as-deposited and hydrogenated samples were measured by ERDA using 3 MeV He^{++} ions emanating from 3 MV Tandetron accelerator based at iThemba Laboratories accelerator-based Sciences (iThemba LABS). The energy resolution of ERDA depends on the detector's resolution. Still, it is affected by the energy straggling in the He^{++} stopping foil, resulting in a value of about 20 keV with a concentration detection limit of 0.1 at. % [4.9]. The samples were individually mounted on a ladder and then loaded into the sample chamber evacuated to a vacuum pressure better than 10^{-6} mbar.

4.2.1.4 **Energy calibration in ERDA.**

For channel number/energy calibration, the 15 μm thick Kapton standard coated with a 1 nm platinum to avoid charging effects was used. Three spectra were collected using He^{++} beam energies of 2, 2.5 and 3 MeV. After that, the samples were measured using beam energy of 3 MeV; an average current of ~ 60 nA and a total collected charge of 40 μC were maintained for all the samples. The energy spectra of recoiled hydrogen atoms were recorded using a Si surface barrier detector with an energy resolution of ~20 keV positioned at a recoiled angle of 30°. From the simulated ERDA spectra, the average hydrogen concentration and depth profile within the samples were calculated using equation 4.13 below.

$$\sum_{I=1}^{n} \frac{H_i t_i}{T_i} \tag{4.13}$$

Where t_i is the thickness at the specific layer in monolayers ($1 \times 10^{15}\ atoms/cm^2$), i represent the order number of layers in the sample, H is the hydrogen concentration at specific at. % and T is the total thickness. In this investigation, the simulation and analysis of ERDA spectra were done using SIMNRA software version 6.06 [www.simnra.com] with the SigmaCalc option selected for the non-Rutherford cross-section in the simulation process.

4.3 Scanning electron microscopy (SEM)

4.3.1 Introduction

SEM is one of the most fundamental techniques for the analysing of the microstructure morphology and chemical composition of the material [4.10, 4.11]. SEM produces images by irradiating the sample with a beam of electrons while scanning the surface [4.10, 4.12]. During the electron-sample interactions, various signals are detected with different detectors depending on the mode of SEM used. These signals contain information regarding the surface morphology and composition of the sample [4.10, 4.12- 4.13]. In this study, SEM was used to investigate the effect of ion implantation and hydrogen on the morphology for the Pd/Ti/V/Pd thin films stack on CP-Ti samples. In this investigation, SEM was done in the microscopic unit, at the department of physics and astronomy, University of the Western Cape using the Auriga Zeiss instrument coupled with the energy-dispersive spectrometry (EDS).

4.3.2 Configuration of scanning electron microscope

Typical SEM is an electronic and optical system that consists of major components such as an electron gun, a condenser lens, scanning coil, objective lens, sample holder, detector, and computer for image display [4.11, 4.13-4.14]. **Figure 4.6** shows the schematic SEM system.

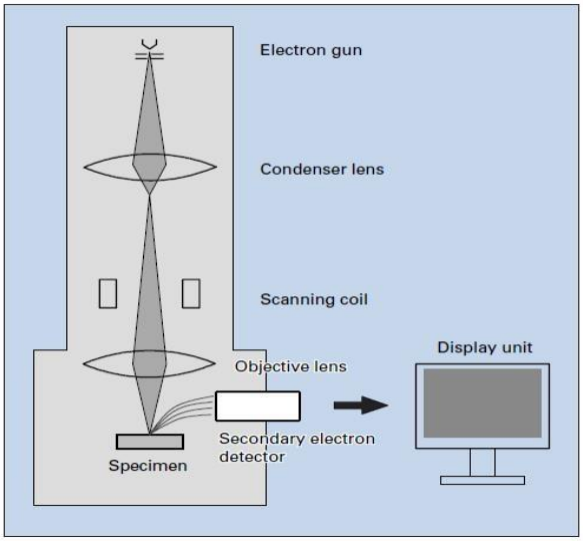

Figure 4.6: *The basic schematic diagram of SEM [4.14].*

Firstly, the electron gun, situated on top of the column, emits the electrons, and accelerates them to energy in a range of 0.1-30 keV. Due to the large diameter produced by a hairpin tungsten gun, the electron beam will diverge after passing through the anode from the emission source, thus affecting the image resolution. To avoid this process; a condenser lens is used to converge and collimate the electron beam into a parallel stream. The objective lens further focuses the electron beam into a probe point at the specimen surface. Lastly, the scanning coils deflect the focused electron beam to scan the surface, and the secondary electron detector collects emitted secondary electrons.

Secondary electrons (SE), backscattered electrons (BSE), characteristics x-rays, and Auger electrons are detected during interaction. **Figure 4.7** shows the detected signals with regions detected [4.11].

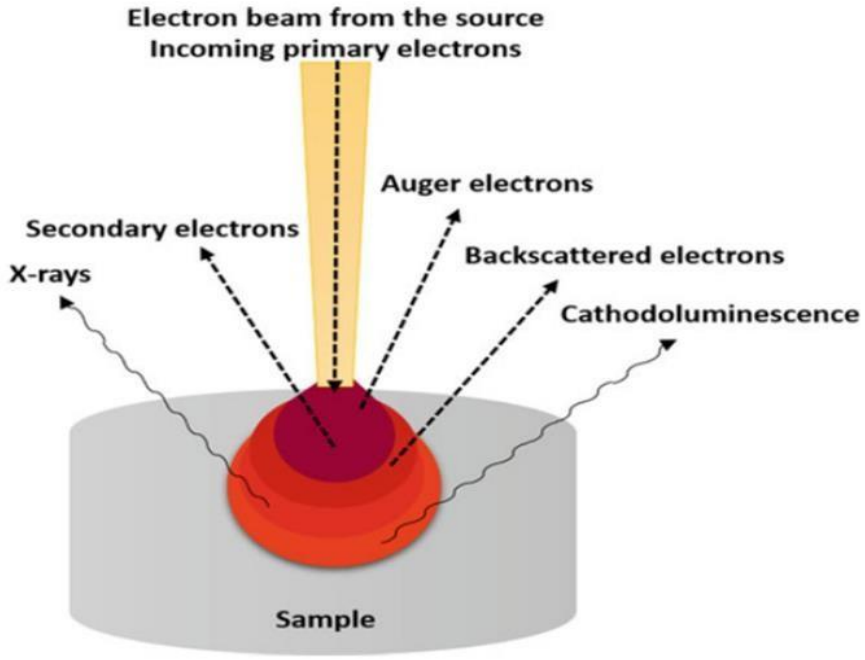

Figure 4.7: *Schematic representation of the interaction of the electron beam with the specimen and the signal emitted from the sample [4.13].*

Secondary electrons are used for topographic contrast in SEM (visualization of surface texture and roughness), and they can resolve surface structure down to the order of 10nm or better. Backscattered electrons are used to provide both compositional and topographic information of the sample. Auger electrons are emitted only closer to the surface due to their lower energies, and they have an escape depth of few nanometres, thus used primarily on the surface analysis [4.11].

4.3.3 **Energy-dispersive spectrometry (EDS)**

EDS is the most common system employed on SEM equipped with a silicon semiconductor detector, which is used to determination the elemental composition of the specimen [4.15, 4.16]. This technique uses characteristics x-rays to analyse the composition of the sample. The high energy beam of electron is focused onto the specimen for the generation of x-rays. At rest, an atom within the specimen contains electrons in their ground states in discrete energy levels or electron shells

bound to the nucleus [4.15]. When the electron beam impinges the specimen, it excites an electron in an inner shell, knocking it out from the shell and create a vacancy (electron-hole). An electron from the higher energy outer shell fills the hole. The x-rays are then released, resulting from the energy difference between both inner and outer shells. The emission of characteristic x-rays is demonstrated in **Figure 4.8** below. Emitted x-rays are of the respective elements that made up the specimen and are collected by a silicon detector. This x-ray allows the determination of the elemental composition of the specimen.

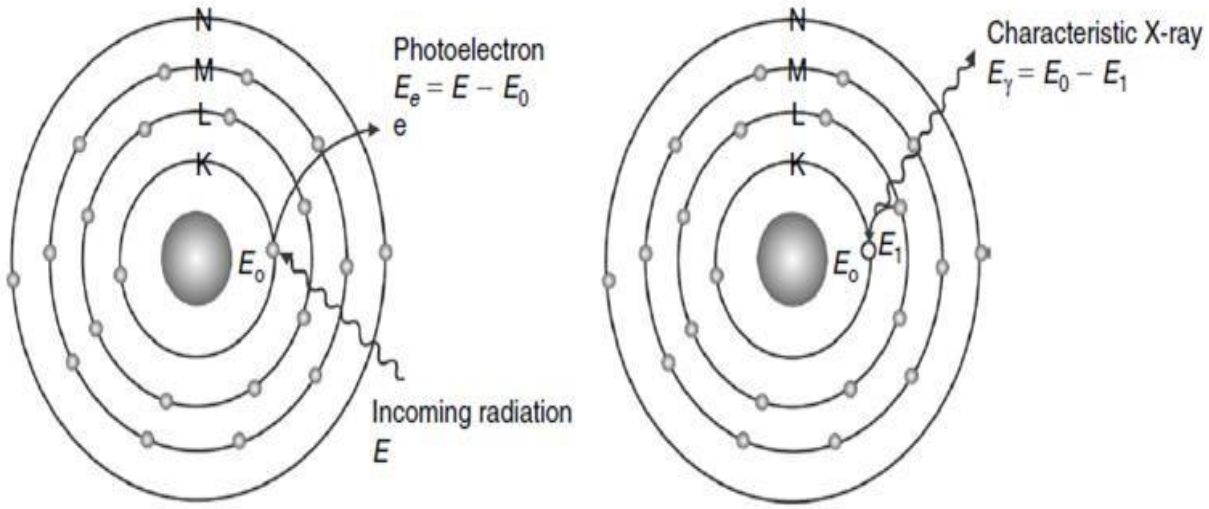

Figure 4.8: *The emission of characteristics x-rays by an atom of the specimen [4.17].*

4.4 X-ray diffraction analysis (XRD)

XRD is a powerful non-destructive method used to characterize of crystalline material [4.18]. This method reveals information regarding crystal structure, new phases, crystal orientation, and structural parameters. X-rays are a type of electromagnetic wave with a shorter wavelength ranging from 0.07-0.2 nm, distinguishing them from other electromagnetic waves such as radio waves, light, and gamma rays [4.19, 4.20]. In this investigation, x-ray diffraction was used to investigate the

formation of new phases and crystallinity of Pd/Ti/V/Pd stack on the CP-Ti substrate before and after implantation of heavy ions (150 keV Fe ions), as well as before and after hydrogenation.

4.4.1 Interaction between x-rays and target atoms

As x-rays traverse through the material, they get scattered by the electrons around the nucleus. They either scattered constructively or destructively. Only constructive scattered x-rays contain information regarding the target under investigation. For x-rays with initial intensity I_0, the total attenuation is related to material thickness and is described by the equation [4.21]:

$$-\frac{dI}{I_0} = \mu dx \tag{4.14}$$

Where μ is the linear absorption coefficient, which depends on the wavelength of the x-rays. By integrating equation 4.14, the intensity after transmission through-thickness x is given by:

$$I = I_0 e^{-\mu x} \tag{4.15}$$

Only signal that obeys Bragg's Law (equation 4.16), as shown in **Figure 4.9** are counted by the detector.

$$n\lambda = 2d\sin(\theta) \tag{4.16}$$

Where n is the order of reflection, λ is the wavelength, θ is the angle between the incident beams, and d is the distance between the lattice planes. Equation 4.16 is known as Bragg's law.

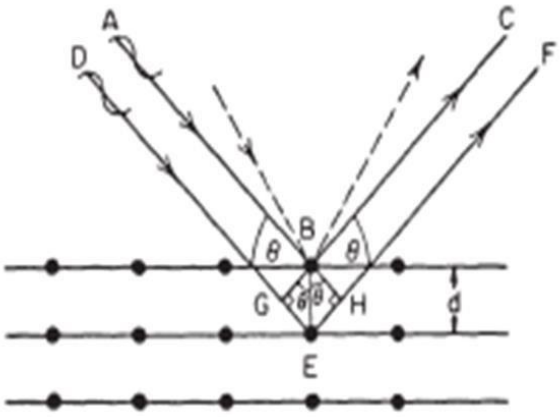

Figure 4.9: *The diffraction of x-rays by the crystal [4.21].*

4.4.2 **Geometry of crystals.**

The crystalline material is the material with atoms of the crystals being periodically arranged in space [4.22], such as a 3D periodical arrangement of points in space shown in **Figure 4.10**.

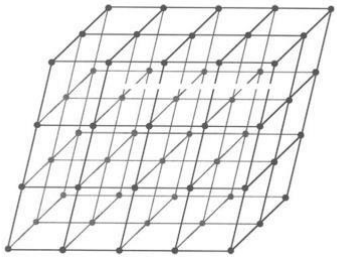

Figure 4.10: Schematic representation of Point lattice [4.22].

In figure 4.11, the lattice can be partitioned into small units/cubes when extended in 3D, forming the lattice point. These small cubes are called unit cells [4.22]. The unit cell is defined by the correlation between the lengths (a, b, c) of its sides and the inter-axial angles (α, β, γ) between them, as shown in **Figure 4.11**. The lengths are measured concerning the corner of the cell taken as the origin. These lengths and angles are called the lattice parameters.

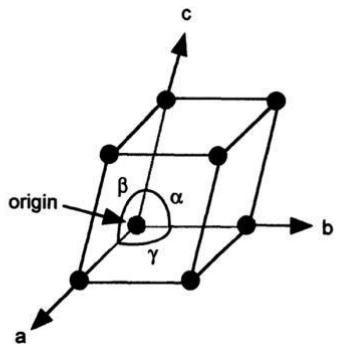

Figure 4.11: *Representation of a unit cell [4.22].*

There is a fundamental requirement of the unit cell. The built-up of the entire lattice by repeating the unit cell in 3D is one of the requirements of the unit cell. Seven shapes meet this requirement and are known as crystal systems. **Table 4.1** shows these seven crystal systems and 14 Bravais lattices.

Table 4.1: *Crystal systems and Bravais lattices [4.23]*

System	Axial lengths and angles	Bravais lattice	Lattice symbols
Cubic	Three equal axes at right angle, $a = b = c, \alpha = \beta = \gamma = 90°$	Simple Body-centred Face-centred	P I F
Tetragonal	Three equal axes and right angles, two equals, $a = b \neq c, \alpha = \beta = \gamma = 90°$	Simple Body-centred	P I
Orthorhombic	Three unequal axes at right angles, $a \neq b \neq c, \alpha = \beta = \gamma = 90°$	Simple Body-centred Base-centred Face centred	P I C F
Rhombohedral	Three equal axes at right angles, equally inclined, $a = b = c, \alpha = \beta = \gamma \neq 90°$	Simple	R
Hexagonal	Two equal coplanar axes at 120º, third axes at right angle $a = b \neq c, \alpha = \beta = 90°, \gamma = 120°$	Simple	R
Monoclinic	Three unequal axes, one pair not at right angles $a \neq b \neq c, \alpha = \gamma = 90° \neq \beta$	Sample Base-centred	P C
Triclinic	Three unequal axes, unequally inclined and none at right angles $a = b = c, \alpha \neq \beta \neq \gamma \neq 90°$	Sample	F

The XRD for the samples under investigation was performed at Material Research Department (MRD) at iThemba LABS Cape Town, South Africa. Bruker D8-advanced-8 diffractometer was used to perform the experiments with x-ray source CuK_{α} of the wavelength 1.54050 Å. The voltage and current of 40 kV and 40 mA respectively were used for this investigation. These experiments were conducted at room temperature with the scanning range of 0 to 90 ° in 2 thetas.

4.5 References

[4.1] Ager, F. J., Respaldiza, M. A., Botella, J., Soares, J. C., Da Silva, M. F., Benítez, J. J., & Odriozola, J. A. (1996). Rutherford backscattering spectrometry (RBS) characterization of oxide scale formed on (AISI-304) steel after surface deposition of lanthanum. *Acta Materialia*, *44*(2), 675–681.

[4.2] Nakajim, K. (2009). Monolayer analysis using higher resolution Rutherford bacscattering spectrometry. PhD thesis, Kyoto university.

[4.3] Jarjis, R. A. (1979). Rutherford backscattering. *Physics Bulletin*, *30*(7), 287–287.

[4.4] Perrière, J. (1987). Rutherford backscattering spectrometry. *Vacuum*, *37*(5–6), 429–432. [4.5] Machaka, R. (2006). *Ion Beam Modification of Boron Nitride by Ion Implantation*. PhD thesis, University of the Witwatersrand, Johannesburg, South Africa.

[4.6] Jain, I. P., Jain, A., & Jain, P. (2010). ERDA: Technique for Hydrogen Content and Depth Pro le in Thin Film Metal Hydride This document appeared in ERDA: Technique for Hydrogen Content and Depth Profile in Thin Film Metal Hydride. *Whec 2010*, *78*.

[4.7] Adams, F., & Barbante, C. (2015). Particle-Based Imaging Techniques. *Comprehensive Analytical Chemistry*, *69*, 315–337.

[4.8] Rbs, T., & Erd, T. (1978). 3 Elastic Recoil Detection 3.1.

[4.9] Arnold Bik, W. M., & Habraken, F. H. P. M. (1993). Elastic recoil detection. *Reports on Progress in Physics*, *56*(7), 859–902.

[4.10] Derry, T. E., Nshingabigwi, E. K., Levitt, M., Neethling, J., & Naidoo, S. R. (2009). Crosssection transmission electron microscopy of the ion implantation damage in annealed diamond. *Nuclear Instruments and Methods in Physics Research, Section B: Beam Interactions with Materials and Atoms*, *267*(16), 2705–2707.

[4.11] Omidi, M., Fatehinya, A., Farahani, M., Akbari, Z., Shahmoradi, S., Yazdian, F., Tahriri, M., Moharamzadeh, K., Tayebi, L., & Vashaee, D. (2017). Characterization of biomaterials. In *Biomaterials for Oral and Dental Tissue Engineering*.

[4.12] Zhou, W., Apkarian, R., Wang, Z. L., & Joy, D. (2007). Fundamentals of scanning electron microscopy (SEM). *Scanning Microscopy for Nanotechnology: Techniques and Applications*, 140.

[4.13] Raghavendra, P., & Pullaiah, T. (2018). Biomedical Imaging Role in Cellular and Molecular Diagnostics. *Advances in Cell and Molecular Diagnostics*, 85–111.

[4.14] Sharma, S. K., Verma, D. S., Khan, L. U., Kumar, S., & Khan, S. B. (2018). Handbook of Materials Characterization. In *Handbook of Materials Characterization* (Vol. 2, Issue February).

[4.15] Weiss, A. D. (1983). Scanning Electron Microscopes. Semiconductor International, 6(10), 90–94.

[4.16] Bashir, S., & Liu, J. (2015). Nanocharacterization. In *Advanced Nanomaterials and Their Applications in Renewable Energy*.

[4.17] Lewis, D. B. (1992). Transactions of the IMF The International Journal of Surface Engineering and Coatings Scanning Electron Microscopy and X-ray Microanalysis TUTORIAL NOTES Scanning Electron Microscopy and X-ray Microanalysis. *Trans. Lnst. Metal Finish*, *70*(4), 98.

[4.18] Kohli, R. (2012). Methods for Monitoring and Measuring Cleanliness of Surfaces. In *Developments in Surface Contamination and Cleaning: Detection, Characterization, and Analysis of Contaminants* (Vol. 4).

[4.19] Schlögl, R. (2020). X-ray diffraction. *Catalysis from A to Z*, *2*, 2.

[4.20] Waseda, Y., Matsubara, E., & Shinoda, K. (2011). X-Ray Diffraction Crystallography. In *XRay Diffraction Crystallography*.

[4.21] Hansson, M., Berg, G., & Isaksson, M. (2009). Determination of Iodine In Vivo and In Vitro by X-Ray Fluorescence Analysis: Methodology and Applications. In *Comprehensive Handbook of Iodine*.

[4.22] Noyan, I. C., & Cohen, J. B. (1987). Fundamental Concepts in X-ray Diffraction. Residual Stress, *75–116.*

[4.23] Suryanarayana, C., & Norton, M. G. (1998). *X-Ray Diffraction.*

[4.24] Mazwi, S. (2016*).* Hydrogen storage in Ti-based coatings and Ti6Al4V alloy. Unpublished master's thesis, University of the Western Cape, Cape Town, South Africa.

[4.25] Konobeyev, A. Y., Fischer, U., Korovin, Y. A., & Simakov, S. P. (2017). Evaluation of effective threshold displacement energies and other data required for the calculation of advanced atomic displacement. *3*, 169–175.

[4.26] Mogogodi, S. (2019). Hydrogen storage capacity of the Ti-Pd multilayer systems.

[4.27] Pollock, T. J. (1987). A Study of Ion Implanted Silicon Using Rutherford Backscattering Spectroscopy with Ion Channelling.

[4.28] Gemmell, D. S. (1974). Channelling and related effects in the motion of charged particles through crystals. *Reviews of Modern Physics*, *46*(1), 129–227.

Chapter 5

Results and discussion

5.1 Introduction

This chapter entails analyses of the results achieved in this investigation using relevant characterization techniques discussed in chapter four. The effect of ion implantation on all samples is discussed in section 5.2. In contrast, the results of the hydrogenation experiments of the same system under pure hydrogen gas (H_2) gas environment are discussed in section 5.3.

5.2 Effect of ion implantation

Metal treatment using ion implantation was reviewed in chapter two, with several researchers [5.15.2] reporting an improvement in surface modification due to ion implantation done at various energies and fluencies. In their investigations, new structural formation occurred due to the ion implantation process, attributed to the interaction between the atoms of the host material and the atoms of the implanted species. In this investigation, a system of CP-Ti coated with Pd (25 nm)/Ti (50 nm)/V (50 nm)/Pd (25 nm) and Pd (25 nm)/Ti (50 nm)/V (50 nm)/Pd (17 nm) multilayer thin films were implanted with Fe ions at 150 keV. Three samples of a system of CP-Ti coated with Pd (25 nm)/Ti (50 nm)/V (50 nm)/Pd (25 nm) were implanted to a fluence values of 1×10^{12} , 1×10^{13} , and $1 \times 10^{14}\ ions/cm^2$; while two samples of Pd (25 nm)/Ti (50 nm)/V (50 nm)/Pd (17 nm) were up to 1×10^{15} and $1 \times 10^{16}\ ions/cm^2$ at iThemba LABS using Variation-Extrion 200-20A2F model ion implanter with an ES-30/25C processing station. All samples were characterized before and after implantation using SEM, XRD, and RBS.

The surface morphological transformations were studied by scanning electron microscope (SEM), crystalline and phase transformations were studied by x-ray diffraction (XRD), and elemental composition and depth profile were investigated by Rutherford backscattering spectrometry (RBS).

5.2.1 Surface morphological analysis

Figure 5.1(a) shows the SEM micrographs of the as-deposited Pd (25 nm)/Ti (50 nm)/V (50 nm)/Pd (25 nm) multilayer thin films deposited on the CP-Ti, which is like that of the Pd (25 nm)/Ti (50 nm)/V (50 nm)/Pd (17 nm). In contrast, **Figure 5.1** (b-d) show the implanted samples of the same system of Pd (25 nm)/Ti (50 nm)/V (50 nm)/Pd (25 nm) with Fe ions at 150 keV at a fluence ranging from 1×10^{12} , 1×10^{13} , and 1×10^{14} $ions/cm^2$ respectively, while **Figure 5.1** (e-f) shows that of two samples of Pd (25 nm)/Ti (50 nm)/V (50 nm)/Pd (17 nm) implanted to up to 1×10^{15} and 1×10^{16} $ions/cm^2$. The as-deposited samples showed rough and non-uniform surfaces with interconnected crystals that resulted from the deposition process. The implanted samples displayed no visible effect of ion implantation (150 keV Fe ions) at low fluence (**Figure 5.1**(b-d)) except for samples implanted with a fluence of 1×10^{15} and 1×10^{16} *ions/cm*^{2}, which displayed slight changes as shown in **Figure 5.1** (e and f). The smoothness and the interconnected holes can be attributed to the surface morphological damage of the films due to the implantation resulting in lattice imperfection. This phenomenon has been reported to be responsible for improving hydrogen adsorption into the lattice of various materials [5.10-5.11]. Since SEM could not reveal any further information besides the surface morphological changes, XRD was the technique used to investigate the crystal structure of the samples. And the results are discussed in sub-section 5.2.2.

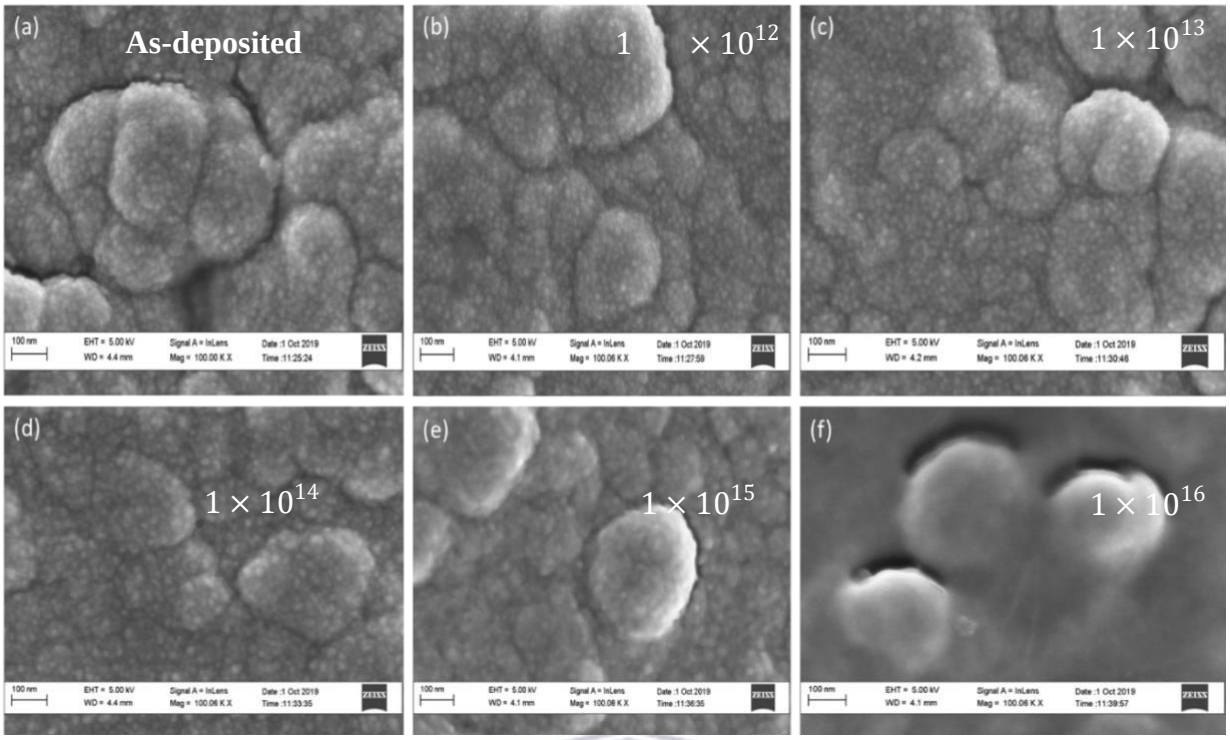

Figure 5.1: *SEM micrographs of (a) as-deposited sample, (b-d) Fe implanted at 150 keV at fluence of* 1×10^{12}, 1×10^{13}, *and* 1×10^{14} $ions/cm^2$ and (e-f) Fe *implanted at 150 keV at fluence of* 1×10^{15} *and* 1×10^{16} $ions/cm^2$.

5.2.2 Crystalline structure and phase transformation analysis

Figure 5.2(spectrum (a)) show the XRD spectra of the as-deposited Pd (25 nm)/Ti (50 nm)/V (50 nm)/Pd (25 nm) multilayer thin films deposited on the CP-Ti, which is like that of the Pd (25 nm)/Ti (50 nm)/V (50 nm)/Pd (17 nm). **Figure 5.2** (spectra b-d) show the implanted samples of the same system of Pd (25 nm)/Ti (50 nm)/V (50 nm)/Pd (25 nm) with Fe ions at 150 keV at a fluence ranging from of 1×10^{12}, 1×10^{13}, and 1×10^{14} $ions/cm^2$ respectively, while **Figure 5.2** (spectra e-f) figures show that of two samples of Pd (25 nm)/Ti (50 nm)/V (50 nm)/Pd (17 nm) implanted up to 1×10^{15} and 1×10^{16} $ions/cm^2$. All XRD patterns, as-deposited and Fe implanted samples, showed diffraction peaks corresponding to the hexagonal α-Ti phase with the

pattern no (00-044-1294) at an angles of **35º, 38º, 40º, 53º, 62.9º, 70.6º, 74º, 76º, 77º, 82º, 86.7º** respectively, with lattice parameters a =2.95 Å and c =4.68 Å. Additional diffraction peaks corresponding to Pd (pattern no.: 00-046-1043) and space group *Fm3m (225)* with lattice parameter a = 3.89 Å were also observed at an angles of **40º, 46.7º, 68º, 82º, 86.7º** respectively.

The Fe implanted samples showed no indication of intermixing of the films after implantation; hence, no new phases, but displayed the slight increase in peaks intensities with the increased fluence. Furthermore, the slight increase in peaks intensities was observed, and this change could be attributed to ion-induced strain. The V film was not observed, which could be attributed to the fact that it was in an amorphous phase after reacting with oxygen residue in the deposition chamber. To investigate the thickness profile, the elemental composition of the films and depth profile RBS techniques was used. **Table 5.1** summarizes the crystallographic information on the phases observed in this XRD investigation.

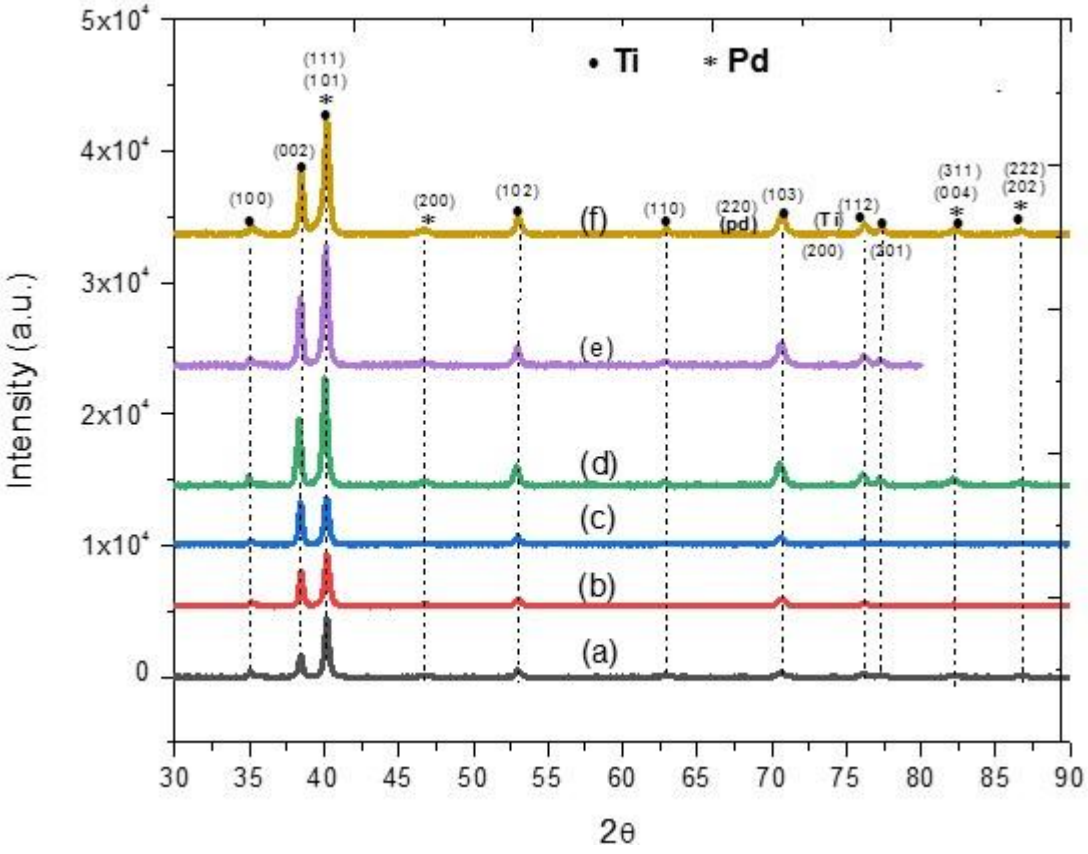

Figure 5.2: *XRD patterns of (spectrum (a)) as-deposited and (spectra (b-f)) Fe implanted at 150 keV at fluence ranging from* 1×10^{12} *to* 1×10^{16} *ions/cm*^{2} *respectively.*

Table 5.1: *Crystallographic information of different observed phases.*

Phase	Pattern no.	Space group	Lattice parameters
HCP (α-Ti)	00-044-1294	*P63/mmc (194)*	a = 2.95 Å; c = 4.68 Å
FCC (Pd)	00-046-1043	*Fm3m (225)*	a = 3.89 Å

5.2.3 RBS analysis

The elemental composition, stoichiometry, and the analysis of the thickness **for Pd (25 nm)/Ti (50 nm)/V (50 nm)/Pd (25 nm)** and **Pd (25 nm)/Ti (50 nm)/V (50 nm)/Pd (17 nm)** multilayer thin films deposited on the CP-Ti and the Fe implanted of the same system were determined using the RBS technique. The SIMNRA software version 6.06. *[www.simnra.com]* with the SigmaCalc option selected for Rutherford and non-Rutherford cross-section in the simulation, the process was used to fit the simulation over experimental data and give information regarding the stoichiometry and areal concentration.

For this study, 4.7 µm is the limited probe depth, and it was obtained using SRIM2013 software and 2 MeV He^{++} ions. **Figure 5.3 (a-c)** show the RBS spectra of the implanted samples of the system of Pd (25 nm)/Ti (50 nm)/V (50 nm)/Pd (25 nm) with Fe ions at 150 keV at a fluence ranging from of 1×10^{12}, 1×10^{13}, and 1×10^{14} $ions/cm^2$ plotted against the as-deposited spectra respectively.

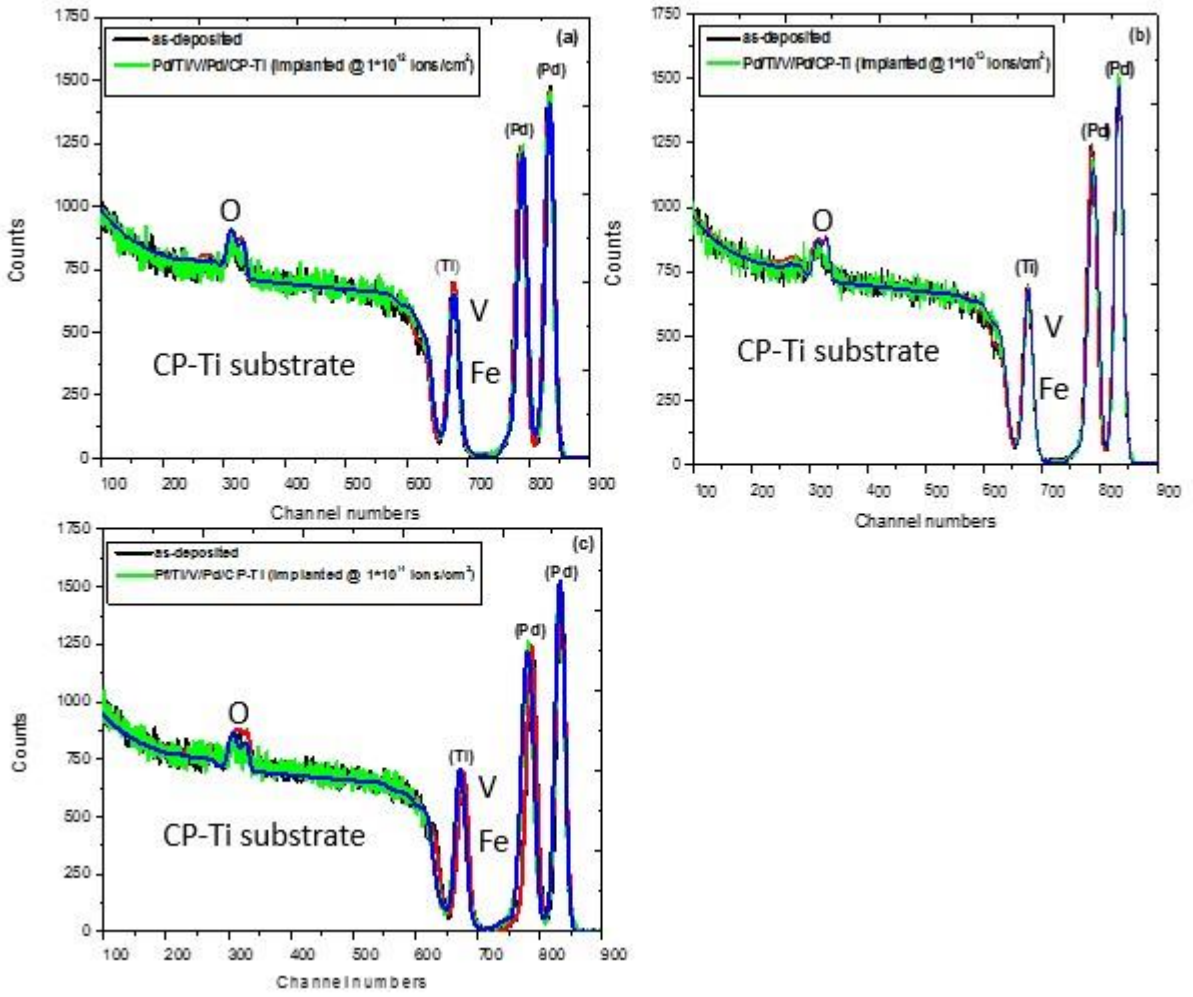

Figure 5.3: *RBS spectra of as deposited compared to the Fe implanted samples with energy of 150 keV, (a) at 1×10^{12} ions/cm^2, (b) 1×10^{13} ions/cm^2, and (c) 1×10^{14} ions/cm^2.*

Figure 5.4(a-b) show that of two samples of Pd (25 nm)/Ti (50 nm)/V (50 nm)/Pd (17 nm) implanted to up to 1×10^{15} and 1×10^{16} $ions/cm^2$. The discrepancy in the thickness of the Pd layer was attributed to the crystal monitor fault reading during the deposition. This discrepancy was taken into consideration during this investigation; hence these two samples are only compared to each other.

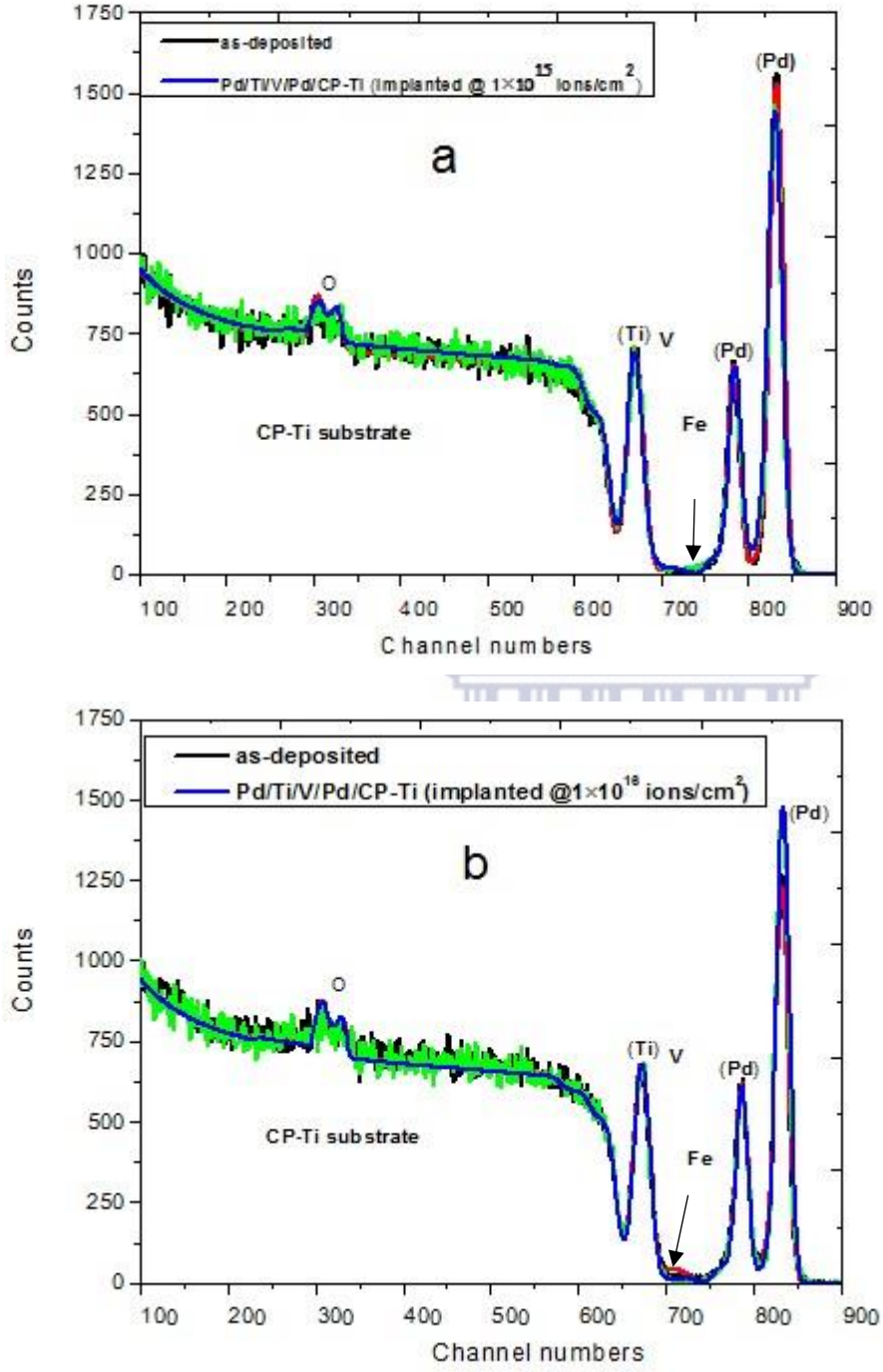

Figure 5.4: *RBS spectra of as deposited compared to the Fe implanted samples with energy of 150 keV, (a) 1×10^{15} ions/cm^2, and (b) 1×10^{16} ions/cm^2.*

The as-deposited and implanted samples display peaks corresponding to backscattered α-particles coming from Pd, V, and Ti films. Pd is displayed at channels 775 (second layer) and 845 (surface layer), respectively. At channel 675, the spectra show Ti from the film and V together in one peak due to similar kinematic factors emanating from their proximity in the periodic table. RBS technique at 2 MeV could not resolve them but could only be observed during the simulation process together with Fe implanted into the samples. The implanted samples showed stability with no indication of intermixing of layers, particularly the Pd layers, which are visibly seen in the spectra. In figure 5.3 (a-c), the simulated thicknesses of the as-deposited Pd surface layer and subsurface layer were found to be ~39.45 nm and ~40.10 nm, respectively, while that of spectra in figure 5.4 (d and e) were found to be ~17.81 nm and 18.56 nm. The Ti in the film was found to have reacted with Oxygen with 30 % O and 70 % Ti forming TiO_2 stoichiometry in all samples investigated. The thicknesses of Ti and V films were found to be 123.64 nm and 93.53 nm, respectively, considering the impact of oxygen atoms and implanted Fe ions in the system.

Comparing the simulated thickness and deposition thickness recorded by crystal monitor for Pd, Ti, and V films, there was a discrepancy attributed to the crystal monitor's accuracy. Therefore, analysis was based on the thicknesses obtained from RBS results rather than the crystal monitor of the deposition technique. All the implanted samples showed a notable change due to the implanted Fe species, with a slight shift in peaks to the small channel numbers, particularly the Pd interface layer and Ti at channels 775 and 675, respectively. This change supports the XRD results, as the peaks shifted to the lower angles. It was further observed that this change becomes more visible with an increased fluence. Hence, at the low fluence, the difference between the as deposited and implanted samples is not visible. The system showed no indication of intermixing of layers after implantation since all peaks are well separated, especially the Pd. Furthermore, it was observed that the simulated thicknesses of the implanted samples vary according the fluence.

5.3 Hydrogenation under pure H_2 gas

5.3.1 Introduction

In chapter two (literature review), investigations by several researchers and research groups on hydrogen storage materials and the conditions governing H absorption have been highlighted. Several researchers have reported the significance of threshold temperature of 550 ℃ for hydrogenation of Ti systems [5.1-5.4]. Mazowe et al. [5.5] studied the hydrogenation of Ti at a temperature ranging from 450 ℃ - 650 ℃, and high H content was found to be attained at a threshold temperature of 550 ℃. Magogodi et al. [5.12] also studied the hydrogenation of the TiPd system at 550 ℃ and found that at this temperature, high H content is absorbed into the bulk of the Ti-Pd system. Topic et al. [5.4] investigated the hydrogen storage in Ti-Al6-4V alloy where all samples were hydrogenated at the optimal temperature of 550 ℃ and reported good absorption of H into the bulk. In the other report, Lopez-Suarez et al. [5.1] have studied the implanted Ti system with H ions which was hydrogenated at a temperature range of 300 - 650 ℃ and reported high H content at 500 ℃.

Some researchers have suggested implantation to enhance H absorption since it can remove the oxide layer on the surface, hence accelerating the diffusion of H atoms into the bulk of the metal matrix [5.10]. This method can improve the surface activation kinetics of Ti systems [5.10] in addition to the metal treatment method using Pd metal catalyst film, which was reported by several researchers working on improving hydrogen absorption kinetics for Ti [5.4-5.9]. For instance, Zaluski et al. [5.8] investigated the effect of catalytic Pd on TiFe alloy for hydrogen absorption. They reported that Pd coated TiFe could absorb hydrogen at normal conditions without any activation before hydrogenation. In the other report, Topic et al. [5.4] investigated the hydrogen storage in Ti-Al6-4V alloy and reported that Ti-Al6-4V alloy capped with Pd catalytic layer

showed improvement in hydrogen absorption. In these investigations, the Pd catalyst layer supported the hydrogen absorption kinetics in titanium (Ti) by dissociating hydrogen molecules into atomic hydrogen and as a protective layer to avoid further oxidation on the Ti system. In this investigation, hydrogenation was conducted following these reports. All samples were hydrogenated at a temperature of 500 ℃ for 30 minutes under pure H_2 environment.

The crystalline and phase transformations were studied by x-ray diffraction (XRD). Rutherford backscattering spectrometry (RBS) studied elemental composition and elemental depth profile, and hydrogen profile was analysed using Elastic recoil detection analysis (ERDA). The results of all these measurements are presented and discussed in the sub-sections below.

5.3.2 Crystalline structure and phase transformation analysis

Figure 5.5 (spectrum (a)) show the XRD spectra of the as-deposited Pd (25 nm)/Ti (50 nm)/V (50 nm)/Pd (25 nm) multilayer thin films deposited on the CP-Ti, which is like that of the Pd (25 nm)/Ti (50 nm)/V (50 nm)/Pd (17 nm. Figures 5.5 (spectra b-d) show the implanted samples of the same system of Pd (25 nm)/Ti (50 nm)/V (50 nm)/Pd (25 nm) with Fe ions at 150 keV at a fluence ranging from of 1×10^{12} , 1×10^{13} , and $1 \times 10^{14}\ ions/cm^2$ respectively, while figure 5.5 (spectra e-f) figures show that of two samples of Pd (25 nm)/Ti (50 nm)/V (50 nm)/Pd (17 nm) implanted to up to 1×10^{15} and $1 \times 10^{16}\ ions/cm^2$.

In all figures, spectra displayed peaks corresponding to the hexagonal α-Ti phase (pattern no: 00044-1294) and space group *P63/mmc (194)* with lattice parameters a = 2.95 Å and c = 4.68 Å.

Additional diffraction peaks corresponding to Pd (pattern no.: 00-046-1043) and space group *Fm3m (225)* with lattice parameters a = 3.89 Å were also observed. There was no intermixing of films because of temperature in both systems. The face-centred tetragonal (FCC) TiH_2 (pattern no: 00-025-0982) and space group *Fm3m (225)* with lattice parameters a = 4.45 Å was challenging to

distinguish since their amount is low and overlapped with Ti peaks as indicated in all the figures, thus this could be attributed to the hydrogenation time which was less. Vanadium film was not observed as explained in the previous section. **Table 5.2** summarizes the crystallographic information on the phases observed in this XRD investigation.

Table 5.2: *Crystallographic information of different observed phases.*

Phase	**Pattern no.**	**Space group**	**Lattice parameters**
HCP (α-Ti)	00-044-1294	*P63/mmc (194)*	a = 2.95 Å; c = 4.68 Å
FCC (Pd)	00-046-1043	*Fm3m (225)*	a = 3.89 Å
FCC (TiH_2)	00-025-0982	*Fm3m (225)*	a = 4.45 Å

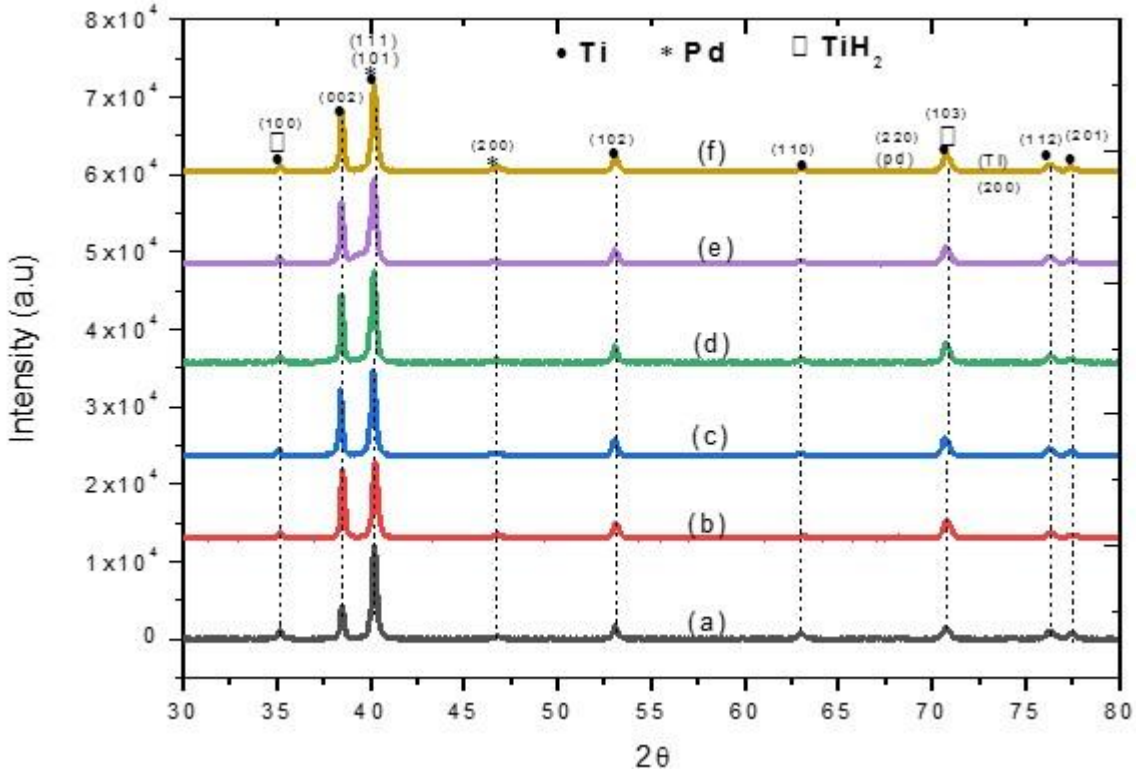

Figure 5.5: *XRD patterns of as-deposited compared to the Fe implanted samples with energy of 150 keV, (spectrum (a)) at 1×10^{12} ions/cm^2, (spectrum (b)) 1×10^{13} ions/cm^2, (spectrum (c))) 1×10^{14}*

ions/cm^2, (spectrum (d)) 1×10^{15} ions/cm^2, and (spectrum (f)) 1×10^{16} ions/cm^2.and hydrogenated at 550 º C for 30 minutes.

5.3.3 **RBS analysis**

Rutherford backscattering spectrometry (RBS) was used to investigate the thermal stability of the film stack before and after hydrogenation. The thermally stable structure of the film stack is the desired structure since hydrogenation is conducted at 550 º C, the region in which most thermodynamically unstable films react to form irreversible compounds. RBS probed depth in this investigation was calculated using SRIM2013 software. The simulation gave a penetration range of ~4.7 µm using 2 MeV He^{++} ions, which is beyond the ions penetration ranges of implanted ions used in this investigation. Therefore, RBS technique was very much suitable for probing the implanted samples.

Figure 5.6 (a-c) show RBS spectra (with an overlay of simulation) of samples implanted with 150 keV Fe ions to the fluence values of 1 × 10^{12}, 1 × 10^{13}, and 1 × 10^{14} *ions/cm^2* after hydrogenation, while **Figure 5.7 (a-b)** show RBS spectra (with an overlay of simulation) of samples implanted with 150 keV Fe ions to the fluence of 1 × 10^{15}, and 1 × 10^{16} *ions/cm^2*. There was no intermixing of layers in both samples; therefore, there was no need to plot the as implanted before hydrogenation. These indicated that there was no spontaneous reaction during deposition, and hydrogenation did not affect the integrity of the film stack. This observation agreed very well with the work of Magogodi et al. [5.12], where they reported a thermally stable film stack after hydrogenation at 550 º C for 30 minutes; because of the formation of the hydride phase, TiH_2. The TiH_2 appears to function as a diffusion barrier limiting the inter-diffusion of atoms of the film

stack. However, there was no intermixing of layers, noticeable shift of all peaks in all samples to higher channel numbers was observed, and this shift could be attributed to the ion-induced strain.

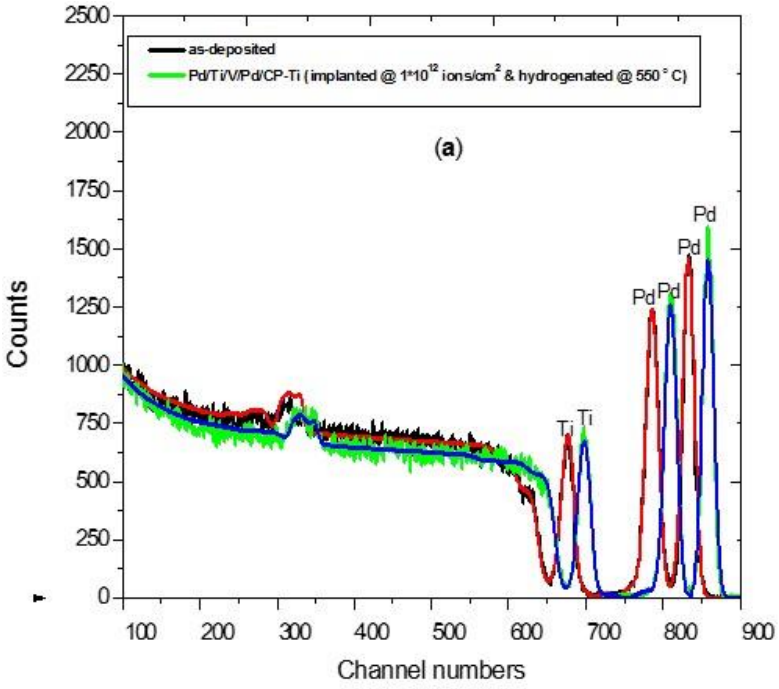

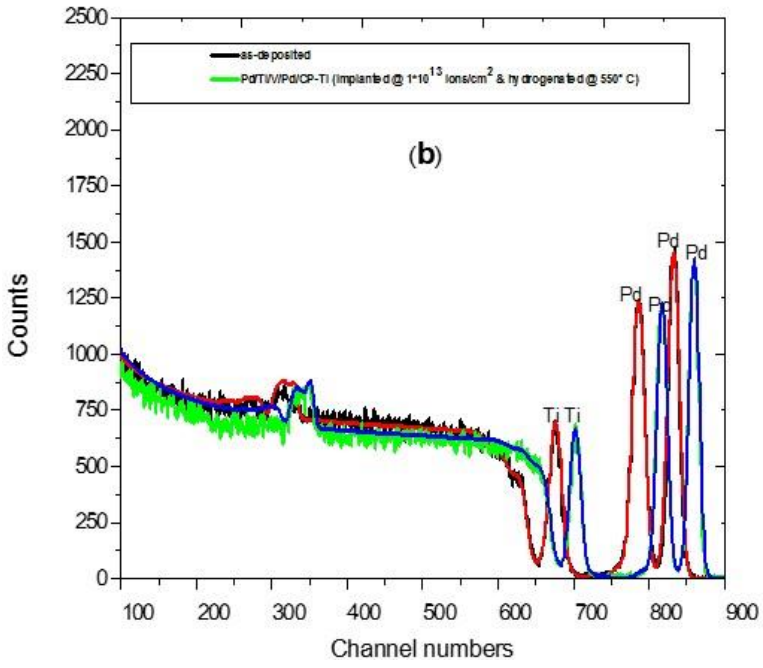

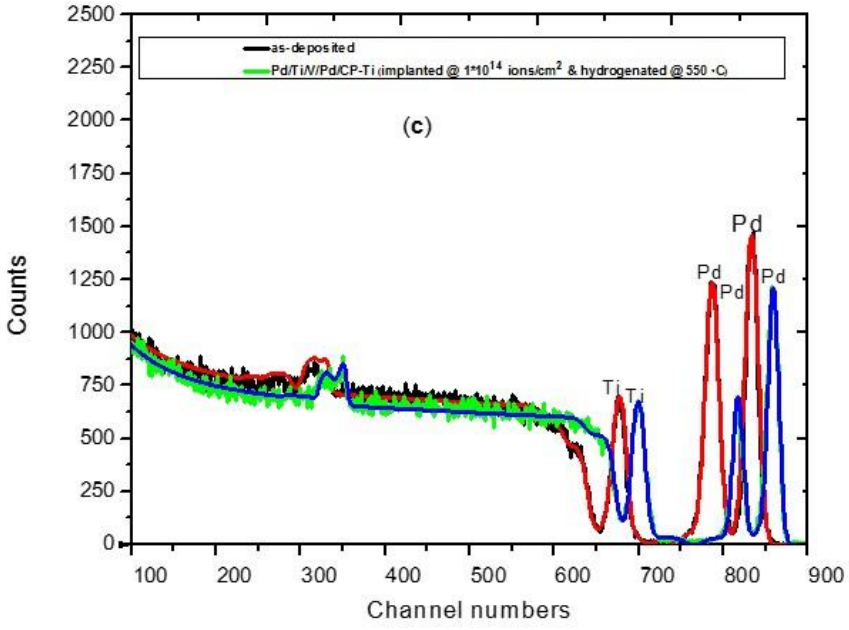

Figure 5.6: *RBS spectra of as deposited compared to the Fe implanted samples with energy of 150 keV, (a) at 1×10^{12} ions/cm^2, (b) 1×10^{13} ions/cm^2, and (c) 1×10^{14} ions/cm^2; hydrogenated at 550 º C for 30 minutes.*

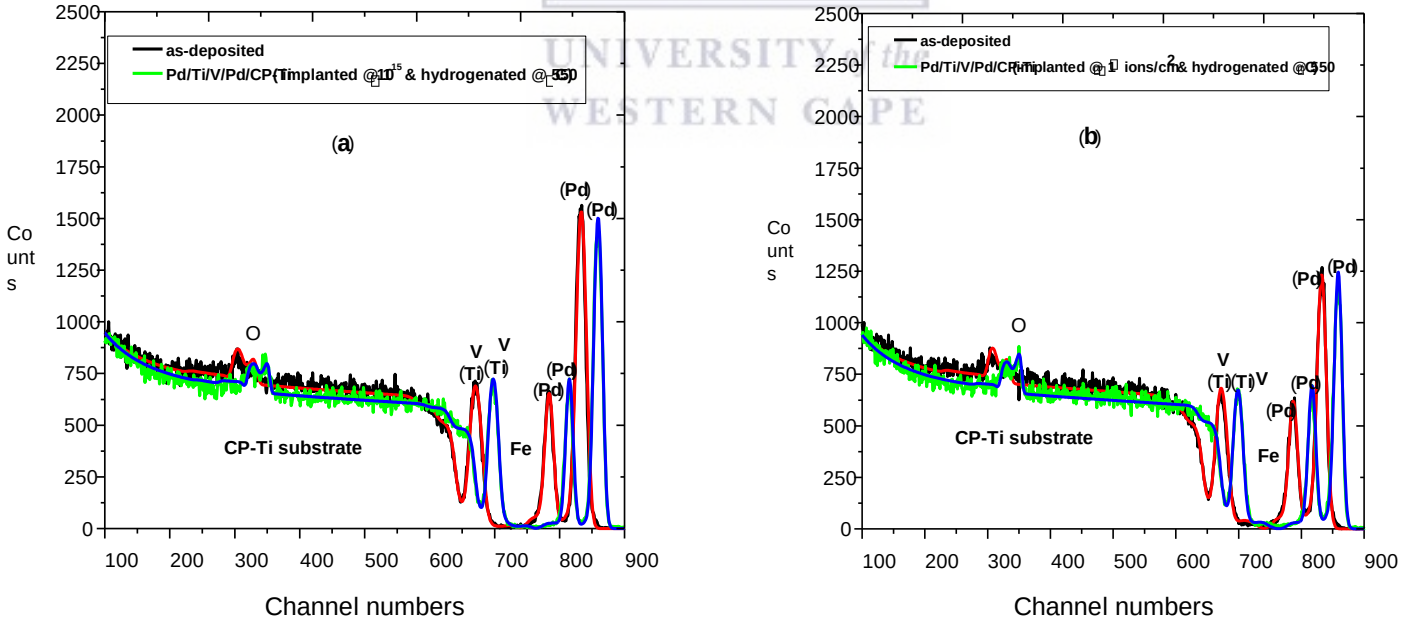

Figure 5.7: *RBS spectra of as deposited compared to the Fe implanted samples with energy of 150keV, (a) at 1×10^{15} ions/cm^2, and (b) 1×10^{16} ions/cm^2; hydrogenated at 550 º C for 30 minutes.*

5.3.4 **ERDA analysis**

In this experiment, the penetration range of 3 MeV He^{++} was simulated by SRIM at 75°. It was found to be ~7.65 µm, which was beyond ions penetration ranges of implanted ions used in this investigation. These allowed the probing of the samples beyond the ranges of the implanted species. **Figure 5.8 (a-c)** present the ERDA spectra of as-deposited plotted with implanted samples with 150 keV Fe ions to the fluence of 1×10^{12}, 1×10^{13}, and 1×10^{14} ions/cm^2; while **Figure 5.9 (a-b)** show that of samples implanted to a fluence of 1×10^{15}, and 1×10^{16} ions/cm^2 before and after hydrogenation. The results show differences in absorbed H content and depth in all samples investigated, hydrogenated under the same conditions. Quantitative analysis of as-deposited sample revealed only less than a per cent of surface H content that is due to water vapour and hydrocarbons from the atmosphere.

The non-implanted hydrogenated sample displayed H content that extends right from the surface into the bulk of the sample. The maximum H concetration in this sample was found to be ~4.8 at% at a depth of ~1.8 µm. The average H concentration was found to be ~2.6 at% over the probed depth, which was a reasonable concentration given the fact that hydrogenation time was kept at 30 minutes. This observation means that the non-implanted sample accommodated H, suggesting that the film stack has a loose microstructure. This was also an indication of the Pd catalyst layers, promoting the diffusion of H into the bulk.

However, for the Fe ion-implanted samples, the H concentration was restricted to the surface and near the surface of all the samples, decreasing towards the bulk. In general, all implanted samples display much lower H concentration than non-implanted sample except at low fluence (1×10^{12} *ions/cm^2*). The H concentration constantly decreased from the surface into the bulk, which suggests that Fe ion implantation did not enhance but restricted H absorption at least to these fluence values.

The average H concentration values over a probed depth were ~2.7, ~2.28, ~1.3, ~1.25, and ~1.18 at% in samples implanted up to a fluence of 1×10^{12}, 1×10^{13}, 1×10^{14}, $1 \times 10^{15,}$ and 1×10^{16} ions/cm^2 respectively.

These results suggest the entrapment of the H atoms by the implanted species. Furthermore, they indicate the ineffectiveness of Fe ion implantation in the enhancing of H absorption in these films, at least at the energies and fluence used in this investigation. A similar study will be conducted in future to confirm these findings at much higher ion energies, i.e., above the MeV range and lower fluence.

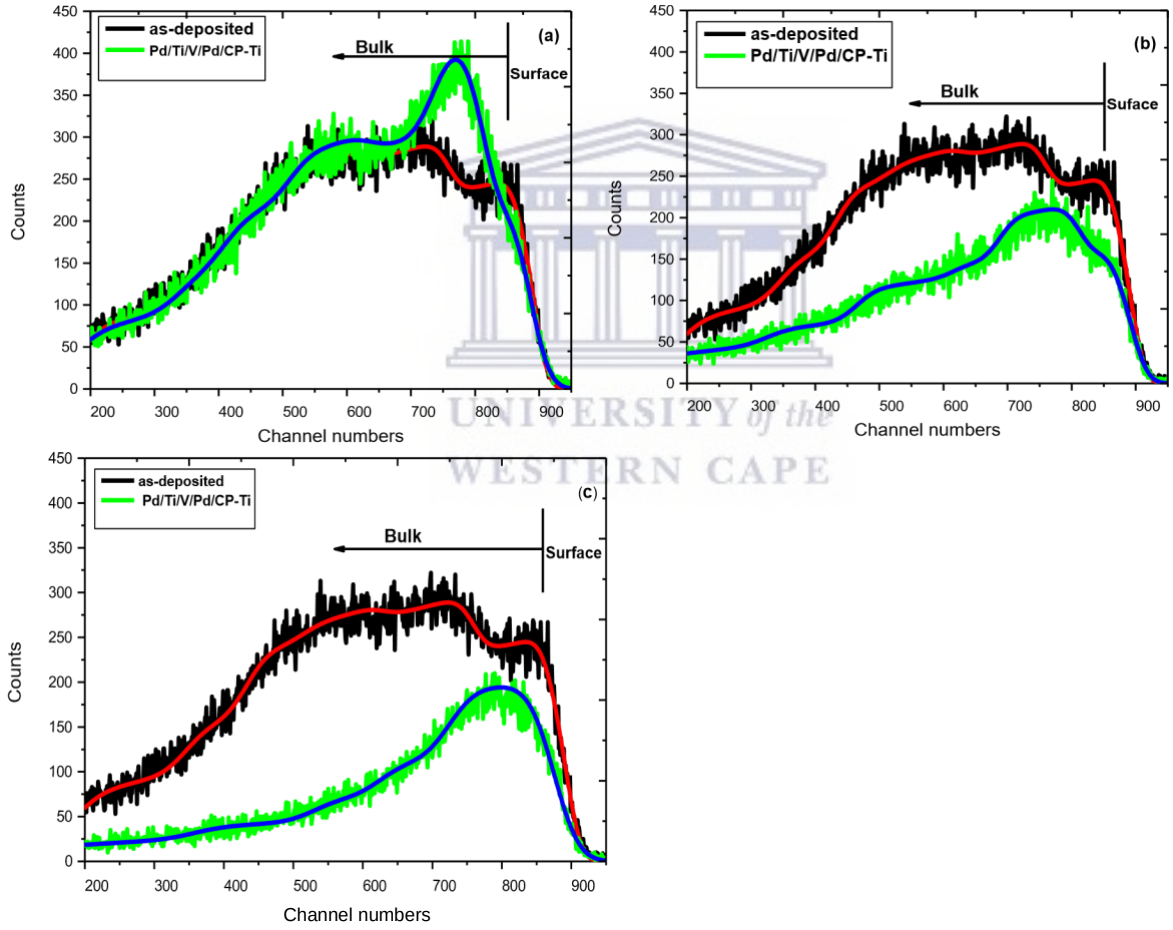

Figure 5.8: *ERDA spectra of as-deposited sample plotted against the Fe implanted samples with energy of 150 keV, (a) at 1×10^{12} ions/cm^2, (b) 1×10^{13} ions/cm^2, and (c) 1×10^{14} ions/cm^2; hydrogenated at 550 ° C for 30 minutes.*

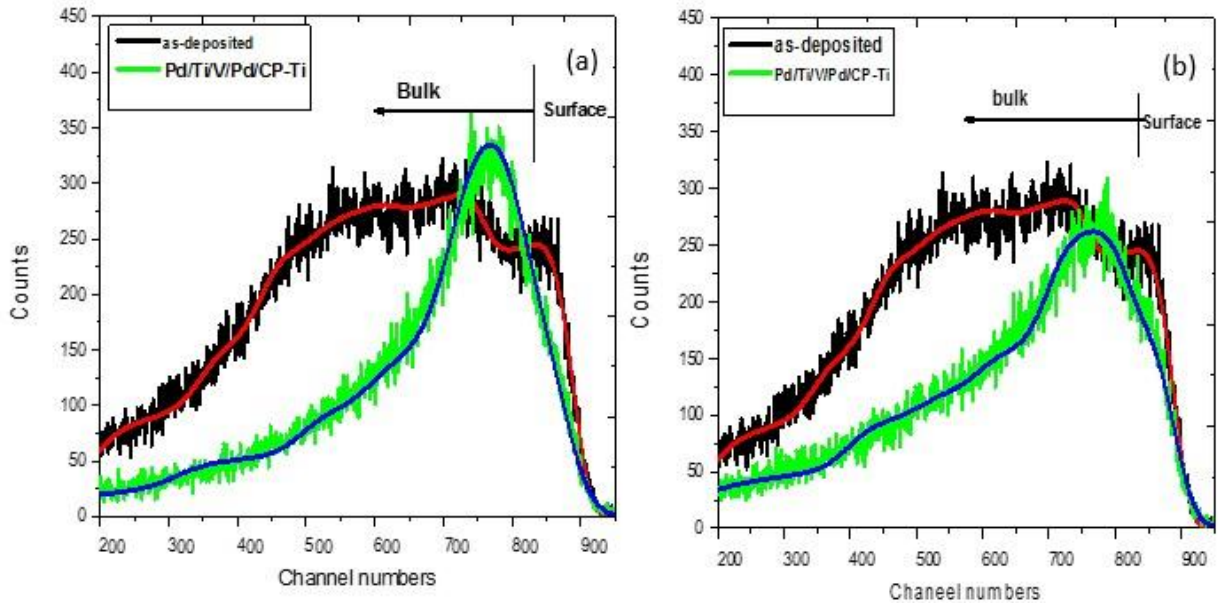

Figure 5.9: *ERDA spectra of as-deposited sample plotted against the Fe implanted samples with energy of 150 keV, (a) at 1×10^{15} ions/cm^2, and (b) 1×10^{16} ions/cm^2; hydrogenated at 550 º C for 30 minutes.*

Figure 5.10 (a-c) and **Figure 5.11 (a-b)** display the H profiles plots from the simulation of all spectra using SIMNRA software. The average H concentration vs fluency in all samples over the probed depth in both 150 keV Fe ion-implanted samples is presented in **Table 5.3**.

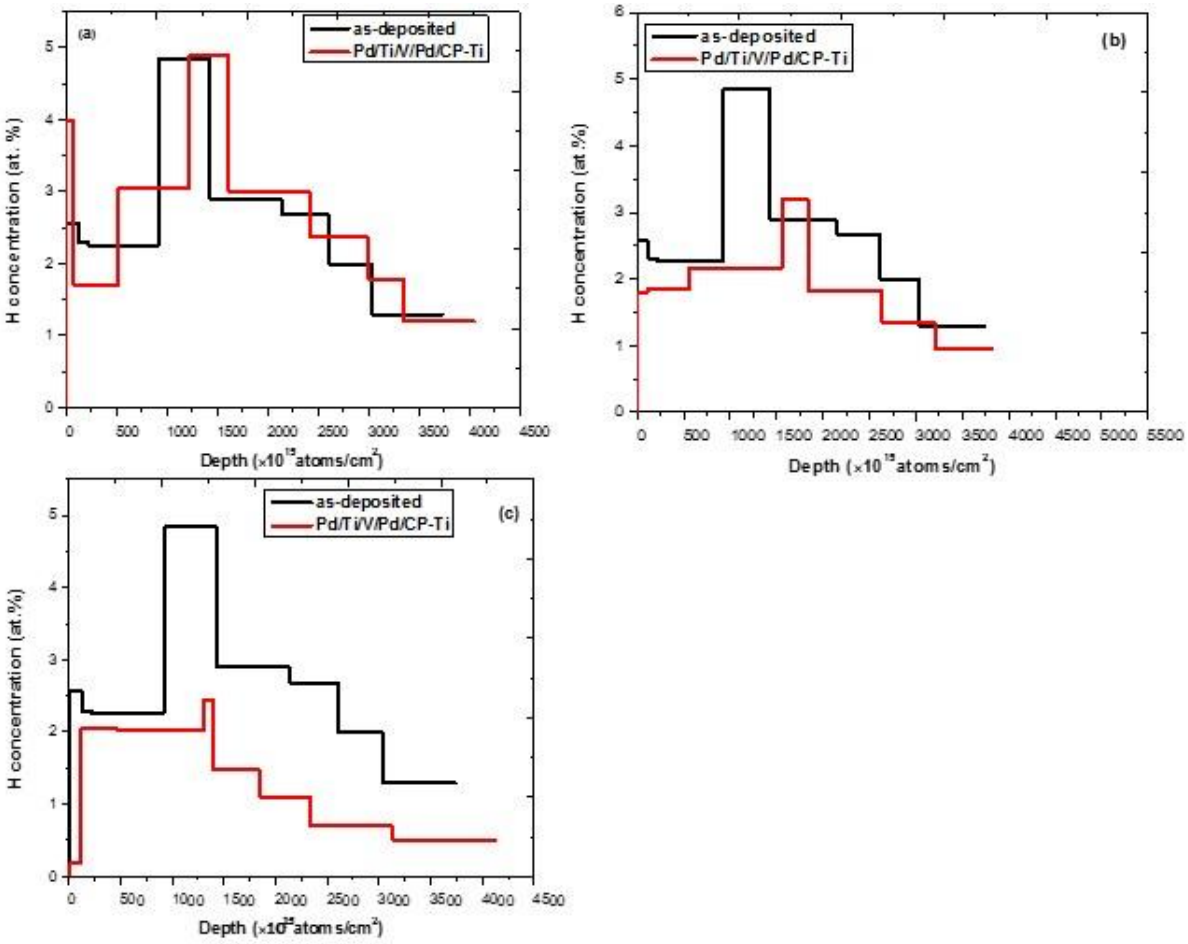

Figure 5.10: *H concentration depth profiles of (a) as deposited compared to the Fe implanted samples with energy of 150 keV, (a) at 1×10^{12} ions/cm^2, (b) 1×10^{13} ions/cm^2, and (c) 1×10^{14} ions/cm^2; hydrogenated at 550 º C for 30 minutes.*

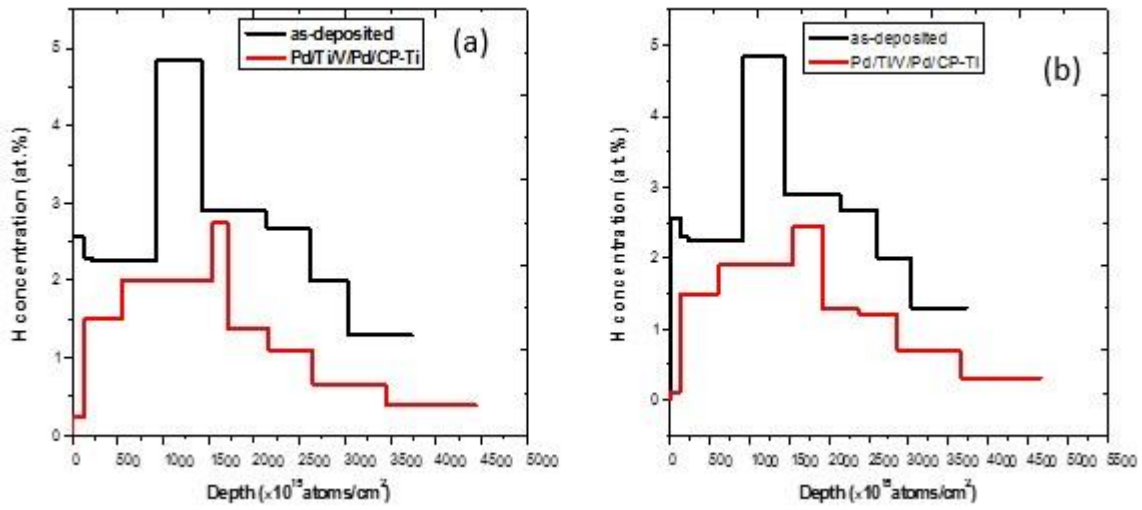

Figure 5.11: *H concentration depth profiles of (a) as deposited compared to the Fe implanted samples with energy of 150 keV, (a) at 1×10^{15} ions/cm^2, and (b) 1×10^{16} ions/cm^2; hydrogenated at 550 ° C for 30 minutes.*

Table 5.3: *Average H concentration (at %) over total probed depth.*

Samples (Fe implanted at 150 keV)	Fluence (ions/cm^2)	Average H concentration (at%) over total probed depth of 7.5 µm
Pd (25 nm)/Ti (50 nm)/V (50 nm)/Pd (25 nm)/CP-Ti	As deposited	2.6
Pd (25 nm)/Ti (50 nm)/V (50 nm)/Pd (25 nm)/CP-Ti	1×10^{12}	2.7
Pd (25 nm)/Ti (50 nm)/V (50 nm)/Pd (25 nm)/CP-Ti	1×10^{13}	2.28
Pd (25 nm)/Ti (50 nm)/V (50 nm)/Pd (25 nm)/CP-Ti	1×10^{14}	1.3
Pd (25 nm)/Ti (50 nm)/V (50 nm)/Pd (17 nm)/CP-Ti	1×10^{15}	1.25
Pd (25 nm)/Ti (50 nm)/V (50 nm)/Pd (17 nm)/CP-Ti	1×10^{16}	1.18

5.4 References

[5.1] Kirchheim, R., & Pundt, A. (2014). Hydrogen in Metals. In Physical Metallurgy: Fifth Edition (Fifth Edition, Vol. 1).

[5.2] López-Suárez, A., Valencia, C. E., López-Patiño, J., Vargas, M. C., & Fuentes, B. E. (2015). Improvement of titanium hydrogenation by low energy ion irradiation. International Journal of Hydrogen Energy, 40(11), 4194–4199.

[5.3] López-Suárez, A. (2017). Effect of Absorption and Desorption of Hydrogen in Ti and Ti Alloys. *New Advances in Hydrogenation Processes - Fundamentals and Applications.*

[5.4] Topić, M., Halindintwali, S., Mtshali, C., Nsengiyumva, S., & Khumalo, Z. M. (2019). Hydrogen storage in Ti-based metal hydrides investigated by elastic recoil detection analysis (ERDA). *Nuclear Instruments and Methods in Physics Research, Section B: Beam Interactions with Materials and Atoms*, 450(April), 239–243.

[5.5] Mazwi, S. (2016). Hydrogen storage in Ti-based coatings and Ti6Al4V alloy. Unpublished master's thesis, University of the Western Cape, Cape Town, South Africa.

[5.6] Adams, B. D., & Chen, A. (2011). The role of palladium in a hydrogen economy. *Materials Today*, *14*(6), 282–289.

[5.7] Heller, E. M. B., Suyver, J. F., Vredenberg, A. M., & Boerma, D. O. (1999). Oxidation and annealing of thin FeTi layers covered with Pd. *Applied Surface Science*, *150*(1), 227–234.

[5.8] Zaluski, L., Zaluska, A., Tessier, P., Ström-Olsen, J. O., & Schulz, R. (1995). Catalytic effect of Pd on hydrogen absorption in mechanically alloyed Mg2Ni, LaNi5 and FeTi. *Journal of Alloys and Compounds*, *217*(2), 295–300.

[5.9] Takasaki, A., Furuya, Y., & Taneda, Y. (1998). Hydrogen uptake in titanium aluminides covered with oxide layers. *Metallurgical and Materials Transactions A: Physical Metallurgy and Materials Science*, *29*(1), 307–314.

[5.10] Suda, T., Ohkawa, M., Sawada, S., Watanabe, S., Ohnuki, S., & Nagata, S. (2002). Effect of surface modification by ion implantation on hydrogenation property of TiFe alloy. *Materials Transactions*, *43*(11), 2703–2705.

[5.11] Fujihana, T., Okabe, Y. &Iwaki, M. (1989) 'Microstructure and Mechanical Properties of High Dose Nitrogen- implanted Iron, Chromium and Titanium Sheets*', 5, pp. 291–295.

[5.12] Magogodi S. (2019). Hydrogen storage capacity of the Ti-Pd multilayer systems. Published master's thesis. University of the Western Cape, Cape Town, South Africa.

[5.13] Sugazaki, Y., Furuya, T., & Satoh, H (1991). Influence of nitrogen implantation on the hydrogen absorption by Ti, *Nuclear Inst., and Methods in Physics Research B 59/60 722–725.*

Chapter 6

6.1 Summary and conclusion

In this study, investigating the material that could be suitable for storing hydrogen for an extended time in a safe manner and less costly was of research interest. The Pd/Ti/V/Pd film stack on CP-Ti was the material under investigation in this current study. Prior to implantation, samples were characterized for thickness confirmation using Rutherford backscattering spectrometry (RBS) technique discussed in the chapter 4 and it was found that two out of five samples deposited had a different thickness of the second Pd layer (layer 4); with this layer having a thickness of ~17 nm. Therefore, these two samples were implanted with Fe ions at 150 keV to higher fluences of 1×10^{15} and 1×10^{16} *ions/cm*^{2} respectively while the other three samples were implanted with Fe ions at 150 keV to fluences of 1×10^{12}, 1×10^{13}, *and* 1×10^{14} *ions/cm*^{2} respectively. The effect of implantation on hydrogen adsorption was investigated and compared with the non-implanted for the same systems.

The non-implanted samples showed rough and non-uniform surfaces with visible interconnected crystals observed from SEM micrographs. In comparison with non-implanted, the implanted samples displayed no visible effect at low fluences (1×10^{12} ions/cm^2, 1×10^{13} ions/cm^2, and 1×10^{14} ions/cm^2). In contrast, at high fluences (1×10^{15} ions/cm^2 and 1×10^{16} ions/cm^2) visible effect was observed as the samples displayed slight changes. XRD results revealed no intermixing of films that took place; as a result, no new phases were observed, but only the broadness in peaks at high fluences was observed. The RBS results showed that the system is stable as the layers were still well separated after the implantation process, and they agree very well with XRD results as no new phases were observed. From the simulations, Ti was found to have reacted with oxygen with 30% O and 70% Ti forming TO_2 stoichiometry from all the samples. The thicknesses of the subsurface

Pd layer for samples implanted at high fluences ((1×10^{15} ions/cm^2 and 1×10^{16} *ions/cm^2*) were found to be different from the rest of the samples due to the discrepancy attributed to the fault crystal monitor reading.

The next phase in this study was to investigate the implanted samples hydrogenated at the optimum temperature of 550 º C for 30 minutes. The face centred tetragonal TiH_2 was not revealed by XRD due to nature of this technique to be able to reveal crystal phases; hence, it was incredibly challenging to distinguish since its amount was exceptionally low and overlapped with Ti peaks.

RBS investigated the thermal stability of the system, and no intermixing of the films occurred. The absence of intermixing of the films suggest that the system is stable, and the integrity of the film stack is not affected by the hydrogenation. The TiH_2 appeared to function as the diffusion barrier limiting the inter-diffusion of atoms of the film stack. The results suggested that this system can be used multiple times without structural failure, particularly the non-implanted system.

The ERDA technique investigated the H profile. ERDA revealed that the average H concentration was high for a non-implanted system with 2.6 at. % over the probe depth. The implanted samples showed less H concentration at high fluences except at low fluence (1×10^{12} *ions/cm^2*). The H content constantly decreased from the surface into the bulk, suggesting that Fe ion implantation did not enhance but restricted H absorption at least to these fluence values. The average H concentration values over a probed depth were ~2.7, ~2.28, ~1.3 ~1.25, and ~1.18 at. % in the samples implanted up to fluence of 1 × 10^{12}, 1 × 10^{13}, 1 × 10^{14}, 1 × 10^{15}, and 1 × 10^{16} *ions/cm^{2,}* respectively. Better performance of the system was achieved at non-implanted sample and low fluence implanted sample, hence the overall conclusion is that the system should be investigated and evaluated without using implanted ions for better performance. A Similar study will be conducted in the future to confirm these findings at much higher ion energies, i.e., above the MeV

range and lower fluences because the sample implanted at lower fluence showed high H concertation as compared to as deposited particularly at the surface.

6.2 **Future work**

In this investigation, other aspects were not investigated. Hence, they will be looked at in future as this project forms a long-term project in hydrogen storage technology. These aspects include:

i. The impact of implantation energy on hydrogen absorption.

ii. The impact of the hydrogenation time.

iii. The effect of a gas flow rate.

iv. The effect of the gas pressure.